

Development of a charge transport model for white OLEDs

Citation for published version (APA):

Vries, de, R. J. (2012). *Development of a charge transport model for white OLEDs*. [Phd Thesis 1 (Research TU/e / Graduation TU/e), Applied Physics and Science Education]. Technische Universiteit Eindhoven.
<https://doi.org/10.6100/IR731150>

DOI:

[10.6100/IR731150](https://doi.org/10.6100/IR731150)

Document status and date:

Published: 01/01/2012

Document Version:

Publisher's PDF, also known as Version of Record (includes final page, issue and volume numbers)

Please check the document version of this publication:

- A submitted manuscript is the version of the article upon submission and before peer-review. There can be important differences between the submitted version and the official published version of record. People interested in the research are advised to contact the author for the final version of the publication, or visit the DOI to the publisher's website.
- The final author version and the galley proof are versions of the publication after peer review.
- The final published version features the final layout of the paper including the volume, issue and page numbers.

[Link to publication](#)

General rights

Copyright and moral rights for the publications made accessible in the public portal are retained by the authors and/or other copyright owners and it is a condition of accessing publications that users recognise and abide by the legal requirements associated with these rights.

- Users may download and print one copy of any publication from the public portal for the purpose of private study or research.
- You may not further distribute the material or use it for any profit-making activity or commercial gain
- You may freely distribute the URL identifying the publication in the public portal.

If the publication is distributed under the terms of Article 25fa of the Dutch Copyright Act, indicated by the "Taverne" license above, please follow below link for the End User Agreement:

www.tue.nl/taverne

Take down policy

If you believe that this document breaches copyright please contact us at:

openaccess@tue.nl

providing details and we will investigate your claim.

Development of a charge transport model for white OLEDs

PROEFSCHRIFT

ter verkrijging van de graad van doctor aan de
Technische Universiteit Eindhoven, op gezag van de
rector magnificus, prof.dr.ir. C.J. van Duijn, voor een
commissie aangewezen door het College voor
Promoties in het openbaar te verdedigen
op donderdag 26 april 2012 om 16.00 uur

door

Rein Jan de Vries

geboren te Hengelo

Dit proefschrift is goedgekeurd door de promotoren:

prof.dr. R. Coehoorn

en

prof.dr.ir. R.A.J. Janssen

Omslagontwerp: B. Senders en R. J. de Vries

Druk: Universiteitsdrukkerij Technische Universiteit Eindhoven.

ISBN: 978-90-386-3122-6

A catalogue record is available from the Eindhoven University of Technology Library.



This research forms part of the research programme of the Dutch Polymer Institute (DPI), project #680.

Contents

1	Towards a predictive device model for white OLEDs	1
1.1	OLEDs for lighting	2
1.1.1	Device principle	3
1.1.2	Organic materials	3
1.1.3	White OLEDs	4
1.2	Towards a multilayer OLED device model	6
1.2.1	OLED device modeling	7
1.2.2	Methods developed in this thesis	8
1.2.3	State-of-the-art transport models	10
1.3	Scope of this thesis	14
2	Extraction of materials and device parameters	19
2.1	Introduction	20
2.2	Method	23
2.3	Parameter extraction on artificial data - two case studies	25
2.3.1	Ideal injecting contact and no trap states	25
2.3.2	Material with trap states	30
2.4	Application to hole and electron transport in PF-TAA	32
2.4.1	Hole transport	32
2.4.2	Electron transport	34
2.5	Summary and conclusions	38
2.6	Appendix A - Experimental uncertainty	40
3	The built-in voltage from electroabsorption	45
3.1	Introduction	46
3.2	Experimental method	47
3.3	Experimental results and analysis	49
3.4	Conclusions	55

4	Hole transport in a polyfluorene based copolymer	59
4.1	Introduction	60
4.2	Experimental results	61
4.3	Modeling results	62
4.4	Conclusions	66
5	Electron transport in Alq₃	69
5.1	Introduction	70
5.2	Experimental results	71
5.2.1	$J(V)$ curves of samples employed in the analysis	71
5.2.2	Additional transport studies of Alq ₃ devices	72
5.2.3	Selection of $J(V)$ characteristics studied	73
5.2.4	Amorphous nature of Alq ₃ films	75
5.3	ECDM results and discussion	76
5.4	Summary and conclusions	82
5.5	Appendix: EGDM results and discussion	84
6	A study of dark injection transients	89
6.1	Introduction	90
6.2	Experimental	91
6.3	Modeling	93
6.4	Results and discussion	94
6.5	Conclusions and outlook	98
7	A device model for multilayer white OLEDs	101
7.1	Introduction	102
7.2	Electron transport in NET-5	103
7.2.1	EGDM results	105
7.2.2	ECDM results	107
7.3	Electron transport in Spiro-DPVBi	110
7.4	Monte Carlo simulation of a multilayer stack	113
	Summary	117
	Samenvatting	119
	List of publications	122
	Curriculum vitae	125
	Dankwoord	127

Towards a predictive device model for white OLEDs

In this thesis crucial steps towards the development of an opto-electronic device model for multilayer white OLEDs are presented. This chapter gives a general introduction to the rapidly developing field of organic electronics and focuses on white OLEDs. It also introduces the scientific challenges towards the development of such a multilayer device model. A detailed scope of the thesis is given at the end of this chapter.

1.1 OLEDs for lighting

Organic light-emitting diodes (OLEDs) are seen as a promising candidate for future lighting applications.^{1–5} OLEDs can be made ultra thin, color tunable and transparent in the off-state which leads to a variety of potential innovative products. OLEDs are already widely used for display applications. Recently, also stretchable polymer based light-emitting devices have been demonstrated.⁶ With functionalities such as flexibility and stretchability, applications of lighting on e.g. clothing or goody bags can be realized. A strong market growth of OLED technology for lighting is expected,⁵ at present by applications from designers and around 2015 for general lighting by roll-to-roll production.⁷ Figure 1.1 shows an example of a technology roadmap for OLEDs.

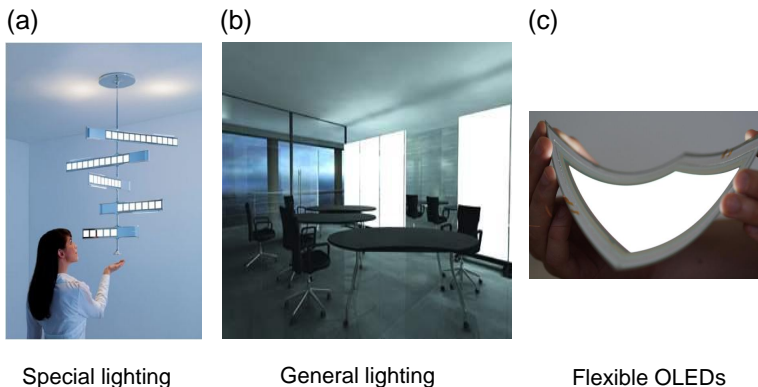


Figure 1.1: Visualization of a “roadmap” for OLED technology. (a) Special lighting which is presently available. (b) General lighting for applications in home or offices, expectedly available from 2012 and in (c) flexible OLEDs, expectedly available from 2015. Photograph (a) and (b) are from Philips (see www.lumiblade.com).

More concretely, the roadmap for white OLED panels in terms of luminous efficacy is expected to approach a value of about 170 lm/W in 2020.⁵ In conjunction with the special features OLEDs offer for some applications, this value would be sufficient to be competitive with, for example, LED technology. So far, the highest efficacy reported on laboratory devices is 124 lm/W by Novaled AG in collaboration with the Technical University of Dresden.⁸ Expectedly, OLEDs for lighting can only be successful if lifetimes up to 10.000 hours at a brightness level of 5000 cd/m² with efficiencies beyond 100 lm/W can be realized at a low cost. In spite of worldwide efforts by industries and knowledge institutes, these ambitious requirements have not yet been realized.

1.1.1 Device principle

In 1987 the first electroluminescent device based on organic materials was made by Tang and VanSlyke.⁹ The physical processes and basic structure of an OLED are shown in Figure 1.2. To illustrate the functioning, a device is shown which will be studied in more detail within this thesis. A solution processed layer of a blue-emitting polyfluorene-triarylamine (PF-TAA) based co-polymer, with a typical thickness of 80 nm, is sandwiched in between a poly(3,4-ethylenedioxythiophene):poly(styrene sulfonic acid) (PEDOT:PSS) anode and a cathode. Holes and electrons are injected from the anode and cathode into the highest occupied molecular orbital (HOMO) and lowest unoccupied molecular orbital (LUMO), respectively. After injection, hopping transport takes place in the organic layer. Subsequently, the holes and electrons can recombine to form an exciton that can decay by emitting, in this case, blue light.

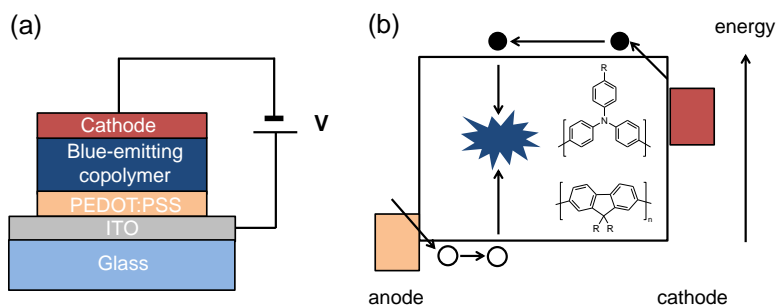


Figure 1.2: Basic functioning of the single-layer blue-emitting co-polymer based OLED which is one of the devices studied within this thesis. (a) Schematic layer structure. (b) Schematic picture showing the basic physical processes of charge carrier injection, transport and recombination are indicated (arrows). The holes and electrons are visualized by empty and filled dots, respectively.

1.1.2 Organic materials

Organic materials such as polymers are often electric insulators. However, some organic materials have semiconducting properties. Such materials typically have alternating single and double bonds between the carbon atoms. In these systems, the presence of π -orbitals, which are derived from the atomic p-orbitals and which are delocalized over the molecule, leads to the conducting properties. On top of this, such organic materials have optoelectronic properties which make them interesting for a broad range of applications, for instance for OLEDs, organic transistors and photovoltaic cells. Organic materials can consist of long-chain molecules (polymers) or small-molecules. Figure 1.3 shows some typical

cathode, respectively. Alternatively, (b) shows a stacked OLED, (c) a pixelated OLED and (d) a monochrome blue device with down-converting phosphorescent layers for red and green emission¹³. The approaches shown in 1.4 (b), (c) and (d) offer specific advantages such as good stability, color tunability and a simple device architecture, respectively. The “all-integrated” approach shown in 1.4 (a) is often regarded as the most promising in terms of high-efficiency and low production cost.

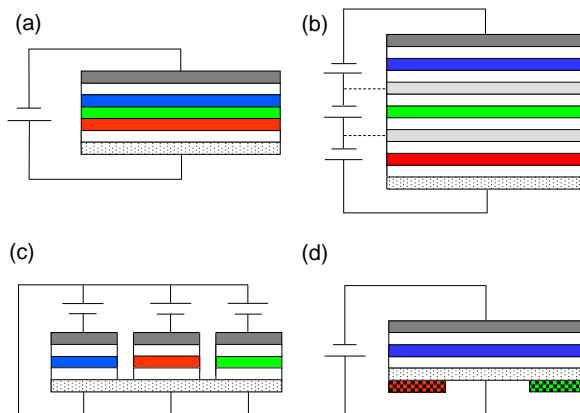


Figure 1.4: Schematic overview of several methods for obtaining white emission. The white layers are transport layers for electrons and holes. The colored layers are emissive layers and the dark grey and dotted white layers are the cathode and anode, respectively. (a) Shows a multilayer stack containing all layers. In (b) a stacked OLED with separate voltage supplies is shown and (c) gives a pixelated OLED. (d) Shows a blue-emitting device with down-converting phosphorescent layers for red and green emission.

Improving OLED performance in terms of, for example, luminous efficacy requires efforts from several disciplines, including materials development, layer stack development and OLED module design. A major opportunity to further optimize the performance is by improving the light outcoupling efficiency.¹⁴ Since OLEDs form a microcavity, the light is waveguided and therefore only in case of a well designed device the optimal efficacy is achieved. This can be realized by a combination of well chosen materials and layer thicknesses so that the recombination takes place at the right position. Moreover, a well designed device is expected to lead to an improved lifetime,⁶ which is a major issue for organic devices.² These examples sketch the necessity for the rational design of (multilayer) OLEDs. This can be achieved by developing a device model which can serve as a design tool for the improvement of OLED performance.

1.2 Towards a multilayer OLED device model

In this thesis, crucial elements towards the development of a device model with predictive value for multilayer white OLEDs are presented. Contributions have been made to an experimental and modeling study of the multilayer stack shown in Figure 1.5.

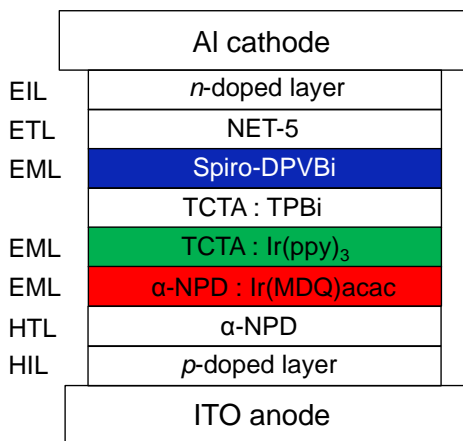


Figure 1.5: White OLED consisting of various evaporation deposited small molecule based organic layers. A *p*-doped hole injection layer (HIL) is deposited on top of the transparent ITO anode. On top of that, an α -NPD layer is deposited to conduct holes throughout the stack (HTL). In the middle of the device, phosphorescent green and red-emitting layers are present based on iridium complexes, TCTA : Ir(ppy)₃ and α -NPD : Ir(MDQ)acac, respectively. Also a fluorescent blue-emitting layer (EML) based on Spiro-DPVBi is present. In between the emissive green and blue layer, an interlayer is deposited. It prevents exciton transfer between the emissive layers and is based on TCTA and TPBi. Finally, a NET-5 based electron transport and *n*-doped injection layer are deposited together with the Al cathode.

The work was done within the framework of a Dutch Polymer Institute (DPI) project (#680). The materials and devices studied were made available within the EU project “Advanced Experimentally Validated Integrated OLED Model” (AEVIOM),¹⁵ and from Philips Research Aachen. In a complementary way, both projects have contributed to the development of a methodology which makes it possible to apply a device model to a multilayer white OLED stack such as shown in Figure 1.5. This device contains various layers with different functionalities. Similar systems, which are often called “hybrid” stacks since both fluorescent and phosphorescent emission are exploited, have been studied by Schwartz *et al.* in Ref. 16. The device consists of various evaporation deposited

small-molecule based organic layers, in between a transparent indium tin oxide (ITO) anode and an aluminum (Al) cathode. An N,N'-diphenyl-benzidine (α -NPD) hole transport layer is used and for the electron transport a NET-5 layer (material supplied by Novaled AG.,⁸ molecular structure not specified) is present. Blue emission is realized using a fluorescent 2,2',7,7'-tetrakis(2,2'-diphenylvinyl)spiro-9,9'-bifluorene (Spiro-DPVBi) layer. Phosphorescent green and red emission is obtained from layers based on iridium dyes. For the green emission, a host-guest system of 4,4',4''-tris(N-carbazolyl)-triphenylamine (TCTA) with tris(phenyl-pyridyl)-iridium ($\text{Ir}(\text{ppy})_3$) is used and for the red layer an α -NPD host with iridium(III)bis(2-methyl-dibenzoquinoline) (acetylacetonate) ($\text{Ir}(\text{MDQ})\text{acac}$) dye is used. In between the blue-emitting Spiro-DPVBi layer and the green emitting TCTA: $\text{Ir}(\text{PPY})_3$ layer, an interlayer is present. This layer is a mixture of TCTA with TPBi (1,3,5-tris(1-phenyl-1H-benzimidazol-2-yl)benzene) and has a crucial role in the stack. It prevents blue excitons from diffusing into the green emission layer and simultaneously conducts both electrons and holes so that both species can reach the emissive layers. Obviously, the multilayer stack shown in Figure 1.5 leads to a broad variety of research challenges since it contains various materials and interfaces. The approach chosen throughout most of this thesis is to focus on studying charge transport $J(V)$ characteristics for single-layer devices. We focus on the development of methods, and apply these to suitable materials, including some electron transporting materials used in the "AEVIOM-stack". If in a systematic way, all materials of the stack have been independently characterized in single-layer devices with well injecting contacts. A multilayer model can be developed which makes it possible to study for example the position of the recombination zone in the emitting layer(s).¹⁷ Being able to tune the recombination zone is essential for designing a device with a good color rendering index and external quantum efficiency (EQE).

1.2.1 OLED device modeling

The rational design of OLEDs is possible on the basis of a device model which describes the physical processes.^{18,19} Already in 1999, Staudigel *et al.*,²⁰ presented a model for a multilayer device based on the well-known small-molecule materials α -NPD and tris(8-hydroxyquinolinato)aluminium (Alq_3). However, necessary progress has been slow due to a lack of accurate transport models and the large amount of parameters needed to describe the physical processes in such a device. A crucial element which was added only recently is the consistent treatment of energetic disorder. Figure 1.6 shows the basic functioning of a single-layer OLED. Injection of electrons (e^-) and holes (h^+) are shown over barriers Δ_e and Δ_h into the lowest unoccupied molecular orbital (LUMO) and the highest occupied molecular orbital (HOMO). The HOMO and LUMO levels are indicated by energetically disordered states in between which the hopping transport in the bulk of the material takes place. The energetic disorder is visualized by a Gaussian with a width, σ . It should be noted that the exact shape of the density of states is a topic of ongoing investigation.

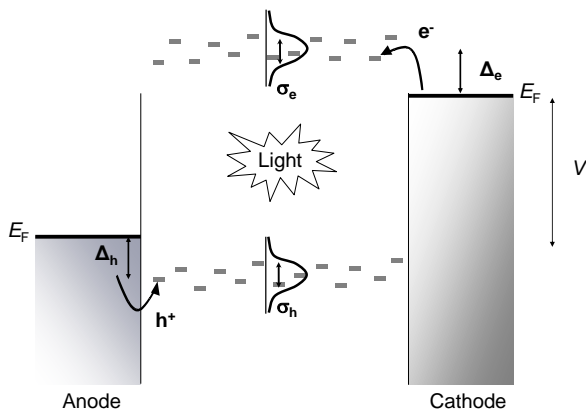


Figure 1.6: Basic functioning of an OLED. Charge carrier injection from the electrodes and transport of electrons (e^-) and holes (h^+) is visualized. The applied voltage (V) is such that flat band conditions are obtained. Within the HOMO and LUMO, the energetic disorder is indicated by Gaussians with a width, σ . Also recombination of the carriers which generates light is indicated.

The *ab-initio* development of a device model for OLEDs is schematically shown in Figure 1.7 in a number of steps. Starting at the molecular structure of the material, molecular dynamics calculations can be used to determine the amorphous structure. Based on that, density functional theory (DFT) gives the opportunity to determine the hopping probabilities. It should be noted that these fields are in an upcoming and quickly developing phase.^{21,22} Subsequently, 3D Monte Carlo (MC) or Master Equation (ME) calculations can give the mobility as a function of for instance the field and charge carrier density.^{23,24} In this thesis, these results are used as input for one-dimensional drift-diffusion modeling of the measured current density, J . This makes the experimental validation of transport models for organic materials possible. As a next step, exciton diffusion and light out-coupling should be included in the model.¹⁴ This completes the chain from the molecular scale to the eventual light output.

1.2.2 Methods developed in this thesis

The work presented in this thesis contributes to the systematic built-up of a multi-layer OLED device model. In particular, it focuses on the experimental validation of one dimensional drift-diffusion models. These models are based on 3D Master Equation calculations which give the mobility as a function of field and charge carrier density for a broad range of values for the disorder parameter $\sigma/k_B T$. A systematic approach to accurately obtain the materials parameters, such as e.g. σ , which determine this mobility from measured $J(V, L, T)$ characteristics is de-

veloped. This method, which is based on a Gauss-Newton algorithm, makes a quick experimental validation possible. In a systematic way, it was investigated how well it is possible to perform an accurate and unique extraction in realistic electron transport devices in which typically a rather large amount of parameters has to be determined.

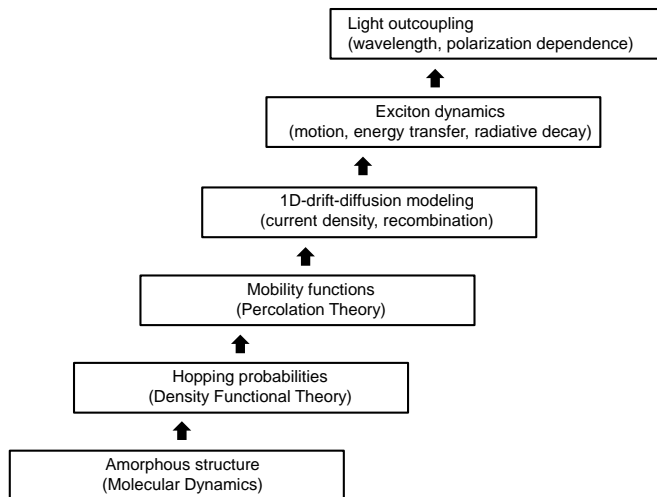


Figure 1.7: Overview of the steps included in the development of a device model for OLEDs.

Another method which was developed makes it possible to determine the built-in voltage by analyzing electroabsorption measurements using a device model. The built-in voltage V_{bi} , is the difference between the effective work functions of the anode and cathode. Accurately knowing V_{bi} makes it possible to determine the mobility from the transport characteristics.

For the case of electron transport, it has often been observed that the measured current-density depends on the history of the device.²⁵ This may be due to charge carrier relaxation effects. To investigate this, we have measured and modeled the time dependence of the current density. For the modeling, we have used the drift diffusion model without introducing extra parameters. From the analysis, we found strong indications for the importance of relaxation effects. A future goal is to take such effects into account in device modeling.

All methods developed are based on a device model and are applicable to real devices. The application and development of such device models, makes it possible to gain understanding about the transport in organic materials and thereby about the functioning of real OLEDs. In the next section, a description of the state-of-the-art of the transport models used is presented.

1.2.3 State-of-the-art transport models

Organic materials based on polymers or small-molecules are often structurally disordered. This results in localization of the charge carriers, so that the concept of band conduction, which applies to crystalline materials, does not hold. Instead, charge carrier conduction takes place by hopping from one localized state to another. The hopping rate depends on the overlap of the electronic wave functions of the hopping sites. This phonon-assisted tunneling process was first proposed by Mott and Conwell.^{26,27} Miller and Abrahams²⁸ developed a model for the hopping rate between localized states. The transition rates W_{ij} for hopping between states i and j for which $\epsilon_j > \epsilon_i$ are given by:

$$W_{ij} = \nu_0 \exp(-2\alpha R_{ij}) \exp\left(-\frac{\epsilon_j - \epsilon_i}{k_B T}\right) \quad \text{for } \epsilon_j > \epsilon_i, \quad (1.1)$$

$$W_{ij} = \nu_0 \exp(-2\alpha R_{ij}) \quad \text{for } \epsilon_j < \epsilon_i. \quad (1.2)$$

Here, ν_0 is an attempt-to-jump frequency, α the inverse of the wave-function localization length, R_{ij} the distance between the sites in between which the hopping takes place and ϵ_i the energy of state i . The rate for upward hops, to a final state with a higher energy, is proportional to two exponential functions of which the first describes the distance dependence of the tunneling rate and where the second is an Arrhenius factor which describes the temperature dependence. Phonon absorption makes it possible to hop to a state higher in energy. For hops downward in energy, ($\epsilon_j < \epsilon_i$), no thermal energy is needed, which leads to the expression given by equation 1.2. An alternative to the Miller Abrahams hopping rates is to use the so-called Marcus hopping rates.²⁹ In this formalism, also the reorganization energy of the molecule, which is material-specific, is taken into account. Herewith, Marcus hopping rates give a more complete description of the transport physics. However also an extra, material-specific, parameter is involved which is not *a priori* known and thereby complicates the determination of a mobility function. Therefore, the Miller Abrahams hopping rates have formed the input for many theoretical studies of charge transport in organic semiconductors with a disordered nature. In such studies, supercomputer simulations are performed in which a three-dimensional box with periodic boundary conditions is filled with N point sites. The site energies are drawn from a certain (often Gaussian) distribution to describe the energetic disorder. Secondly, m free charge carriers are entered into the system which can move as described by for instance the Miller Abrahams hopping rates under the influence of an applied electric field, F . Such a simulation leads to a prediction of the so-called mobility of the charge carriers, which is defined as:

$$\mu \equiv \frac{\langle v \rangle}{F}, \quad (1.3)$$

where $\langle v \rangle$ is the average velocity of the carriers in the direction of the field. From the Miller Abrahams hopping rates Eq. 1.1 and 1.2 it follows that the mobility is dependent on the temperature T and through the site energies ϵ also on the applied electric field. The calculated mobility may be compared to the

results of measurements on real devices. Examples of experimental techniques which have been used extensively in the literature to rather directly probe the effective mobility in a device are for instance time-of-flight (TOF) or dark injection (DI) measurements.^{30,31} These techniques are frequently used to study disordered organic semiconductors. For instance from TOF experiments several authors e.g. Borsenberger *et al.*³² and Malliaras *et al.*,³³ argued that the mobility can be described using the so-called Poole-Frenkel electric-field dependence^{34,35}:

$$\mu(F) = \mu_{0,\text{PF}} \cdot \exp(\gamma(T)\sqrt{F}). \quad (1.4)$$

In this empirical equation, $\mu_{0,\text{PF}}$ is the mobility at zero field and γ is a temperature dependent activation parameter:

$$\gamma(T) = \beta[1/k_{\text{B}}T - 1/k_{\text{B}}T_0], \quad (1.5)$$

where β and T_0 are empirical parameters.

Another commonly used technique to study the mobility is by analyzing the measured current density as a function of, the applied voltage. In a simple approach, the field dependence of the mobility is neglected and only the drift contribution is taken into account. If also the contacts are assumed to be well-injecting (no barrier at the interface), the relation between the current density and the voltage in a single carrier device is given by the Mott-Gurney (MG) relation³⁶:

$$J(V) = \frac{9}{8}\epsilon_0\epsilon_r\mu\frac{(V - V_{\text{bi}})^2}{L^3}, \quad (1.6)$$

for $V > V_{\text{bi}}$, with ϵ_0 the vacuum permittivity and ϵ_r the relative dielectric permittivity. Under the assumptions made Eq. (1.6) may be used to determine the mobility in so-called space charge limited devices. In such devices, the current is limited by the space charge in the device and there is no injection barrier at the metal-organic interface which restricts the current. Using Eq. 1.6 with $\mu = \mu(F) = \mu(V/L)$ as given by Eq. 2.8 it is often investigated whether the Poole-Frenkel (Eq. 2.8) field dependence of the mobility is obtained.

Such analyses lead to the question how the obtained empirical parameters relate to the more fundamental materials properties such as for instance the volume density of hopping sites, N_t , and the shape of the density of states (DOS) in the material. This lack of basic understanding inspired Bässler³⁴ *et al.* to develop the so-called Gaussian disorder model (GDM). His Monte Carlo simulations assumed a Gaussian distribution to describe the energetic disorder and led, in a certain field-range, to a Poole-Frenkel-like field dependence of the mobility.²³ In contrast to the empirical Poole-Frenkel model, the GDM introduces physically interpretable parameters such as the width (standard deviation) of the DOS, σ , and the hopping site density. If also spatial correlations between the site energies were taken into account,³⁷ an even better agreement with the experimental field dependence of the mobility was found for certain materials. These correlations can be caused, e.g. by the overall field of the randomly oriented dipole moments of the molecules. This led to the introduction of the correlated disorder model (CDM) by Novikov *et al.*³⁸ Other physical causes of site energy correlations can

be a strain in the polymer backbone³⁹ or a variable morphology.⁴⁰ In 2003, Tanase *et al.*⁴¹ showed that the difference in the measured mobility in OLEDs and organic field effect transistors (OFETs) can be understood from a charge carrier concentration dependence of the mobility. This additional insight has led Pasveer *et al.*²³ to extend the GDM to the so-called extended Gaussian disorder model (EGDM) in which also the charge carrier density dependence of the mobility is taken into account. Similarly, the CDM was extended by Bouhassoune *et al.*²⁴ to the extended correlated disorder model (ECDM). Both models are based on three-dimensional Master Equation calculations and give the mobility as a function of electric field, charge carrier density and temperature. Hopping in a random Gaussian (a) or correlated (b) density of states is schematically shown in Figure 1.8.

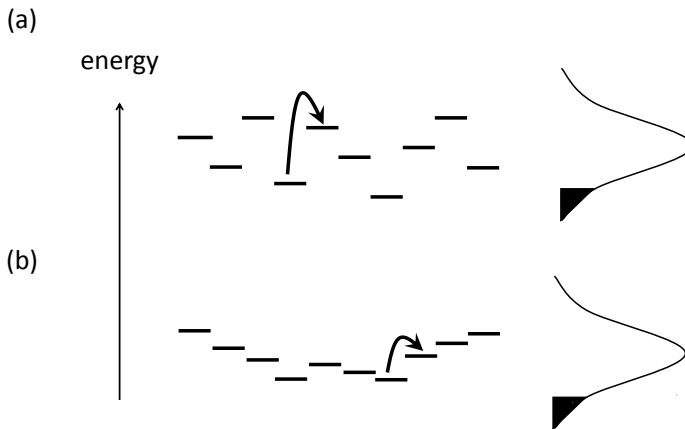


Figure 1.8: Schematic visualization of hopping transport in a Gaussian density of states. In (a) charge carriers hop (arrow) in a positionally (horizontal axis) uncorrelated Gaussian density of states which describes the energetic disorder (vertical axis). The resulting mobility as obtained using a three dimensional master equation solver is published in Ref.²³ In (b), a positionally correlated energy level landscape is shown, which leads to the extended correlated disorder model (ECDM)²⁴. Also the filling of lower energy states in the tail of the Gaussian is indicated.

Within the (E)GDM and the (E)CDM, the thermally activated transport process leads to a temperature dependence of the zero field and zero charge carrier mobility described by:

$$\mu_{(F=0, n=0)} = \mu_0^* \exp \left[-C \left(\frac{\sigma}{k_B T} \right)^2 \right], \quad (1.7)$$

with a C -value which depends on the wave function overlap and in the case of

Miller-Abrahams hopping with a typical value in the range 0.38 to 0.5 for the EGDM,⁴² and with a typical value around 0.29 for the ECDM.²⁴ Recent work by Cottaar *et al.*⁴³ suggests that the C -parameter can be higher if the hopping process is described using the more comprehensive Marcus theory. Van Mensfoort *et al.* have implemented both mobility models in a one dimensional drift-diffusion solver⁴⁵ which can quickly calculate current-voltage characteristics. The drift-diffusion equation used in the solver developed by the authors⁴⁶ is given by:

$$J = J_{\text{drift}} + J_{\text{diffusion}} = e\mu nF \mp eD \frac{dn}{dx}, \quad (1.8)$$

where J_{drift} and $J_{\text{diffusion}}$ are the drift and diffusion contributions to the current density, e is the elementary charge, n the density of the charge carriers, D the diffusion coefficient and x the position.

For describing the hole and electron contribution to the current-density, the minus or plus-sign should be used, respectively. In the case of organic semiconductors, disorder is present and the generalized Einstein relation describes the diffusion coefficient:

$$D = \frac{n}{e \frac{\partial n}{\partial \eta}} \mu. \quad (1.9)$$

Here, η is the electrochemical potential. Eq 1.9 describes the charge carrier concentration dependent enhancement of the diffusion coefficient due to disorder. At low concentrations, in the so-called Boltzmann limit, the charge carriers act as independent particles and the generalized Einstein relation approaches the classical Einstein relation: $D = \mu k_B T / e$. The formalism given so far was successfully applied to describe the hole transport $J(V)$ characteristics in α -NPD and PF-TAA.^{45,47,48} For the case of electron transport, so-called “trap-states” which may be caused by impurities or imperfections in the chemical structure of the material, often give rise to energetically low-lying states which strongly affect the transport properties. Frequently, trap states are described by an exponential density of states⁴⁹:

$$g(E) = \frac{N_{\text{t,trap}}}{k_B T_0} \times \exp\left(\frac{E}{k_B T_0}\right), \quad (1.10)$$

where T_0 is the trap temperature, $N_{\text{t,trap}}$ the trap site density (the integral of $g(E)$ to $E = 0$) and $E = 0$ is the energy which corresponds to the top of the Gaussian DOS. In Refs. 50 and 51, the influence of traps is taken into account by such an exponential density of states superimposed on the Gaussian DOS. Within this description, hopping between trap sites is neglected, which is a realistic assumption if the density of trap states is low as compared to the density of transport sites in the Gaussian DOS. In this case, the mobility is determined by the density of occupied states at the so-called “transport level”.⁴² If local thermal equilibrium between all carriers is assumed, this density of free carriers n_f follows straightforwardly, using the Fermi-Dirac distribution function, from the total density n_{tot} . The total carrier density is the sum of the density of trapped and free charge carriers. The drift-diffusion equation is in this case slightly modified and reads:

$$J = en_f(n_{\text{tot}})\mu F + eD \frac{dn_f(n_{\text{tot}})}{dx}. \quad (1.11)$$

The current density is determined by the free carrier density (n_f) which is a simple function of the total density. This total density determines the field throughout the material via the Poisson equation. It should be noted that the assumption of an exponential trap DOS is a topic of discussion. For example Nicolai *et al.* have shown in Ref. 44 that a Gaussian trap distribution at an energy level below the top of the Gaussian of the host material can give a similarly good description of the charge transport in several polymers. This approach introduces another parameter, namely the mentioned depth of this Gaussian. This value is not *a priori* known for the polymers and small-molecule based materials studied in this work.

1.3 Scope of this thesis

In this thesis, crucial elements towards the development of a multilayer white OLED device model are presented. The electrical characteristics of layers which consist of polymer and small-molecule based materials are measured and studied to explore the validity of novel methods for OLED device modeling.

In **Chapter 2**, the question is addressed how accurately materials parameters which determine the mobility in single layer devices can be extracted on the basis of $J(V)$ characteristics. An extraction method based on a Gauss-Newton algorithm is developed and thoroughly tested on both hole-only and electron-only characteristics to investigate the accuracy but also the limitations of parameter extraction. It is concluded that for hole transport the extraction is straightforward, in contrast to the case of electron transport where the extraction often requires additional knowledge about the system.

Obviously, if one could use an independent experimental technique to determine one of the parameters involved this would improve the accuracy of electrical characterization. One of the important parameters in single-layer devices is the built-in voltage. This device parameter is defined as the effective work-function difference between the anode and the cathode materials used. To give insight into this parameter, an electroabsorption setup was built and used to study polyfluorene based co-polymer hole-only devices. These devices were already found to be well described using the EGDM, which made it possible to interpret the voltage at which the electroabsorption signal goes to zero in relation to the built-in voltage. A significant difference between both voltages is found. This is explained by charge carrier diffusion in the polymer layer. The results obtained using this method are presented in **Chapter 3**.⁵²

As mentioned, the polyfluorene based co-polymer devices described in Section 1.1.1 are found to be well described using the EGDM. Now the question arises how well the ECDM can describe the transport in these devices. This is investigated using the extraction method discussed above. The results are presented in **Chapter 4**.⁴⁷ It was found that a similarly good fit to the data could be obtained but with an unrealistically high hopping site density. In this way, one may thus make a distinction between both models. We view this as evidence for the absence of correlated disorder in this co-polymer.

Chapter 5 deals with the analysis of electron transport, which is known to be difficult due to an increased experimental uncertainty and two additional parameters (see Section 1.2.3) describing the density of trap states which is present in such materials. The electrical characteristics of the well studied small molecule material Alq₃ are re-analyzed using the EGDM and the ECDM. A good fit quality is found, using a realistic site density with the ECDM. In contrast to the earlier study of these characteristics using a conventional model, a consistent set of parameters is used for all devices studied. Moreover, in contrast to the previous work, the presence of a significant injection barrier is found for the devices studied.

In studying charge transport, it is often found that, in particular for electron transport, charge carrier relaxation effects significantly affect the measurement result. For this reason, **Chapter 6** presents an extension of the model to describe the effect of charge carrier relaxation on the time-dependence of the current-density. For the polyfluorene based co-polymer devices introduced in Section 1.1.1, this is investigated by an EGDM modeling study of the measured dark injection (DI) transients. The influence of (time dependent) relaxation effects on the DI peak position is demonstrated from the comparison between experiment and modeling results.

In **Chapter 7**, the introduced parameter extraction method is applied to Spiro-DPVBi and NET-5 which are small-molecule based materials present in the white multilayer stack mentioned in Section 1.2. The gained knowledge about the electron mobility in this material was used as input for a 3D Monte Carlo simulations of the full stack. This simulation was done by a collaborating group within the project and also uses experimental results on the mobility in the other layers. These results were obtained by collaborating groups and will be referred to. This shows that it is now possible to make a multilayer white OLED model based on experimentally determined mobilities. Finally, a critical comparison between the measured current-density in the stack and the predictions of the 3D model are given to make further improvements possible.

Bibliography

1. J. Kido, M. Kimura, and K. Nagai, *Science* **267** 1332 (1995).
2. Y. Tyan, *Journal of Photonics for Energy* **1**, 011009-1 (2001).
3. B. W. D'Andrade and S. R. Forrest, *Adv. Mat.* **16** 1585 (2004).
4. S. Reineke, F. Lindler, G. Schwartz, N. Seidler, K. Walzer, B. Lussem, and K. Leo, *Nature* **459**, 234 (2009).
5. United States Department of Energy, Multi-year program for Solid-State Lighting (2011), <http://science.energy.gov/>.
6. Z. Yu, X. Niu, Z. Liu, and Q. Pei, *Adv. Mat.* (2011) (to be published).
7. *High efficiency OLEDs for lighting Applications - Completing the Solid State Lighting Portfolio*, C. Verschuren, V. van Elsbergen, and R. Coehoorn, Springer Verlag (2011).
8. Novalled AG, <http://www.novalled.com/>.
9. C. W. Tang and S. A. VanSlyke, *Appl. Phys. Lett.* **51**, 913 (1987).
10. F. Lindla, M. Boesing, C. Zimmerman, P. van Gemmern, D. Bertram, D. Keiper, M. Heuken, H. Kalisch, and R. H. Jansen, *Journal of Photonics for Energy* **1**, 011013 (2011).
11. T. Peng, Y. Yang, H. Bi, Y. Liu, Z. Hou, and Y. Wang, *J. Mat. Chem.* **21**, 3551 (2011)
12. W. Ji, J. Zhao, Z. Sun, and W. Xie, *Org. Electron.* **12**, 1137 (2011).
13. A. Duggal, J. Shiang, C. Heller, and D. Foust, *Appl. Phys. Lett.* **80**, 3470 (2002).
14. S. L. M. van Mensfoort, M. Carvelli, M. Megens, H. Greiner, D. Wehenkel, M. Bartyzel, R. A. J. Janssen, and R. Coehoorn, *Nature Photonics* **4**, 329 (2010).
15. "Advanced Experimentally Validated Integrated OLED Model" (AEVIOM), EU project in the 7th Framework Programme, <http://www.aeviom.eu/>.
16. G. Schwartz, K. Walzer, M. Pfeiffer, and K. Leo, *Proc. SPIE* 61920Q-2 (2006).
17. S. L. M. van Mensfoort, J. Billen, M. Carvelli, S. I. E. Vulto, R. A. J. Janssen, and R. Coehoorn, *J. Appl. Phys.* **109**, 064502 (2009).
18. B. K. Crone, P. S. Davids, I. H. Campbell, and D. K. Smith, *J. Appl. Phys.* **84** 833 (1998).
19. S. J. Konezny, D. L. Smith, M. E. Galvin, and L. J. Rothberg, *J. Appl. Phys.* **99**, 064509 (2006).

20. J. Staudigel, M. Stossel, F. Steuber, and J. Simmerer, *J. Appl. Phys.* **86**, 3895 (1999).
21. J. J. Kwiatkowski, J. Nelson, H. Li, J. L. Bredas, W. Wenzel, and C. Lennertz, *Phys. Chem. Chem. Phys.* **10**, 1852 (2008).
22. V. Rühle, A. Lukyanov, F. May, M. Schrader, Th. Vehoff, J. Kirkpatrick, B. Baumeier, and D. Andrienko, *J. Chem. Theory Comput.* **10**, 3335 (2011).
23. W. F. Pasveer, J. Cottaar, C. Tanase, R. Coehoorn, P. A. Bobbert, P. W. M. Blom, and D. M. de Leeuw *Phys. Rev. Lett.* **94**, 206601 (2005).
24. M. Bouhassoune, S. L. M. van Mensfoort, P. A. Bobbert, and R. Coehoorn *Org. Electron.* **10**, 437 (2009).
25. W. Brütting, S. Berleb, and A. G. Mückl, *Org. Electron.* **2**, 1 (2001).
26. N. F. Mott, *Can. J. Phys.* **34**, 1356 (1956).
27. E. M. Conwell, *Phys. Rev.* **103**, 51 (1956).
28. A. Miller and E. Abrahams, *Phys. Rev.* **120**, 745 (1960).
29. R. A. Marcus, *Rev. Mod. Phys.* **65**, 599 (1993).
30. A. Many and G. Rakavy, *Phys. Rev.* **126**, 1980 (1962).
31. D. Poplavskyy, W. Su, and F. So, *J. Appl. Phys.* **98**, 014501 (2005).
32. P. M. Borsenberger and D. S. Weiss, *Organic Photoreceptors for Xerography* (Dekker, New York, 1998).
33. G. Malliaras, Y. Shen, D. H. Dunlap, H. Murata, and Z. H. Kafafi, *Appl. Phys. Lett.* **79**, 2582 (2001).
34. H. Bässler, *Phys. Stat. Sol. B* **175**, 15 (1993).
35. P. W. M. Blom and M. C. J. M. Vissenberg, *Mater. Sci. Eng., R.* **27**, 53 (2000).
36. M. A. Lampert and P. Mark, *Current Injection in Solids* (Academic, New York, 1970).
37. Y. N. Gartstein and E. M. Conwell, *Chem. Phys. Lett.* **245**, 351 (1995).
38. S. V. Novikov, D. H. Dunlap, V. M. Kenkre, P. E. Parris, and A. V. Vannikov, *Phys. Rev. Lett.* **81**, 4472 (1998).
39. Z. G. Yu, D. L. Smith, A. Saxena, R. L. Martin, and A. R. Bishop, *Phys. Rev. Lett.* **84**, 721 (2000).
40. S. V. Rakhmanova and E. M. Conwell, *Appl. Phys. Lett.* **76**, 3822 (2000).

41. C. Tanase, E. J. Meier, P. W. M. Blom, and D. M. de Leeuw, *Phys. Rev. Lett.* **91**, 216601 (2003).
42. R. Coehoorn, W. F. Pasveer, P. A. Bobbert, and M. A. J. Michels, *Phys. Rev. B* **72**, 155206 (2005).
43. J. Cottaar, L. J. A. Koster, R. Coehoorn, and P. A. Bobbert, *Phys. Rev. Lett.* **107**, 136601 (2011).
44. H. T. Nicolai, M. M. Mandoc, and P. W. M. Blom, *Phys. Rev. B* **83** 195204 (2011).
45. S. L. M. van Mensfoort, S. I. E. Vulto, R. A. J. Janssen, and R. Coehoorn, *Phys. Rev. B* **78**, 085208 (2008)
46. S. L. M. van Mensfoort and R. Coehoorn, *Phys. Rev. B* **78**, 085207 (2008).
47. R. J. de Vries, S. L. M. van Mensfoort, V. Shabro, S. I. E. Vulto, R. A. J. Janssen, and R. Coehoorn, *Appl. Phys. Lett.* **94**, 163307 (2009).
48. S. L. M. van Mensfoort, V. Shabro, R. J. de Vries, R. A. J. Janssen, and R. Coehoorn *Phys. Rev. B* **80**, 033202 (2009).
49. M. M. Mandoc, B. de Boer, and P. W. M. Blom, *Phys. Rev. B* **73**, 155205 (2006).
50. S. L. M. van Mensfoort, R. J. de Vries, V. Shabro, C. van der Marel, H. P. Loebel, R. A. J. Janssen, and R. Coehoorn, *Org. Electron.* **11**, 1408 (2010).
51. S. L. M. van Mensfoort, J. Billen, S. I. E. Vulto, R. A. J. Janssen, and R. Coehoorn, *Phys. Rev. B* **80**, 033202 (2009).
52. R. J. de Vries, S. L. M. van Mensfoort, R. A. J. Janssen, and R. Coehoorn, *Phys. Rev. B* **81**, 125203 (2010).

2

Extraction of the materials parameters that determine the mobility in disordered organic semiconductors

The development of white organic light-emitting diodes (OLEDs), which generally consist of various organic layers with specific functionalities, is hampered by a lack of fast and accurate methods for determining the materials parameters related to the molecular and electronic structure, such as e.g. the width of the density of states (σ) and the hopping site density (N_t). Deriving the parameters from the current-voltage characteristics is a time-consuming process. This hampers progress in the understanding of the dependence of the mobility on field, charge carrier density and temperature in organic materials, which is required for the rational design of multilayer stacks. In the literature, several mobility models have been proposed and experimentally tested using visual means to judge the fit quality. For some intensively investigated OLED materials this has led to a broad spread of published materials parameter values. Therefore the question arises to what extent it is possible to determine the materials and device parameters, based on single organic layer current-voltage characteristics, in a fast, accurate and unbiased manner. We present a quick extraction method which takes into account the experimental uncertainty and which yields the best fit parameters to experimental data, including uncertainty margins in the obtained parameters and including the correlations in these margins. The method makes it possible to quickly make a distinction between different models in a quantitative manner. Furthermore it makes it possible to determine the limitations of parameter extraction methods in cases in which a too large set of free parameters is needed to describe the molecular and electronic structure.

2.1 Introduction

In the past decade, strong progress has been made concerning the description of charge transport processes in disordered organic semiconductors. In particular, enhanced understanding has been obtained of the charge carrier density dependence of the mobility resulting from energetic disorder. Experimental proof of the carrier density dependence of the mobility was obtained from the current density (J) versus voltage (V) characteristics of organic field effect transistors (OFET) and from $J(V)$ characteristics of sandwich-type devices as used in organic light-emitting diodes (OLEDs).^{1,2} When using sandwich-type single-carrier devices, a clear distinction with the previously often used approach, within which the carrier density dependence was neglected and within which an empirical Poole-Frenkel type field dependence ($\ln(\mu) \propto F$) was assumed,^{3,4} may be made by carrying out experiments for various layer thicknesses.⁵ Whereas the $J(V)$ curves of OFETs based on materials with a disordered structure can be consistently described assuming an exponential density of states (DOS),¹ the finding of a constant mobility from the hole-only $J(V)$ characteristics of sandwich-type devices based on various polymers is more consistent with the assumption of a Gaussian DOS.^{6,7} In a Gaussian DOS, the charge carriers act at low carrier concentrations, in the so-called Boltzmann regime, as independent particles. Above a critical carrier concentration, the mobility increases with increasing charge carrier density as low-energy states which would otherwise act as traps are then already filled. For the case of a Gaussian DOS with spatially random site energies, Pasveer *et al.*⁶ obtained accurate expressions for the temperature (T), electric field (F) and charge carrier density (n) dependence of the mobility from three-dimensional modelling (“extended Gaussian disorder model”, EGDM).⁶ An analogous approach for the case of a Gaussian DOS with spatially correlated site energies, by Bouhassoune *et al.*, led to the “extended Correlated disorder model” (ECDM).⁸ Within the ECDM, the field dependence of the mobility is much stronger than in the EGDM, but the carrier density dependence is smaller.

Being able to determine the type of disorder and to accurately extract the materials parameters that determine the mobility in disordered organic semiconductors is of great importance to the rational design of OLEDs, in particular when multilayer stacks are used. The shape of the DOS and the type of disorder (random or spatially correlated) are in general not known *a priori*. Only recently, the feasibility of obtaining such information from first-principles theoretical studies of the molecular and energetic structure of organic semiconductors has been demonstrated, combining molecular dynamics modeling and density functional theory.^{9–11} Analyses of measured $J(V)$ curves of sandwich-type devices have been successfully carried out using the EGDM for several polymers,^{12–15} whereas for several small-molecule materials a more consistent analysis was obtained using the ECDM.^{16–18} However, in these studies no systematic method was applied for obtaining quantified uncertainty margins of the parameters studied and their possible correlations. Furthermore, it has remained unclear to what extent it is possible to make a distinction between different mobility models, e.g. the EGDM and the ECDM.

In this chapter, we investigate these issues in a systematic manner by carrying out a study of the accuracy and limitations of a parameter extraction method based on a Gauss-Newton algorithm.^{19–21}

Within this method, the optimal set of parameter values follows iteratively from a least-squares fit of the measured current density to the current density as calculated assuming a linear sensitivity to a change of the parameter values, around a trial set of parameter values. The algorithm is thus most efficient if the quantity to be analyzed varies approximately linearly with each of the parameter values. In order to more closely achieve this situation, we have chosen to apply the method to the measured $\log_{10}(J(V))$ curves, instead of to the $J(V)$ curves. The method includes the influence of the experimental uncertainty in the measured current density, and provides a covariance matrix which expresses the correlated uncertainties of all parameters. We note that it is not known whether in realistic cases the linearization assumption is valid to a sufficient extent, so that the predicted ellipsoidal confidence regions obtained surrounding the optimal point in parameter space coincide sufficiently well to the confidence regions that would follow from a (time-consuming) brute force approach within which the merit function is calculated explicitly for a dense grid of parameter values surrounding the optimal point. Furthermore, it is not *a priori* clear whether in all cases a unique solution, which is essentially independent of the starting conditions, is found. Indeed, we will show that a unique solution exists often, but not in all cases.

In order to investigate the strengths and limitations of the method used, we study a series of cases with increasing complexity of the problem to be solved, i.e. with an increasing number of parameters. In all cases, single-layer systems are studied with an energy level structure such as shown in Figure 2.1, but with values of the injection barriers such that the transport is unipolar. The transport takes place by hopping of either holes or electrons in between energetically random or spatially correlated states with a Gaussian energy distribution. The mobility is then given by the EGDM and the ECDM, respectively, in which the only materials parameters are the width of the DOS, σ , the total hopping site density, N_t , and the (temperature dependent) mobility in the limit of zero field and zero carrier density, μ_0 . In our analyses, we include a study of the effects of injection barriers (Δ) for holes (h) and electrons (e) at the anode (A) and cathode (C). The built-in voltage V_{bi} is equal to $\Delta_{C,h} - \Delta_{A,h}$ and $\Delta_{A,e} - \Delta_{C,e}$ for the case of hole and electron-only devices, respectively. Furthermore, we study the effect of the presence of a superimposed exponential trap density of states, as often assumed for the case of electron transport^{15,22,23}. The total DOS is then described using two additional parameters, viz. the total density of trap states $N_{t,trap}$ and the characteristic $1/e$ decay energy of the trap DOS, E_0 . We first explore the performance of the method by studying two examples based on artificial noise-containing datasets. It is shown how in an efficient manner a unique solution is found, how a clear distinction can be made between the EGDM and the ECDM, and how as a result of the increasing complexity (more model parameters) of the problems studied the uncertainty regions increase. We show how this uncertainty can be reduced by making use of available experimental information on one of the parameters,

and argue that, in particular when studying electron-transport, this will often be necessary in order to obtain the parameter values with sufficient accuracy. Subsequently, the method is applied to the case of experimental $J(V)$ curves as measured for hole-only¹² and to the case of experimental electron-only¹⁵ devices based on a blue-emitting polyfluorene-triarylamine copolymer (PF-TAA), and a comparison is made with earlier published analyzes. Table 1 gives an overview of the four cases studied.

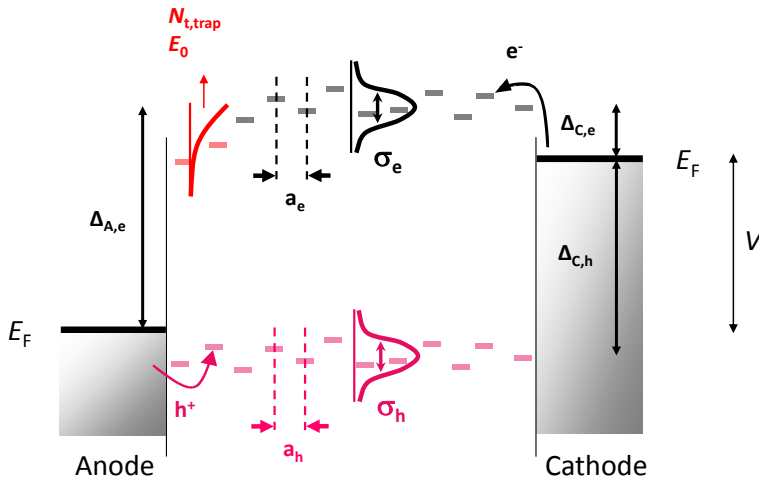


Figure 2.1: Schematic energy level diagram of a double-carrier device indicating all relevant materials and device parameters. For holes (h^+) and electrons (e^-) the widths of the DOS, $\sigma_{e,h}$, the hopping site distances $a_{e,h}$ and the injection barriers Δ at the anode (A) and cathode (C) are indicated. For the electrons, the superimposed exponential DOS is indicated with the two additional parameters involved, E_0 and $N_{t,trap}$. An applied voltage (V) leads to an energy difference between the Fermi levels (E_F) of the anode and the cathode.

In Section 2.2, the method is presented. Section 2.3 contains the application to the two artificial datasets, and in Section 2.4 the method is applied to the hole and electron transport in PF-TAA. Section 2.5 contains a summary and conclusions.

Table 2.1: Overview of the cases studied in this chapter. The description indicates which of the elements, shown in Figure 2.1, are included. A = Artificial data, E = Experimental data.

Section	Data	Description
2.3.1	A	No traps, ideal injecting contact, finite V_{bi} , EGDM and ECDM analysis.
2.3.2	A	Exponential trap DOS, ideal injecting contact, finite V_{bi} , ECDM analysis.
2.4.1	E	No traps, ideal contacts, EGDM and ECDM analysis.
2.4.2	E	Exponential trap DOS, injection barriers at both electrodes, EGDM analysis.

2.2 Method

Within the Gauss-Newton method used, the set of n experimental current densities $J_{\text{exp},i}$ as obtained at various device thicknesses and measurement conditions is analyzed using a set $P \equiv \{P_1, P_2, \dots, P_m\}$ of m parameter values describing the transport. These parameters are chosen to be obtained by minimizing a χ^2 merit function which is here defined as

$$\begin{aligned} \chi^2(P) &\equiv \frac{1}{n} \sum_{i=1}^n \frac{[\log_{10}(J_{\text{model},P,i}) - \log_{10}(J_{\text{exp},i})]^2}{\alpha_i^2} \\ &\equiv \frac{1}{n} \sum_{i=1}^n F_{P,i}^2. \end{aligned} \quad (2.1)$$

In this expression, $\log_{10}(J_{\text{model},P,i})$ is the logarithm of the predicted current density, and α_i is the standard deviation of the measured logarithm of the current density, in both cases for the i -th experiment. Choosing the logarithm of the current density as the observable is found to provide a quite linear variation of the observable with the parameters to be determined. The experimental uncertainty in the observable is assumed to be normally distributed. For the same reason, we have chosen the logarithms of N_t , $N_{t,\text{trap}}$, and of μ_0 as the parameters to be determined. In practice, the experimental data points are obtained by varying for a given type of device the voltage, layer thickness L , and temperature T .

Efficiently minimizing $\chi^2(P)$ is an iterative procedure. First, for the previously determined ‘‘old’’ parameter set the partial derivatives of J with respect to the value of each of the parameters is calculated. Subsequently, the partial derivatives of F are obtained, and a Taylor expansion of $\chi^2(P)$ of the form

$$\chi_{\text{new}}^2 = \min_{\Delta P_j} \left\{ \frac{1}{n} \sum_{i=1}^n [F_i(P_{\text{old}}) + \sum_{j=1}^m \frac{\partial F_i}{\partial P_j} \Delta P_j]^2 \right\} \quad (2.2)$$

is used to predict the optimal change ΔP_j of each of the parameters ($j = 1, 2, \dots, m$), leading by minimization to a new prediction for χ^2 . This procedure is iterated until self-consistency is reached.

It is not *a priori* clear whether the approach described above will give rise to a unique solution in all cases. It cannot be excluded that the function $\chi^2(P)$ shows multiple local minima, e.g. as a result of the experimental uncertainties, as a result of the use of an insufficiently rich experimental data set, or as a result of the use of an incorrect transport model. We will investigate this explicitly for several cases by repeating the iterative procedure after starting at different initial points in the parameter space. Furthermore, it is not in all cases *a priori* clear whether the model used will actually provide a good description of the transport process in the material investigated. One may expect that the final “observed” value for the merit function, χ^2_{obs} , is then significantly larger than the statistically expected value. In order to investigate this, one may carry out a so-called “ χ^2 -test”,²¹ making use of the probability density function of the χ^2 distribution

$$f_{\chi^2}(x) = \frac{1}{2^{\nu/2}\Gamma(\nu/2)} x^{\frac{1}{2}\nu-1} e^{-x/2}, \quad (2.3)$$

where $\nu = n - m$. If the mathematical model used is correct and if the experimental errors are normally distributed and correctly estimated, the value of the parameter

$$p = \int_{\chi^2_{\text{obs}}}^{\infty} f_{\chi^2}(x) dx \quad (2.4)$$

is expected to be uniformly distributed between 0 and 1. The finding of a value of p very close to 1 would provide an indication that the model used is incorrect or incomplete. The finding of a very small value of p , close to 0, might indicate that the experimental errors have been overestimated. The χ^2 -test thus provides a tool for validating a certain transport model.

The uncertainty margins in the parameters are fully quantified by the covariance matrix C , defined as

$$C = (A^T \cdot A)^{-1} \quad (2.5)$$

with $A \equiv (\partial F_i / \partial P_k)$. The diagonal elements C_{jj} are equal to the square of the standard deviation of the parameter P_j . In this chapter, the 95% confidence intervals are given for the normal distribution assumed. The half-width is then equal to $1.96 \cdot C_{jj}^{1/2}$.

Often, correlations between the parameters are significant. Their pairwise correlation is expressed by the correlation matrix. The matrix elements are defined as $\rho_{ij} \equiv C_{ij} / \sqrt{C_{ii} \cdot C_{jj}}$, a number in between -1 and +1. The standard deviations provide only the widths of the probability distributions for each single parameter. They take the complexity of the problem, within which the parameter values may be correlated, into account, but they do not yet provide the *joint* m -dimensional probability distribution which would be needed to make a prediction of the uncertainty of the predicted current density in a device. In this joint probability distribution the contours of equal probability density (expressed in terms of dimensionless units, i.e. by expressing the parameter values in units of

the standard deviation) are m -dimensional ellipsoids centered around the optimal point.²¹ These ellipsoids enclose joint uncertainty regions, corresponding to a certain level of confidence.

In this chapter, we show as an example for the case of an artificial dataset the 95% confidence ellipsoid around the selected parameter value point P , containing with a 95% probability the outcome of the extraction procedure if noise is included (see Section 2.3.1). It may be obtained from the covariance matrix using

$$UC^{-1}U^T = \Delta_m^2, \quad (2.6)$$

where U is the vector (u_1, u_2, \dots, u_m) , with u_j the deviation of the j th parameter from the optimal value, and where Δ_m^2 is the 95th percentile of the χ^2 -distribution with m degrees of freedom. The half-widths of the projection of these 95% confidence ellipsoids on the P_j axes are equal to $\Delta_m \cdot C_{jj}^{1/2}$. The value of Δ_1 is equal to 1.96, and Δ_m increases with increasing m .

2.3 Parameter extraction on artificial data - two case studies

2.3.1 Ideal injecting contact and no trap states

In the first case study, we show how the method can be applied to a material containing no trap states, in a device with an ideal injecting contact. For this purpose, we make use of a set of $J(V)$ curves which have been calculated using the ECDM.⁸ In order to study the effect of experimental uncertainty on the current measurement, noise at a level of 10 percent of the current density, and normally distributed on a $\log_{10}(J)$ -scale, was added to these artificial data. These curves are shown in Figure 2.2 (symbols), for organic layer thicknesses equal to 67 and 122 nm and for three temperatures (272, 213 and 170 K), using $\sigma = 0.09$ eV, $N_t = 5 \times 10^{27} \text{ m}^{-3}$, $V_{bi} = 1.7$ V, and a temperature dependence of the mobility in the limit of zero field and zero carrier density given by

$$\mu_0(T) = \mu_0^* \exp\left[-C\left(\frac{\sigma}{k_B T}\right)^2\right], \quad (2.7)$$

with $C = 0.30$, a typical value expected within the ECDM,⁸ and with $\mu_0^* = 1 \times 10^{-9} \text{ m}^2/(\text{Vs})$. The $J(V)$ curves were calculated using a method for solving the 1D-continuum drift-diffusion equation described in Ref. 12. In Figure 2.2, the solid lines show the result of a best fit to these data as obtained using the method described above and making use of the ECDM. In order to investigate to what extent it would be possible to make a distinction with the EGDM,⁶ a second fit was made to the data assuming the latter model (dashed lines). Figure 2.2 clearly shows that the fit quality as obtained using the ECDM is significantly higher than as obtained using the EGDM. It is thus indeed possible in this case to make a distinction between both models.

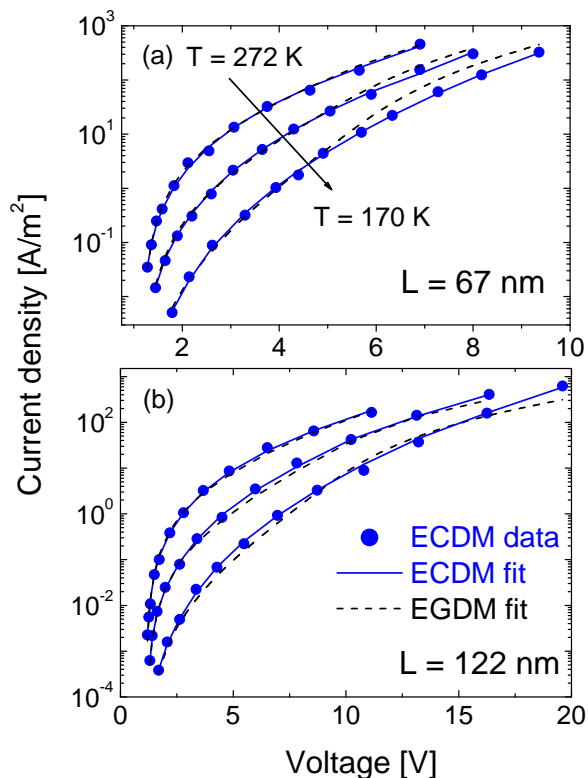


Figure 2.2: $J(V, L, T)$ characteristics, generated using the ECDM with 10% random noise on $\log_{10}(J)$ (\bullet), obtained from a fit using the ECDM (solid lines) and obtained from a fit using the EGDM (dashed lines), for an organic layer thickness equal to 67 nm (a) and 122 nm (b) and for a temperature equal to 272, 220 and 170 K. The parameter values used for generating the curves are given in the text.

In Figure 2.3, a more detailed analysis of the fit results is given. Figure 2.3(a) shows the evolution of the χ^2 -value as a function of the iteration number. The Λ CDM-fits are found to converge within four iterations to a stable χ^2 -value very close to 1. Figure 2.2 also shows the EGDM-results, obtained after starting at two different positions in parameter space (see below). Again, fast convergence is obtained, in the EGDM-case to $\chi^2 \approx 4$. A χ^2 -test (see Section 2.2) yields in these cases $p = 0.1$ and $\sim 2 \times 10^{-17}$. The former value is consistent with the use of the correct physical model, whereas the latter rather extreme value is consistent with the fact that an incorrect model has been used. In a more quantitative manner, this thus confirms that it is indeed possible to make a distinction between both models on the basis of an analysis of $J(V)$ curves. Figure 2.3(b) shows the sequence of the parameter values σ and N_t obtained. The Λ CDM-sequence shows that the final parameter values are not necessarily monotonically approached, but that the final values (solid symbols) obtained are very close to the initial values used (cross). The two EGDM-sequences converge to essentially the same end point, independent of the largely different starting points. The σ -value obtained is only slightly different from the value assumed. However, the site density N_t obtained is approximately a factor 50 smaller than the value assumed. This huge difference thus provides additional information from which it is possible to discriminate the EGDM and the Λ CDM on the basis of the site density obtained, if this parameter is experimentally known, as suggested in Ref. 16. Figure 2.3(c) shows that the values of $\mu_0(T)$ as obtained within the EGDM vary linearly (on a log-scale) with $1/T^2$, with a slope ($C \sim 0.42$, as defined in Eq. 2.7) which is significantly larger than for the values of $\mu_0(T)$ set to calculate the Λ CDM-based $J(V)$ curves used. In view of the linearity of the temperature dependence obtained and in view of the finding of a slope-parameter which is within the range expected for the EGDM,^{6,24} it is in this case not possible to use the temperature dependence of $\mu_0(T)$ to make a distinction between both models.

In Table 2.2, an overview is given of the parameter values obtained from the Λ CDM fit and the confidence intervals. The confidence intervals are quite small. Therefore a symmetric confidence interval has been given for N_t and μ_0 instead of the slightly asymmetric interval which follows from considering the logarithms of these parameters as the quantities used in the fitting procedure. The joint probability distribution is better represented by giving confidence ellipsoids, as discussed in Section 2.2. Figure 2.3(d) gives the projection of the five-dimensional 95%-confidence ellipsoid on the (σ, N_t) -plane. The figure reveals a strong correlation between both parameters, corresponding to a correlation coefficient equal to 0.7. The ellipsoid extends in the long direction to the region outside the individual-parameter confidence interval given in the table, in this five-dimensional case to maximum deviations from the optimal fit value of each of the parameters equal to 3.33 ($= \Delta_5$) times their standard deviation.

From Figure 2.3(b), it was found that the site density can be used to distinguish both models, as a factor of 50 difference with a quite small uncertainty margin was found. Now the question arises to what extent for any arbitrary (σ, N_t) combination an analysis using an incorrect model gives rise to a significantly different value of N_t . To investigate this, a single artificial noise-free $J(V)$ curve was

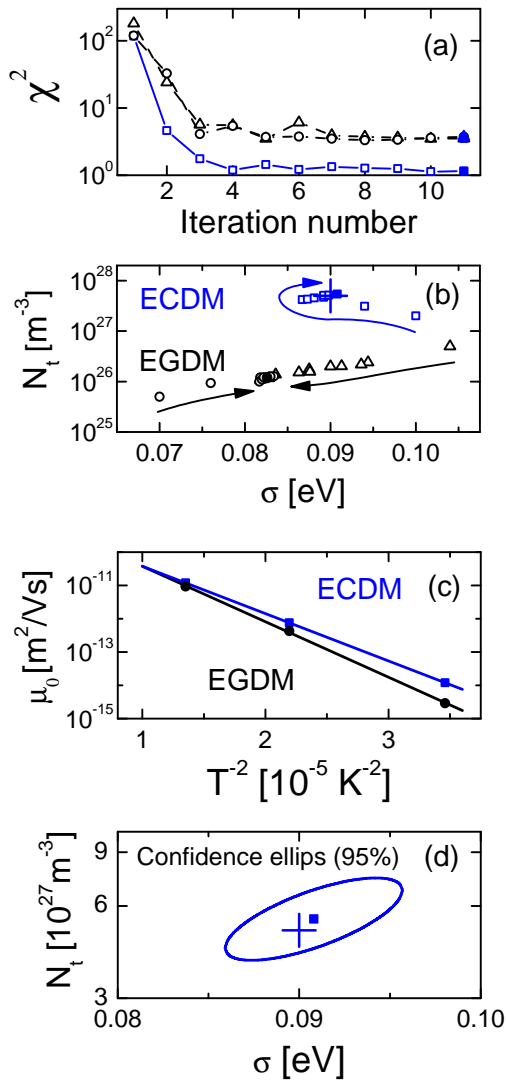


Figure 2.3: Results of the ECMD and EGDM analyses presented in section 2.3.1. (Un)converged results are indicated by open (filled) symbols. The plus symbols indicate the starting values of the parameters. (a) Sequence of χ^2 -values as obtained using the ECMD (\square) and the EGDM (\triangle and \circ), in the latter case resulting from two different starting points. (b) Trajectories in the (σ, N_t) -plane corresponding to the sequences shown in panel (a). (c) Temperature dependence of μ_0 (symbols) and best fits based on Eq. 2.7 (solid lines). (d) Projection of the full 95% confidence ellips on the (σ, N_t) -plane.

Table 2.2: Initial and obtained parameter values for the ECDM case studied in Sections 2.3.1 and 2.3.2.

Parameter	Initial	Obtained Section 2.3.1	Obtained Section 2.3.2
N_t [10^{27} m^{-3}]	5.0	5 ± 1	4.5 ± 1
σ [meV]	90	90 ± 3	89 ± 4
V_{bi} [V]	1.7	1.71 ± 0.01	1.69 ± 0.02
$\mu_0(272 \text{ K})$ [$10^{-11} \text{ m}^2/(\text{Vs})$]	1.2	1.17 ± 0.09	
$\mu_0(214 \text{ K})$ [$10^{-13} \text{ m}^2/(\text{Vs})$]	7.6	8 ± 1	
$N_{t,\text{trap}}$ [10^{24} m^{-3}]	2.0		1.6 ± 0.4
E_0 [meV]	103		107 ± 4
$\mu_0(300 \text{ K})$ [$10^{-11} \text{ m}^2/(\text{Vs})$]	2.6		2.5 ± 0.2
$\mu_0(170 \text{ K})$ [$10^{-14} \text{ m}^2/(\text{Vs})$]	1.2		1.2 ± 0.4

generated using both the EGDM and the ECDM at 273 K for 100 nm devices with a built-in voltage of 1.7 V, no barrier at the injecting contact, $N_t = 1 \times 10^{27} \text{ m}^{-3}$ (ECDM) and $N_t = 5 \times 10^{26} \text{ m}^{-3}$ (EGDM), for values of σ in the range 0.07 to 0.14 eV. A least-squares fit using the other model shows then how the initial points in either parameter space are projected to points in the other parameter space. The obtained values of V_{bi} and μ_0 were found to be only marginally different from the initial values. Figure 2.4 gives an overview of the resulting projection in the (N_t, σ) -space. In order to investigate the sensitivity of the projection to the other initial parameters used, the calculations starting from an ECDM- $J(V)$ curve obtained using $\sigma = 0.1$ eV were repeated three times, viz. using $T = 173$ K, $L = 300$ nm, and using a 0.4 eV barrier at the injecting contact. Only very small changes of the end points were found, indicating that the projection shown in Figure 2.4 is not very sensitive to the temperature, layer thickness and barrier at the injecting contact used. It can clearly be seen that applying the ECDM to the EGDM-data leads to a substantially higher site density, about a factor of 20, whereas about the same σ -value is obtained. Similarly, applying the EGDM to the ECDM-data leads to a substantially lower site density, about a factor of 10-100. Also in this case the σ -values are only slightly different, up to 0.015 eV at most. The effect on N_t is consistent with the results of earlier analyses of experimental data on various materials (PF-TAA,¹⁶ α -NPD,¹⁸ and BAQ¹⁷), in which a similar substantial difference in site density was found. That made it possible (together with the known experimental site density) to make a distinction between both models.

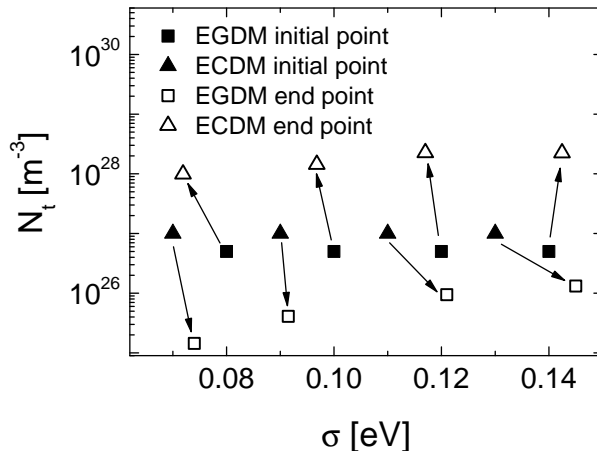


Figure 2.4: Fit parameters (open symbols) obtained using the EGDM and the ECDM for $J(V)$ curves generated using the other model and using the initial σ and N_t parameter values indicated by the solid symbols. The calculations were carried out for 100 nm thick devices assuming $T = 273$ K. The other initial parameters are given in the text.

2.3.2 Material with trap states

As a next step, the ability of the method to accurately determine the material and device parameters from an analysis of current-voltage curves was investigated for a more complex case, with more free parameters, viz. for a material with a realistic small exponential density of trap states. The analysis was applied to an artificial data set consisting of four $J(V)$ curves generated at 300 and 170 K for a layer thickness of 100 and 300 nm using the ECDM. Noise (10% on $\log_{10}(J)$) was added to the data to mimic the experimental uncertainty. An ECDM-analysis was used to investigate the effect of this level of noise on the uncertainty of the parameter values obtained. A χ^2 -test was found to yield $p = 0.4$, consistent with the use of the correct model to analyze the data. An overview of the parameter values assumed and obtained is given in Table 2.2.

Table 2.2 shows that, using the methodology described in Section 2.2, all seven parameters are found to be equal to the initial values, within the confidence intervals. In order to further analyze the consistency of the approach and the consistency of the parameters obtained, we have investigated the variation of χ^2 as a function of σ , around the optimal point.

In Figure 2.5(a) the solid curve shows the predicted function $\chi^2(\sigma)$, as obtained from the linear least-squares method used. Within the σ -interval shown, a sig-

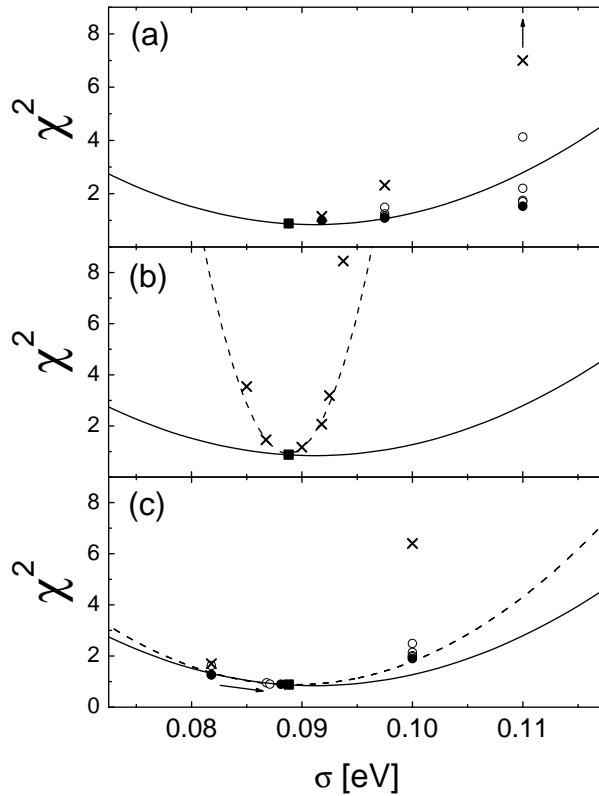


Figure 2.5: Results of the ECDM analysis presented in Section 2.3.2. Full curves: predicted $\chi^2(\sigma)$ curve around the best fit σ -value. Solid square: point at which the extraction procedure was terminated (further iterations only lead to small noisy variations of this endpoint). The crosses indicate the actually obtained χ^2 -value at several σ -values. Subsequently, parameter extraction under the constrained of a fixed value of σ gives the open spheres and converges at the solid spheres. (a) The arrow indicates that the value of the upper datapoint (cross) at $\sigma = 0.11$ eV is actually at $\chi^2 \approx 300$ which is far outside the frame of the figure. (b) The predicted χ^2 curve (dashed) if only the mobility parameters μ_0 are free. (c) The predicted χ^2 curve (dashed) if every parameter is free except for the hopping site density (N_t). Again, the crosses show the actually obtained χ^2 values and the spheres show the result of parameter extraction at that σ -value. If subsequently all parameters are left free, the initial σ -value is reproduced as investigated for the case starting with $\sigma = 0.082$ eV and as indicated by the arrow.

nificant increase of χ^2 above the minimum value is expected. In order to test the validity of this prediction, we first calculated the value of χ^2 for various fixed values of σ , taking all other parameters equal to their predicted optimal value at that value of σ (crosses in Figure 2.5(a)). We find that in all cases these explicitly calculated values of χ^2 are larger than the predicted values. The difference increases with increasing σ -distance from the optimal point. Starting with these estimated solutions, we subsequently calculated for all these fixed σ -values the value of χ^2 without introducing any other constraint. The solid spheres in Figure 2.5(a) give the final results, while the open spheres give the intermediate results obtained during the iterative procedure. The χ^2 values obtained using the predicted parameter values are found to be larger than the expected values. However, the subsequently obtained χ^2 values (closed spheres) after parameter extraction (all parameters free) are at every σ value smaller than as predicted. This shows that in this case the linearization assumption gives rise to an underestimation of the uncertainty of the parameter values obtained. In order to investigate how, within the scope of the method, the uncertainty in the parameter values could be improved, we have studied the effect of reducing the number of free parameters. The dashed curve in Figure 2.5(b) shows the predicted $\chi^2(\sigma)$ curve as obtained from the linear least-squares method used when leaving only the mobility (at the two temperatures considered) as a free parameter while taking all other parameters, except for σ , equal to the values given in Table 2.2. Similarly, in Figure 2.5(c) all parameters are left free except for the hopping site density N_t . It can be seen that the linearization approach provides a quite accurate prediction when only the mobility is treated as a degree of freedom. Furthermore, when leaving all parameters free apart from N_t , the prediction still somewhat differs from the explicitly obtained results. However, from the finally obtained $\chi^2(\sigma)$ -points the optimal value of σ (and of the other parameters) may be determined with a smaller uncertainty than when not constraining any parameter value. As for many materials N_t is expected to be equal to the molecular site density, which may be determined accurately from the density and molecular weight of the material, we view constraining its value as a realistic and practical approach towards extracting the other parameter values with increased accuracy.

2.4 Application to hole and electron transport in PF-TAA

2.4.1 Hole transport

As a next step, the method is applied to previously published hole-only and electron-only $J(V)$ curves for devices based on a blue-emitting polyfluorene with triarylamine units (PF-TAA),^{12,15,16} and a comparison is made with the uncertainty estimates as obtained in these studies in a much more time-consuming manner by exploring possible solutions on a grid consisting of a large number of points in parameter space surrounding the optimal point. The hole-only devices studied have the structure

| Glass | ITO | PEDOT:PSS | PF-TAA | 100 nm Pd |,

with an indium tin oxide (ITO) / poly(3,4-ethylenedioxythiophene):poly(styrene sulfonic acid) (PEDOT:PSS) anode layer, the PF-TAA light-emitting layer, and a palladium cathode. The structure and functioning of the PF-TAA copolymer have been described in Ref. 12. We employed the measured $J(V)$ curves at 272 and 215 K for device layer thicknesses of 67 and 122 nm, given in this work. Furthermore, we have investigated the experimental uncertainty in the measured current density by repeatedly re-measuring the $J(V)$ characteristics of the same devices at each temperature and layer thickness. A statistical analysis revealed an approximately Gaussian distribution with a standard deviation on $\log(J)$ of about 4% at 273 K. Reanalyzing the $J(V)$ characteristics using the EGDM, including the uncertainty in the measured current-density, led to quick convergence to the same end point, independent of the initial conditions. Within the analysis, all parameter values were treated as identical for each layer thickness, apart from the value of V_{bi} , which is known to show in practice small sample-to-sample variations. The χ^2 value was ~ 10 , which leads to $p = 10^{-75}$. We view these values as an indication that the procedure underestimates the experimental uncertainties, which actually also contain a contribution due to an uncertainty in the layer thickness and measurement temperature. The influence of the latter uncertainties are described in more detail in the Appendix. However, we cannot exclude that the EGDM does not provide a sufficiently accurate description of the transport process, which would also lead to an unacceptably high value of χ^2 . The total uncertainty of the parameter values is expressed as a sum of contributions from the covariance matrix analysis, assuming the nominal values of L and T , and a contribution which is due to the experimental uncertainty in L and T . For this case, with five parameters, the Gauss-Newton extraction method requires approximately 10 times less $J(V)$ curve calculations as compared to the previously used “grid approach”.¹⁶ Within that approach, χ^2 is calculated on a dense grid of parameter value combinations. Using the Gauss-Newton method significantly reduces the calculation time required for an extraction. The method only yields a linear increase in calculation time with every additional parameter, whereas a power law increase is obtained using the grid approach. Herewith, the benefit of the extraction method increases rapidly with increasing amount of parameters.

Table 2.3 gives an overview of the modelling results, and includes a comparison with the results obtained in Ref. 12. It may be seen that within the uncertainty margins essentially the same parameter values were obtained, albeit with a larger and smaller uncertainty margin for the cases of N_t and σ , respectively. This confirms the validity of the earlier results and shows how the Gauss-Newton method can be used as a quick method for extracting the transport parameters and their uncertainties.

In Section 2.3.1 it was argued that it is in principle possible to make a distinction between the EGDM and the ECDM on the basis of the χ^2 -value obtained. However, that would require that the experimental uncertainties are small and well-understood. We find that a re-analysis of the data using the ECDM leads to a fit with a similar χ^2 value as for the EGDM, $\chi^2 \approx 10$, and with an unrealistically

Table 2.3: EGDM parameter values describing the current density in the PF-TAA based hole-only devices discussed in Section 2.4.1, as obtained in Ref. 12 and as obtained in this chapter. For the 67 and 122 nm devices slightly different values of V_{bi} were found in both studies.

Parameter	Ref. 12	This chapter
N_t [10^{26} m^{-3}]	6 ± 1	6 ± 3
σ [eV]	0.13 ± 0.01	0.128 ± 0.003
$V_{bi}(67 \text{ nm})$ [V]	1.75 ± 0.05	1.77 ± 0.05
$V_{bi}(122 \text{ nm})$ [V]	1.95 ± 0.05	1.90 ± 0.03
$\mu_0(272 \text{ K})$ [$10^{-13} \text{ m}^2/(\text{Vs})$]	9 ± 4	7 ± 3
$\mu_0(215 \text{ K})$ [$10^{-16} \text{ m}^2/(\text{Vs})$]	6 ± 4	8 ± 5

large site density. The χ^2 -value is, again, larger than the value expected when only random errors in the current density measurement would play a role. The finding of a similar ECDM and EGDM fit quality and essentially the same high ECDM hopping site density was reported previously in Ref. 16. This confirms that in practice a distinction between both models is most easily made on the basis of the site densities obtained, if the experimental value of N_t is known. Only a strong reduction of the uncertainties in the experimental values of L and T would, in this case, make it possible to make a distinction on the basis of the fit quality. We find that a different situation arises when considering the Poole-Frenkel model, within which the mobility is given by

$$\mu = \mu_{0,PF}(T) \exp^{-\gamma(T)\sqrt{F}}. \quad (2.8)$$

Here, γ is an empirical temperature dependent parameter and F the electric field. This model, applied to the hole-only $J(V)$ curves, leads to $\chi^2 \approx 50$. The EGDM (with $\chi^2 \approx 10$) provides thus a significantly better description of the data. The conclusion from this quantitative analysis is consistent with the more qualitative analysis given in Ref. 12.

2.4.2 Electron transport

The extraction of the parameters which determine the transport in electron-only devices is generally more difficult than for hole-only devices due to the presence of additional traps. In the presented modeling study, an exponential trap DOS is assumed. Also the presence of a barrier at the electron injecting contact often plays a role. In order to investigate the accuracy with which the transport parameters can be determined in such a case, we apply the Gauss-Newton method to the dataset presented in Ref. 15, comprising $J(V)$ curves measured for devices with the structure

$$[\text{glass} | \text{Al} | \text{PF-TAA} | \text{LiF} | \text{Ca} | \text{Al}] ,$$

with 96, 129, and 149 nm PF-TAA layer thicknesses. The 129 nm devices were studied as a function of the temperature in the 193 to 295 K range in 20 K steps (see Ref. 15 for the details), whereas the other two devices were studied at room temperature (295 K). An EGDM based one-dimensional device model was employed which takes into account the presence of a small barrier of 0.3 eV at the electron injecting contact. Within this study, it was chosen to keep this value fixed. It should be noted however that although the value of 0.3 eV is in line with the value obtained in Ref. 15, the claimed uncertainty margin of 0.1 eV is considered to be realistic. Therefore it should be mentioned that using a barrier of e.g. 0.4 eV will change the extraction results presented here. Herewith the main value of the presented approach is to find out how well it is possible to independently determine the transport parameters. In the model, a correction to the injection barrier due to the image charge effect is taken into account as described in Ref. 25. We find that the correction only has a minor effect since only at rather high voltages a small lowering of the barrier is found.

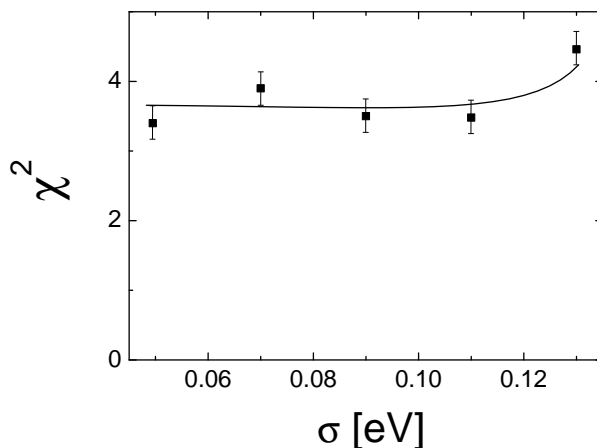


Figure 2.6: Obtained best fit χ^2 values as a function of the width of the density of states σ , for the case studied in Section 2.4.2. The uncertainty margins of every point and a guide-to-the eye (drawn curve) are shown.

Using the method, quick convergence was found for the $J(V,L,T)$ characteristics using in total 4 free materials and device parameters: the mobility μ_0 , the hopping site density N_t , the volume density of trap sites $N_{t,\text{trap}}$, and the built-in voltage V_{bi} . The width of the density of states, σ , was kept fixed and the calculation was repeated for a series of values of σ from 0.05 to 0.13 eV in steps of 0.02 eV. Using the method, quick convergence was found in all cases. However in contrast to the other studies discussed in this chapter, it was found that for a

broad range of σ values [0.05 - 0.11 eV] a very similar χ^2 value (around 4) could be obtained, as can be seen in Figure 2.6. Therefore the fit quality cannot be used to accurately determine the parameters. The uncertainty margins and a trendline to the obtained χ^2 values are also shown in Figure 2.6. From these it can be seen that the χ^2 value found at $\sigma = 0.13$ eV is somewhat higher than for the lower σ values. Herewith, from a point of view of fit quality, the σ values below 0.13 eV are more likely. It should however be noted that since the obtained χ^2 values are significantly higher than 1, which would not be expected for a physically fully correct model, these relatively small differences must not be overinterpreted.

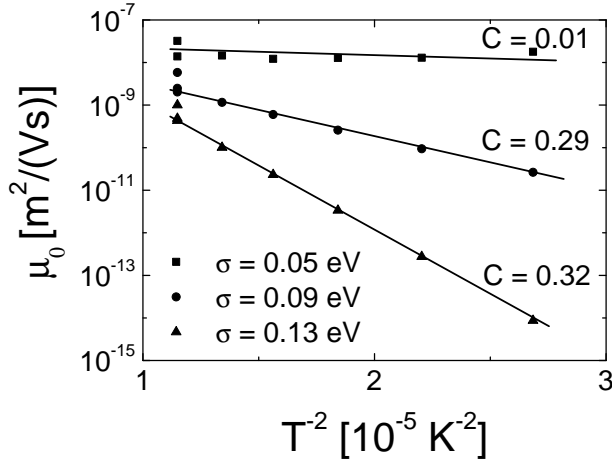


Figure 2.7: Obtained best fit temperature dependence of the mobility μ_0 for three different values of σ . The values of the slope parameters C (see Eq. 2.7) to the best fit of the data (lines) are shown.

Figure 2.7 shows the corresponding values of $\mu_0(T)$. Clearly, a very different temperature dependence of μ_0 is obtained for each σ value studied. From the EGDM theory, the dimensionless slope of these lines, indicated by the C -value defined by Eq. 2.7, is expected to be in the range 0.38 to 0.5. Therefore, the obtained values (0.29 to 0.32 for $\sigma > 0.09$ eV, see Figure 2.7) are rather low. At $\sigma = 0.05$ eV, in particular the C -value is unphysically small. Herewith $\sigma = 0.05$ eV is considered to be not a realistic value for the width of the DOS.

Figure 2.8 gives an overview of the parameter values obtained at each σ value studied. In panel (a) of Figure 2.8, a subtle decrease of the obtained hopping site density can be seen. However, all N_t values lie in the range $(1.0 \pm 0.5) \times 10^{27} \text{ m}^{-3}$, which is expected for PF-TAA.¹⁵ Therefore, no discrimination between the results obtained at the different σ values can be made based on N_t . Panel (b) shows a gradual increase in the trap density $N_{t,\text{trap}}$ obtained with increasing σ

value. Similarly, no discriminating conclusion can be drawn from this result since no material specific knowledge on the expected volume density of trap sites is available.

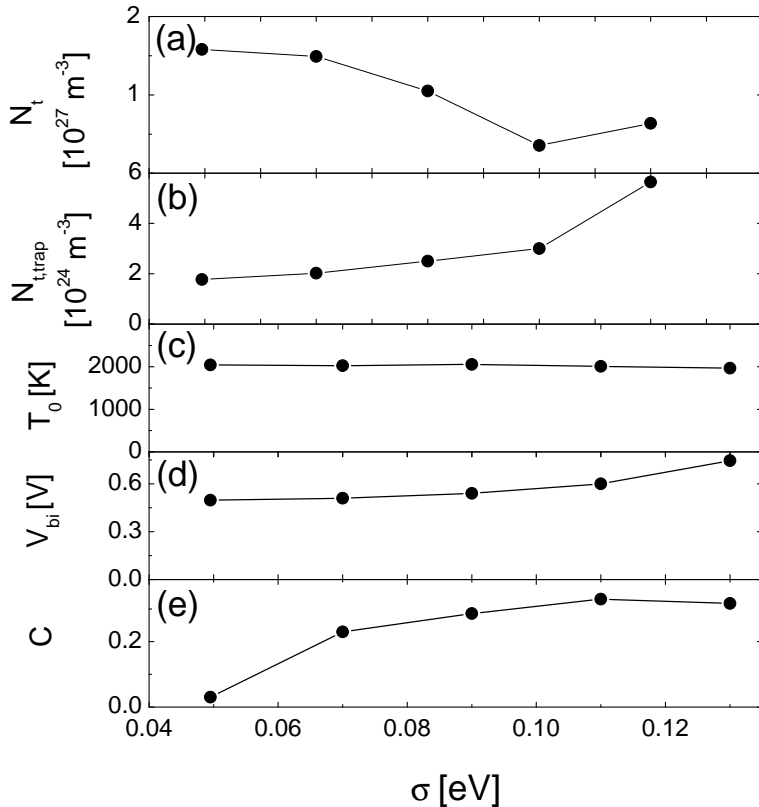


Figure 2.8: Obtained best fit parameters as a function of the width of the density of states σ , for the case studied in Section 2.4.2. (a) A gradual decrease of the obtained site density N_t can be seen. Panel (b), (d), and (e) show an increase in the obtained trap density ($N_{t,\text{trap}}$), built-in voltage (V_{bi}), and C parameter, respectively. (d) Shows the obtained T_0 parameter which is found to be independent of the σ value.

Figure 2.8(c) shows that a very similar value of T_0 is obtained for every σ value studied. This can be understood from the fact that this parameter is strongly determined by the slope of the studied $J(V)$ characteristics on a log-log scale.²⁶ T_0 can thus be determined independent of the other parameters with a rather high

accuracy. The built-in voltage shown in panel (d) shows a small increase with increasing σ value. Also here, no detailed information on the expected built-in voltage is known and no discrimination can be made between the results obtained at the different σ values. Additionally, one could perform electroabsorption or capacitance voltage measurements to independently judge the accuracy of the value of the built-in voltage obtained.²⁷ In panel (e) of Figure 2.8, the increase in the obtained C parameter with increasing σ value is shown. This result was already discussed in relation to Figure 2.7.

Overall one can state that a more accurate extraction of the various transport parameters would require a richer dataset or additional specific information about the material or devices studied. Such knowledge can serve as an input parameter in the model. As an example, having prior knowledge about the expected hopping site density N_t , would be useful since it can reduce the amount of degrees of freedom. For materials such as PPVs for which the value of N_t for HOMO and LUMO states is expected to be very similar, such information can be obtained from a hole-only study.²³ However in this case PF-TAA with hole-transporting units is used and the hopping site density for electrons is different from that for the holes. Therefore more accurate knowledge about the expected N_t value is not available.

2.5 Summary and conclusions

The Gauss-Newton extraction method was applied for quickly deducing the materials and device parameters which determine the mobility in an organic material from the $J(V)$ characteristics. We determined the accuracy and limitation of its application to realistic organic semiconductor devices. For selected cases, the experimental uncertainties were quantified using a statistical analysis of the experiments and the parameter uncertainties and parameter correlations were quantified using co-variance matrices.

Applying the method to generated ECDM hole transport data with additional noise using both the EGDM and the ECDM showed convergence in less than 10 iterations to a unique point in the parameter space. The obtained hopping site density is significantly different for both models. Therefore a comparison with the experimental site density can be used to discriminate the models. Since both extractions lead to a temperature dependence of the mobility which is well described using equation 2.7 with a value for the C parameter which is consistent with the value range expected for each model, the obtained temperature dependence of the mobility cannot discriminate both models. The method was also tested on generated electron transport data with additional noise. The presence of additional parameters, describing the shape of the trap DOS, made the extraction more difficult. As more parameters are present, the obtained uncertainty margins are larger. Reducing the uncertainty margins is shown to be possible by fixing the site density N_t .

As a next step, the method was applied to measured hole and electron $J(V)$ transport characteristics of PF-TAA. For the hole transport, much quicker con-

vergence to very similar parameter values as obtained in a previous study was found.¹² For this case, the influence of the experimental uncertainty in the organic layer thickness and temperature on the determined parameters is taken into account. A comparison with the empirical PF model showed that a significantly higher fit quality is obtained using the EGDM. A quantitative comparison between different mobility models can be made using the method. For the electron transport characteristics of PF-TAA, a similar fit quality was obtained for a rather wide range of combinations of the parameters which describe the shape of the density of states. A distinction between different best fit parameter combinations can thus be made by the shape and slope of the obtained $1/T^2$ temperature dependence of the mobility μ_0 . In particular at $\sigma = 0.05$ an unrealistically low slope parameter is found. A more accurate determination of the electron transport parameters requires a richer dataset or additional information about the material or devices studied. One could perform electroabsorption or capacitance voltage measurements to independently judge the accuracy of the value of the built-in voltage obtained.²⁷ Previously, it was found that for PPVs a hole-only study can give valuable information about the site density for electron transport.²³ For polyfluorene with hole transport units a different electron transport site density is however expected since the transport is via the polyfluorene. Herewith, no additional information about the electron transport site density can be obtained from comparing with the previous hole-only study.

The extraction method presented shows that quick, robust and proper convergence is possible for the hole-only studies presented and that uncertainty margins on the determined parameters can be quantified. Moreover it was shown how the method can be used to investigate whether the electron transport parameters can be determined unambiguously given a certain dataset and model. As a next step, “design of experiment” can be used to investigate which experiment can be most efficiently added to make a more unique extraction possible.

2.6 Appendix A - Experimental uncertainty

Within the Gauss-Newton parameter extraction method the experimental uncertainty in the observable is assumed to be normally distributed. In order to verify this assumption and to quantify the experimental uncertainty for a typical experimental case, the current-density was measured multiple times for a hole-only device of the type studied in section 2.4.1 at a fixed voltage and temperature. Figure 2.9 shows the result of a statistical analysis of the data. It can be seen that data are indeed fairly well described by a normal distribution.

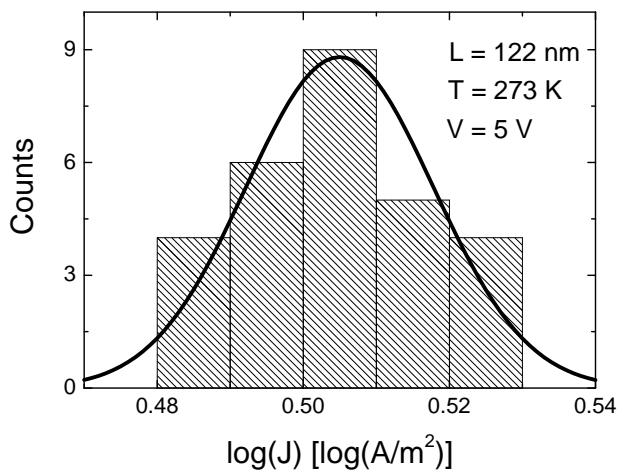


Figure 2.9: Histogram of the measured current density at 273 K and at 5 V for a hole-only PF-TAA based device with a layer thickness of 122 nm, as discussed in section 2.4.1. The solid line shows the best-fit normal distribution.

Figure 2.10 shows the voltage dependence of the standard deviation of $\log_{10}(J)$, measured at two temperatures. At room temperature (295 K), no active temperature control is used. This leads to a small experimental uncertainty, of about 0.5 to 2% for voltages above 2 V. This percentage is calculated using $(10^\alpha - 1) \times 100\%$, where α is the standard deviation in $\log_{10}(J)$, as obtained from Figure 2.10. At 273 K an active temperature control is used. This leads in our setup to a higher uncertainty, up to 4% above 2 V. The peak in the uncertainty in the lower voltage regime corresponds to the steep onset of the current-density, which occurs at a temperature-dependent voltage which is significantly smaller than the built-in voltage due to charge-carrier diffusion.²⁷ The parameter extraction results presented were based only on $J(V)$ -points well above V_{bi} . In particular, for the temperature and layer thickness dependent set of $J(V)$ curves considered in Section 2.4.1, the experimental uncertainty was determined for every experiment.

This gives a balanced weight to every measured current-density.

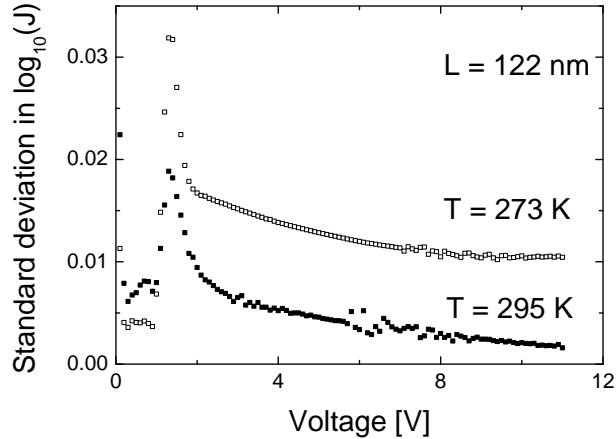


Figure 2.10: Voltage dependence of the standard deviation of the measured current density for two temperatures (295 K and 273 K) in a PF-TAA based hole-only device with a layer thickness of 122 nm, as discussed in Section 2.4.1.

The uncertainty in the obtained parameter values is in practice also influenced by a non-random contribution due to errors in the layer thickness (ΔL) and in the (average) measurement temperature (ΔT). Both uncertainties lead to a (non-random) shift of the $J(V)$ curves. The resulting uncertainty in the parameter values can be obtained by making use of a Taylor expansion of the function F_i (defined in Eq. 2.1) around the optimal set of parameters, i.e. by writing

$$F_i(\Delta L, \Delta T) = F_i(0, 0) + \frac{\partial F_i}{\partial L} \Delta L + \frac{\partial F_i}{\partial T} \Delta T, \quad (2.9)$$

and by subsequently minimizing the corresponding χ^2 -value

$$\chi^2(\Delta L, \Delta T) = \min_{\Delta P_j} \left\{ \frac{1}{n} \sum_{i=1}^n [F_i(\Delta L, \Delta T) + \frac{\partial F_i}{\partial P_j} \Delta P_j]^2 \right\} \quad (2.10)$$

in order to obtain the optimal change ΔP of each of the parameters (j). This optimal change can be used as a measure for the uncertainty in every parameter due to the mentioned non-random uncertainties. For the case studied in Section 2.4.1, $\Delta L = \pm 2$ nm and $\Delta T = \pm 2$ K was taken to obtain the confidence intervals given in Table 2.3.

Bibliography

1. C. Tanase, E. J. Meijer, P. W. M. Blom, and D. M. de Leeuw, *Phys. Rev. Lett.* **91**, 216601 (2003).
2. C. Tanase, P. W. M. Blom, D. M. de Leeuw, and E. J. Meijer, *Phys. Stat. Sol. (a)* **201**, 1236 (2004).
3. J. Staudigel, M. Stossel, F. Steuber, and J. Simmerer, *J. Appl. Phys.* **86**, 3895 (1999).
4. P. W. M. Blom and M. C. J. M. Vissenberg, *Mat. Sc. and Eng.* **27**, 53-94 (2000).
5. P. W. M. Blom, C. Tanase, D. M. de Leeuw, and R. Coehoorn, *Appl. Phys. Lett.* **86**, 092105 (2005).
6. W. F. Pasveer, J. Cottaar, C. Tanase, R. Coehoorn, P. A. Bobbert, and P. W. M. Blom, *Phys. Rev. Lett.* **94**, 206601 (2005).
7. R. Coehoorn, W. F. Pasveer, P. A. Bobbert, and M. A. J. Michels, *Phys. Rev. B.* **72**, 155206 (2005).
8. M. Bouhassoune, S. L. M. van Mensfoort, P. A. Bobbert, and R. Coehoorn, *Org. Electron.* **10**, 437 (2009).
9. J. J. Kwiatkowski, J. Nelson, H. Li, J. L. Bredas, W. Wenzel, and C. Lennartz, *Phys. Chem. Chem. Phys.* **10**, 1852 (2008).
10. V. Coropceanu, J. Cornil, D. A. da Silva Filho, Y. Olivier, R. Silbey, and J. L. Bredas, *Chem. Rev.* **107**, 926 (2007).
11. V. Rühle, A. Lukyanov, F. May, M. Schrader, Th. Vehoff, J. Kirkpatrick, B. Baumeier, and D. Andrienko, *J. Chem. Theory Comput.* **10**, 3335 (2011).
12. S. L. M. van Mensfoort, S. I. E. Vulto, R. A. J. Janssen, and R. Coehoorn, *Phys. Rev. B.* **78**, 085208 (2008).
13. J. C. Blakesley, H. S. Clubb, and N. C. Greenham, *Phys. Rev. B* **81**, 045210 (2010).
14. J. C. Blakesley and N. C. Greenham, *J. Appl. Phys.* **106**, 034507 (2009).
15. S. L. M. van Mensfoort, J. Billen, S. I. E. Vulto, R. A. J. Janssen, and R. Coehoorn, *Phys. Rev. B* **80**, 033202 (2009).
16. R. J. de Vries, S. L. M. van Mensfoort, V. Shabro, S. I. E. Vulto, R. A. J. Janssen, and R. Coehoorn, *Appl. Phys. Lett.* **94**, 163307 (2008).
17. S. L. M. van Mensfoort, R. J. de Vries, V. Shabro, H. P. Loebel, R. A. J. Janssen, and R. Coehoorn, *Org. Electron.* **11**, 1408-1413 (2010).

18. S. L. M. van Mensfoort, V. Shabro, R. J. de Vries, R. A. J. Janssen, and R. Coehoorn *J. of Appl. Phys.* **107**, 113710 (2010).
19. I. Bauer, H. G. Bock, S. Korkel, and J. P. Schlodel, *Journ. of Comp. and Appl. Math.* **120**, 1-25 (2000).
20. H. G. Bock, E. Kostina, and J. P. Schlodel, *GAMM-Mitt.* **30**, No 2, 376-408 (2007).
21. R. C. Aster, B. Borchers, and C. H. Thurber, *Parameter Estimation and Inverse Problems* (Elsevier Academic Press, Oxford, 2005).
22. M. M. Mandoc, B. de Boer, and P. W. M. Blom, *Phys. Rev. B* **73**, 155205 (2006).
23. M. M. Mandoc, B. de Boer, G. Paasch, and P. W. M. Blom, *Phys. Rev. B.* **75**, 193202 (2007).
24. J. Cottaar, L. J. A. Koster, R. Coehoorn, and P. A. Bobbert, *Phys. Rev. Lett.* **107**, 136601 (2011).
25. P. R. Emtage and J. J. O'Dwyer, *Phys. Rev. Lett.* **16**, 356 (1966).
26. P. Mark and W. Helfrich, *J. Appl. Phys.* **33**, 205 (1962).
27. R. J. de Vries, S. L. M. van Mensfoort, R. A. J. Janssen, and R. Coehoorn *Phys. Rev. B* **81**, 125203 (2010).

3

Relation between the built-in voltage in OLEDs and the zero-field voltage as measured by electroabsorption

For developing understanding of the current density onset voltage and injection barriers in organic light-emitting diodes (OLEDs), a precise determination of the built-in voltage, V_{bi} , is of crucial importance. Commonly, V_{bi} is assumed to be equal to the voltage $V_{0,EA}$ at which in an electroabsorption (EA) experiment the reflection of light at the OLED is found to become insensitive to a small voltage modulation. However, this assumption is shown to lead to significant errors for devices with well-injecting contacts. From an analysis of EA experiments for hole-only devices containing a polyfluorene-based copolymer, it is shown that $V_{0,EA}$ may be interpreted as an effective current density onset voltage, agreeing with the commonly accepted picture, but that for these devices V_{bi} is ~ 0.5 V larger than $V_{0,EA}$. This is found to be consistent with predictions of $V_{0,EA}$ from model calculations of the electric field and light-absorption profiles in the semiconducting layer.

3.1 Introduction

Since the demonstration of bilayer OLEDs by Tang and VanSlyke,¹ the power efficiency of OLEDs has increased impressively.²⁻⁴ Advances in the understanding of the relevant processes, such as charge carrier injection, transport and recombination, are expected to enable further progress. Many of these processes are strongly affected by the electric field, F . In the absence of a space charge, the electric field would be uniform and given by $(V - V_{\text{bi}})/L$, with V the applied voltage, V_{bi} the built-in voltage and L the semiconductor layer thickness. The built-in voltage may be expressed as $V_{\text{bi}} = (W_{\text{a}} - W_{\text{c}})/e$, with W_{a} and W_{c} effective work functions of the anode and cathode, respectively, and with e the elementary charge. V_{bi} is an important parameter in device models, as it is related to the hole and electron injection barriers, Φ_{h} and Φ_{e} , at the anode and cathode interfaces, respectively, via the relationship $\Phi_{\text{h}} + \Phi_{\text{e}} = E_{\text{g}} - V_{\text{bi}}/e$, with E_{g} the semiconducting gap energy.

The built-in voltage may be determined using for example capacitance-voltage measurements,⁵ photovoltaic measurements,⁶ steady-state current-voltage measurements,⁷ and electro-absorption (EA) measurements.⁸⁻¹⁹ The latter method, which probes the electric field in OLEDs, is the subject of this paper. EA experiments involve measurements of the modulation, ΔR , of the reflection coefficient for monochromatic light, R , resulting from the application of a small ac voltage superimposed on a dc bias voltage. This non-invasive technique uses the fact that the optical absorption coefficient α of an organic layer changes with the square of the electric field. The change in α is caused by a Stark-like shift of the allowed optical transitions.²⁰ In most analyses, it is assumed that the electric field is uniform across the organic semiconducting layer(s), at least at small voltages below V_{bi} . The field dependence of the absorption leads then to a field-dependent relative change of the reflection coefficient given by⁸

$$\frac{\Delta R}{R}(h\nu) \propto \text{Im} \chi^{(3)}(h\nu) F^2. \quad (3.1)$$

Here, $\text{Im} \chi^{(3)}$ is the imaginary part of the third order susceptibility at the photon energy $h\nu$ employed. The photon energy dependence of the effect has been used to resolve the electric field in distinct semiconducting layers within multilayer OLEDs.²¹⁻²⁴ Furthermore, the photon energy and modulation frequency dependence has been used to distinguish the Stark-like effect mentioned above from a contribution due to charge-induced absorption.^{14-17,23-25} The voltage $V_{0,\text{EA}}$ at which the relative change in reflection in a single-layer device vanishes is commonly viewed as a direct measure of V_{bi} .

In this paper, we demonstrate that for OLEDs with well-injecting contacts the assumption that at $V_{0,\text{EA}}$ the field across the semiconducting layer is essentially uniform is not correct, and that this can result in a significant difference between $V_{0,\text{EA}}$ and V_{bi} . The effect is caused by the presence of a substantial space charge density close to the injecting electrodes, even at voltages well below V_{bi} . This affects the electric field throughout the entire device. We also argue that, in view of the non-uniformity of the electric field, it will in general be important to

include the variation of the optical absorption across the semiconducting layer in the analysis. The absorption in the active layer is far from homogeneous, as is shown from thin-film optical microcavity calculations. The analysis is carried out for sandwich-type hole-only devices containing a blue-emitting polyfluorene-based co-polymer with varying layer thicknesses. For the devices studied, the charge-carrier density and electric field dependence of the mobility are well-known from an analysis of steady-state current density versus voltage ($J(V)$) measurements.⁷ This makes it possible to accurately determine V_{bi} from such measurements, using a drift-diffusion device model.

Section 3.2 contains a description of the material and device structures, and of the experimental methods. In section 3.3, the experimental results are presented and analyzed. A model is developed which describes the layer thickness dependence of $V_{0,EA}$, the difference with V_{bi} and the shape of the EA signal over a relatively large voltage range. Section 3.4 contains a summary and conclusions.

3.2 Experimental method

The devices studied contain a polyfluorene (PF) based polymer (from the LumationTM Blue Series, supplied by Sumation Co., Ltd.) with randomly copolymerized triarylamine (TAA) monomer units (7.5 mol %) as the semiconducting layer (PF-TAA), with 67 nm, 98 nm and 122 nm layer thicknesses. The PF-TAA layer thicknesses were determined from step-height measurements using a VeecoTM Dektak stylus profilometer. The hole transport takes place via the TAA units.²⁶ The full layer structure and the structure of the fluorene and TAA units are shown in Figure 1. The anode consists of a 100 nm thick poly(3,4-ethylenedioxythiophene):poly(styrenesulfonic acid) (PEDOT:PSS) layer, spin-coated on precleaned glass substrates covered with 100 nm indium tin oxide (ITO). The cathode consists of a palladium layer, evaporated in a high-vacuum chamber to form 100 nm thick top electrodes. The use of patterned bottom and top electrodes results in glass | ITO | PEDOT:PSS | PF-TAA | Pd structures with areas of $3 \times 3 \text{ mm}^2$.

Within the EA measurements, a laser beam is focused on the organic diode which is driven by a Keithley 2601 function generator. The applied voltage consists of a dc voltage component, V_{dc} , and an ac component with a frequency $f = 1.18 \text{ kHz}$ and amplitude V_{ac} , so that $V(t) = V_{dc} + V_{ac} \cos 2\pi ft$. The resulting modulation of the reflection is extracted using a Stanford Research Systems SR830 DSP lock-in amplifier, synchronized by the function generator. The use of a Nirvana auto-balanced dual-beam photoreceiver, which takes out the dc component of the reflected signal proportional to the incident light intensity, was found to improve the signal-to-noise ratio. The amplitude of the first-order term $R_{ac} \cos 2\pi ft$ in the time-dependent detector response, which is proportional to $-dR/dV$ for sufficiently small values of V_{ac} , is usually called “the electro-absorption signal”. In a typical measurement, the EA signal is measured as a function of V_{dc} , while keeping V_{ac} at a small constant value $\sim 0.8 \text{ V}$. Consistent with the results of Bodrozic *et al.*,¹⁸ no change except for an enhancement of the signal strength was found by increasing V_{ac} up to this value. Also, a variation of the modulation frequency

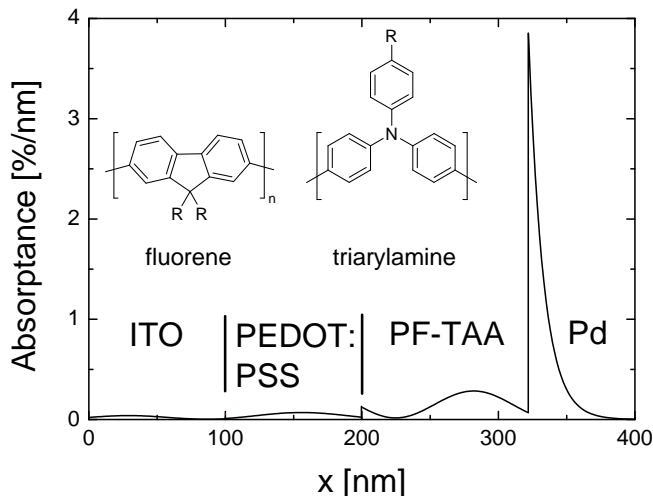


Figure 3.1: Layer structure of a 122 nm device as studied in this chapter, calculated absorbance as a function of the distance x from the glass/ITO interface (see section 3.3), and structures of the fluorene and triarylamine monomer units forming the PF-TAA copolymer.

in the range 500-3000 Hz was found to have no effect on the EA signal. This implies that a possible contribution due to charge-induced absorption^{14-17,23-25} can be neglected. Furthermore, no hysteresis of the EA signal as a function of the voltage was observed.

The third order susceptibility is proportional to a linear combination of the first and second order derivative of the absorption coefficient with respect to the photon energy.²⁷ The absorption coefficient of PF-TAA varies strongly in the range from 400 to 450 nm. We studied all three devices using laser diodes with emission wavelengths of 408 nm and 440 nm. Very similar voltage dependences of the EA signal were obtained, except for the thickest device. In that case, the intensity of the reflected light at 408 nm was rather low due to the relatively high total absorption for that wavelength in the 122 nm organic layer, leading to a relatively poor signal-to-noise ratio. The lower absorbance at 440 nm led to a significantly higher signal-to-noise ratio for measurements at that wavelength. All results reported in this chapter have therefore been obtained using the 440 nm laser diode. A systematic variation of the laser fluence, revealed no effect on the measured value of $V_{0,EA}$ and on the voltage dependence of the EA signal.

3.3 Experimental results and analysis

Before carrying out the EA experiments, temperature dependent steady-state $J(V)$ curves were measured to determine the value of V_{bi} for all three devices studied. The analysis employs a description of the mobility as given by the Gaussian Disorder Model (GDM), using the carrier density and field dependence of the mobility as described in Ref. 28 and with the parameter values describing the mobility as obtained by van Mensfoort *et. al.*⁷ The inset in Figure 3.2 shows the measured and modeled $J(V)$ curves for each thickness, at $T = 295$ K. As compared to the earlier study of the same devices in Ref. 7, no change of these curves apart from a slight (~ 0.2 eV) decrease of V_{bi} was found.

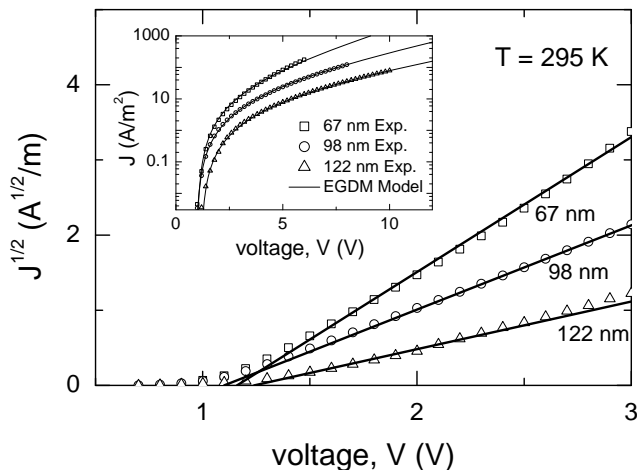


Figure 3.2: Square-root of the measured current density versus voltage for three PF-TAA layer thicknesses (open symbols) at room temperature, and linear fits through these data taking $J = 0$ at $V = V_{0,\text{EA,exp}}$ (solid lines). The inset shows the corresponding measured data (open symbols) and the modeled current density versus voltage curves (solid curves).

The results are included in Table 3.1. From the vacuum work functions of PEDOT:PSS and palladium, which are both close to 5 eV, a built-in voltage close to 0 V would be expected. However, the actual values are much larger, in the range 1.6 – 1.9 V. As no significant injection barrier at the anode was found, which is expected on the basis of the vacuum work functions of PEDOT:PSS and the very similar ionization potential of the hole-transporting TAA units, the high value of V_{bi} indicates that important metal-organic interactions occur at the cathode interface.⁷ The small variation of V_{bi} with L suggests a sensitivity to the (nominally

identical) deposition conditions, and the slightly lower value of V_{bi} as compared to the previous result suggests a small time-dependent change of the dipole layer at the PF-TAA/Pd interface.

Table 3.1: Layer thickness dependence of the built-in voltage (V_{bi}), the zero-crossing voltage as determined from EA experiments ($V_{0,\text{EA,exp}}$) and as calculated using the model discussed in section III ($V_{0,\text{EA,mod}}$), and the peak voltage as obtained from low-frequency differential capacitance measurements ($V_{\text{p,C}}$). $V_{0,\text{EA,mod}}$ was calculated by subtracting from V_{bi} the value of $V_{\text{bi}} - V_{0,\text{EA,mod}}$ as obtained from modeling.

L (nm)	V_{bi} (V)	$V_{0,\text{EA,exp}}$ (V)	$V_{0,\text{EA,mod}}$ $V_{\text{bi}} - V_{0,\text{EA,mod}}$ (V)	$V_{\text{p,C}}$ (V)
67	1.66 ± 0.05	1.16 ± 0.07	1.18 ± 0.10 0.48 ± 0.05	1.10 ± 0.04
98	1.63 ± 0.05	1.10 ± 0.10	1.08 ± 0.10 0.55 ± 0.05	1.00 ± 0.03
122	1.87 ± 0.05	1.24 ± 0.15	1.29 ± 0.10 0.58 ± 0.05	1.2 ± 0.1

Figure 3.3 shows the measured EA signal (squares) for the three PF-TAA layer thicknesses. Two observations can be made immediately. First, the measured zero crossing values $V_{0,\text{EA}}$ (included in Table 3.1) are significantly smaller than the built-in voltages as determined above (red squares). A qualitatively similar result was recently found by Gather *et al.*,²⁴ who studied devices containing a green-emitting phosphorescent polymer/dye blend and measured an EA zero crossing at ~ 2.5 V whereas a value of ~ 3.0 V was expected on the basis of the work function difference of the electrodes. In that work, no further analysis was given. Secondly, the shape of the voltage dependence of the signal changes with the thickness: for the 67 nm device the curve is slightly concave whereas it is slightly convex for the 122 nm device. A non-linear shape of the EA signal was also found in other studies,^{19,24} and was argued to be due to screening of the internal field resulting from space charge injected in the device or to a voltage dependent contribution due to charge-induced absorption. However, no quantitative analysis was given. The observed difference between $V_{0,\text{EA}}$ and V_{bi} and the voltage dependence of the EA signal are the two issues we will clarify by modeling the measured EA signals. We note that the shape of the signal versus voltage does not yield any indication for a possible effect of electron trapping at the anode interface, in contrast to the results obtained by Brewer *et al.*^{14,15,17} for poly(9,9-dioctyl)fluorene (PFO) based devices, i.e. for a polymer without TAA hole transporting units.

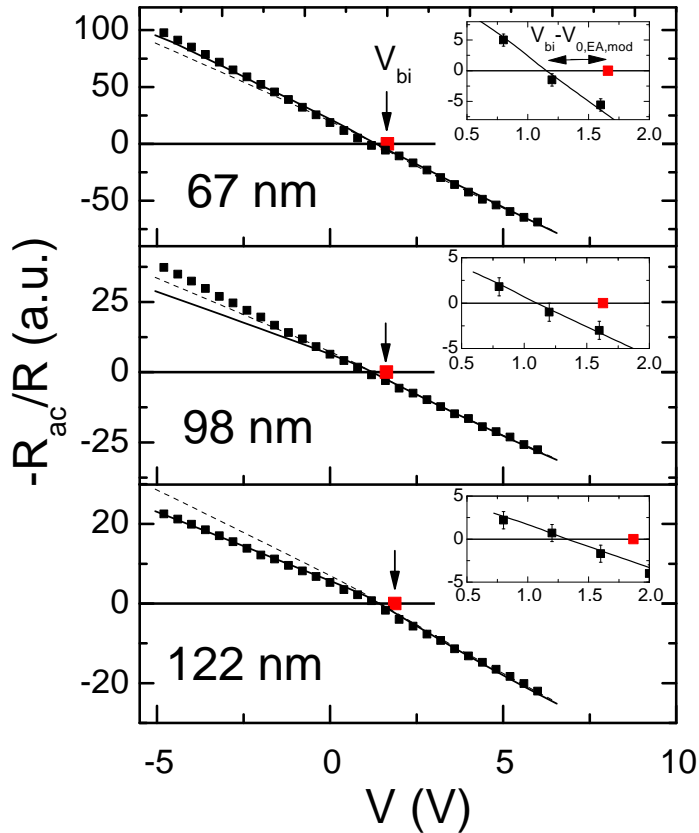


Figure 3.3: Electro-absorption signal as a function of the bias voltage for three devices with different PF-TAA layer thicknesses. Black small squares: experimental data. The arrows and the larger red squares indicate the values of the built-in voltage as determined from an analysis of steady state current-voltage curves. Solid and dashed lines: model results including and excluding the position dependence of the absorptance rate, respectively (see text). The insets provide a closer view around $V_{0,EA}$.

The observation of an EA signal which varies linearly with the voltage is commonly viewed as a justification of the assumption that the device is space-charge free. However, the fact that the detailed shape of the curves depends on the layer thickness indicates that this point of view is in general not correct, and that even in the case of near-linearity this can be the result of an interplay between various balancing effects. In the devices studied, there is already at zero applied voltage a considerable space charge present in the PF-TAA layer near the anode interface, which forms a well-injecting contact for holes due to the low or even negligible injection barrier at that interface.⁷ In order to investigate the effect of this space charge on the EA signal, as a first step the position-dependent electric field $F(x)$ is calculated as a function of the voltage, using the drift-diffusion model given in Ref.²⁹. Figure 3.4(a) shows results for a 122 nm thick PF-TAA layer, for three values of the voltage. The figure clearly reveals a strong position dependence of the field in at least a part of the device.

In the case of a non-uniform electric field, the EA signal is affected by the position dependence of the absorptance rate $A(x)$, defined as the fraction of the incident radiant energy absorbed per nanometer. Under the conditions employed, the relative change of the light absorption in the device upon modulating the bias voltage is very small. The voltage dependence of the EA signal may then be expressed as

$$\frac{R_{ac}}{R}(h\nu, V) \propto -\text{Im} \chi^{(3)}(h\nu) \int_0^L A(x) \left. \frac{dF(x, V')^2}{dV'} \right|_V dx. \quad (3.2)$$

Figure 3.4(b) shows for the 122 nm device the calculated position dependence of the function dF^2/dV . Figure 3.1 shows the absorptance rate for a 440 nm incident wavelength, as used in the EA experiments, for the case of a constant absorption coefficient corresponding to $F(x) = 0$. The calculation has been carried out using the thin-film optical software package MACLEOD, with the complex refractive indices of the layers as determined by ellipsometry. The light absorption in the PF-TAA layer is quite non-uniform. As a result, changes in the absorption coefficient at a position of about 40 nm from the Pd electrode, for example, contribute more strongly to the EA signal than changes close to the LEP-Pd interface. Figure 3.4(c) gives the position dependence of the absorptance-weighted contributions to the EA signal.

Application of Eq. 3.2 leads to the full model curves shown in Figure 3.3. The model results obtained by only taking the position dependence of the electric field into account (i.e. assuming $A(x) = 1$), are shown by dashed lines. In all cases, the proportionality factor is taken such that an optimal fit is obtained for positive voltages. The insets show the same results, focusing at the region around $V_{0,EA}$. The values of $V_{0,EA}$ as obtained from the model are included in Table 3.1. Excellent agreement is obtained with the experimental zero-crossing voltages. Furthermore, it is seen from the figure that both model curves yield essentially the same value of $V_{0,EA}$, but that the full shape of the EA curves is affected by the position dependence of the absorptance. Including the absorptance in the model improves the description of the voltage dependences of the EA signal for the 67 and 122 nm devices. From the experiment, the EA curves are slightly

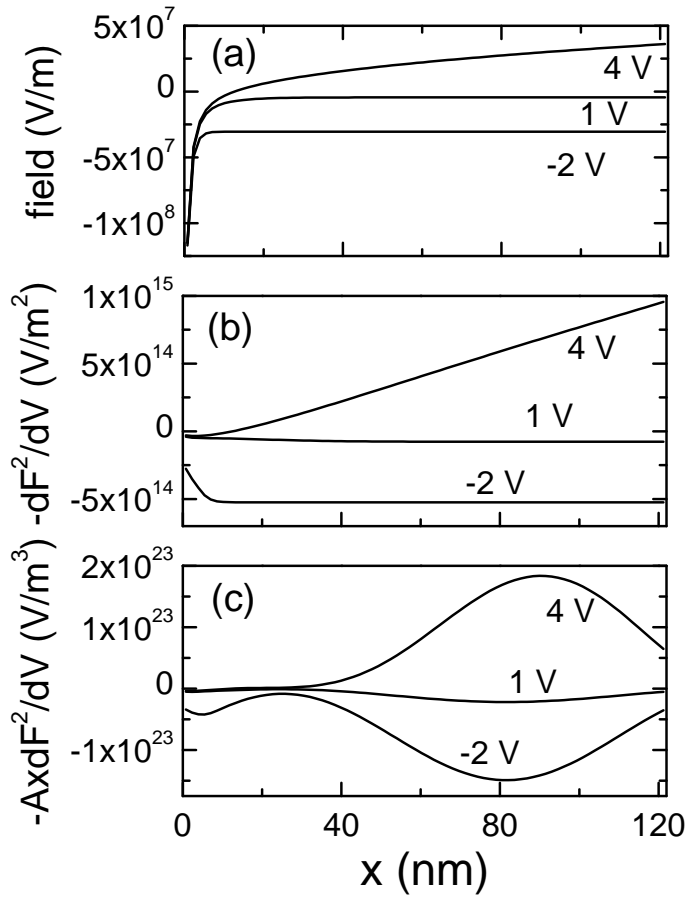


Figure 3.4: Calculated variation of the electric field F (a), the function $-dF^2/dV$ (b) and the function $-A \times dF^2/dV$ (c) throughout a 122 nm PF-TAA layer in the devices studied for several applied voltages.

convex and concave, respectively. On the other hand, including the absorptance leads for the 98 nm device to slightly worse agreement with experiment. We find that for this layer thickness a shift of the absorption profile of only 12 nm towards the middle of the devices would give rise to a (more concave) shape of the EA curve which agrees excellently with the experimental curve. The analysis of the full shape of the curves (but in this case not the determination of $V_{0,EA}$) is thus very sensitive to the exact form of the absorptance profile. The occurrence of a small shift of the absorption profile may in practice be induced by a slightly lower reflection at the polymer-Pd interface due to for example interface roughness.

The zero-crossing voltage as determined from EA can thus be considerably smaller than the built-in voltage. The effect is a result of the presence of space charge in the organic semiconductor. Although the space charge density is largest near the anode, its presence throughout the entire device is non-negligible. Therefore, the difference between V_{bi} and $V_{0,EA}$ is layer thickness dependent. The experimentally observed difference increases from 0.50 V for the 67 nm device to 0.63 V for the 122 nm device, consistent with the model predictions. Although it is thus incorrect to associate $V_{0,EA}$ to V_{bi} , we find that it is still possible to view $V_{0,EA}$ as an effective onset value of the space-charge-limited current. This may be seen from Figure 3.2, which shows that in the voltage range in between $V_{0,EA}$ and V_{bi} good linear fits can be made to the square-root of the current density, taking the voltage at which the curves extrapolate to zero equal to $V_{0,EA}$.

It has previously been established that an alternative measure for the effective onset voltage is given by the voltage $V_{p,C}$ at which at low-frequencies a distinct peak in the differential capacitance is observed.⁵ The values of $V_{p,C}$, as obtained from differential capacitance measurements at frequencies from 100 up to 5000 Hz, are included in Table 3.1. They are indeed close to the values of $V_{0,EA}$. The finding that $V_{p,C}$ is slightly larger for the 122 nm device than for the two other devices is consistent with the finding of a slightly larger value of V_{bi} for that device.

It would be of interest to extend in future studies the EA experiments to lower temperatures. The effect of charge carrier diffusion on $V_{0,EA}$ is expected to decrease with decreasing temperature, as it is due to space charge in the device. A similar effect has already been observed by Kemerink *et al.*³⁰ for the temperature dependence of the onset voltage in poly(phenylene vinylene) (PPV) based devices. To our point of view, the built-in voltage is then given by the value of the onset voltage, extrapolated to zero temperature.

3.4 Conclusions

We have studied hole-only devices based on a PF-TAA co-polymer with a very small injection barrier at the anode interface, and have shown that the voltage at which the EA signal vanishes is significantly smaller than the built-in voltage, determined from the analysis of the steady-state current density curves. The difference depends on the device thickness, and can be understood as a result of charge carrier diffusion, which leads to a strong variation in the electric field throughout the LEP layer. It has been shown that the zero-crossing voltage essentially coincides with the effective onset of the space-charge-limited current density, and with a distinct peak in the differential capacitance. A similar effect is known from studies of photovoltaic cells, where in the absence of extraction barriers the open-circuit voltage V_{oc} can be 0.5 eV smaller than V_{bi} .³¹ The shape of the voltage dependence of the measured EA signal, which is concave and convex for the device with a 67 and 122 nm LEP layer, respectively, can be understood well by properly taking the variation of the absorptance throughout the organic layer into account. The analysis of the detailed shape of the EA curves is found to be quite sensitive to the detailed shape of the absorptance profiles, which therefore in general should be taken into account when analyzing the results of EA measurements.

Bibliography

1. C. W. Tang, and S. A. VanSlyke, *Appl. Phys. Lett.* **51**, 913 (1987).
2. Y. Sun, N. C. Giebink, H. Kanno, B. Ma, M. E. Thompson, and S. R. Forrest, *Nature* (London) **440**, 908 (2006).
3. S.-J. Su, E. Gonmori, H. Sasabe, and J. Kido *Adv. Mater.* **20**, 4189 (2008).
4. S. Reineke, F. Lindner, G. Schwartz, N. Seidler, K. Walzer, B. Lüssem, and K. Leo, *Nature* **459**, 234 (2009).
5. S. L. M. van Mensfoort, and R. Coehoorn, *Phys. Rev. Lett.* **100**, 086802 (2008).
6. G. G. Malliaras, J. R. Salem, P. J. Brock, and J. C. Scott *J. Appl. Phys.* **84**, 1583 (1998).
7. S. L. M. van Mensfoort, S. I. E. Vulto, R. A. J. Janssen, and R. Coehoorn, *Phys. Rev. B* **78**, 085208 (2008).
8. I. H. Campbell, T. W. Hagler, D. L. Smith, and J. P. Ferraris, *Phys. Rev. Lett.* **76**, 1900 (1996).
9. C. M. Heller, I. H. Campbell, D. L. Smith, N. N. Barashkov, and J. P. Ferraris, *J. Appl. Phys.* **81**, 3227 (1997).
10. T. M. Brown, J. S. Kim, R. H. Friend, F. Cacialli, R. Daik, and W. J. Feast, *Appl. Phys. Lett.* **75**, 1679 (1999).
11. T. M. Brown, R. H. Friend, I. S. Millard, D. L. Lacey, T. Butler, J. H. Burroughes, and F. Cacialli, *J. Appl. Phys.* **93**, 6159 (2003).
12. S. J. Martin, G. L. B. Verschoor, M. A. Webster, and A. B. Walker, *Org. Elec.* **3**, 129 (2002).
13. P. A. Lane, P.J. Brewer, J. Huang, D.D.C. Bradley, and J. C. deMello, *Phys. Rev. B* **74**, 125320 (2006).
14. P. J. Brewer, P. A. Lane, J. deMello, D. D. C. Bradley, and J. C. deMello, *Adv. Func. Mat.* **14**, 562 (2004).
15. P. J. Brewer, P. A. Lane, J. Huang, A. J. deMello, D. D. C. Bradley, and J. C. deMello, *Phys. Rev. B* **71**, 205209 (2005).
16. P. J. Brewer, A. J. deMello, J. C. deMello, P. A. Lane, D. D. C. Bradley, R. Fletcher, and J. O'Brien, *J. Appl. Phys.* **99**, 114502 (2006).
17. P. J. Brewer, J. Huang, P. A. Lane, A. J. deMello, D. D. C. Bradley, and J. C. deMello, *Phys. Rev. B* **74**, 115202 (2006).
18. V. Bodrozic, M. Roberts, N. Philips, J. H. Burroughes, S. Mian, and F. Cacialli, *J. Appl. Phys.* **101**, 084507 (2007).

19. C. V. Hoven, J. Peet, A. Mikhailovsky, and T. Nguyen, *Appl. Phys. Lett.* **94**, 033301 (2009).
20. D. E. Aspnes, and J. E. Rowe, *Phys. Rev. B* **5**, 4022 (1972).
21. I. H. Campbell, M. D. Joswick, and I. D. Parker, *Appl. Phys. Lett.* **67**, 3171 (1995).
22. F. Rohlfing, T. Yamada, and T. Tsutsui, *J. Appl. Phys.* **86**, 4978 (1999).
23. K. Book, H. Bässler, A. Elschner, and S. Kirchmeyer, *Org. Electron.* **4**, 227 (2003).
24. M. C. Gather, R. Jin, J. de Mello, and D. D. C. Bradley, *Appl. Phys. B* **95**, 113-124 (2009).
25. I. H. Campbell, D. L. Smith, C. J. Neef, and J. P. Ferraris, *Appl. Phys. Lett.* **78**, 270 (2001).
26. R. J. de Vries, S. L. M. van Mensfoort, V. Shabro, S. I. E. Vulto, R. A. J. Janssen, and R. Coehoorn *Appl. Phys. Lett.* **94**, 1 (2009).
27. S. J. Martin, D. D. C. Bradley, P. A. Lane, H. Mellor, and P. L. Burn, *Phys. Rev. B* **59** (1999).
28. W. F. Pasveer, J. Cottaar, C. Tanase, R. Coehoorn, P. A. Bobbert, P. W. M. Blom, D. M. de Leeuw, and M. A. J. Michels, *Phys. Rev. Lett.* **94**, 206601 (2005).
29. R. Coehoorn, and S. L. M. van Mensfoort, *Phys. Rev. B* **80**, 085302 (2009).
30. M. Kemerink, J. M. Kramer, H. H. P. Gommans, and R. A. J. Janssen, *Appl. Phys. Lett.* **88**, 192108 (2006).
31. V. D. Mihailetschi, P. W. M. Blom, J. C. Hummelen, and M. T. Rispens, *J. Appl. Phys.* **94**, 6849 (2003).

Analysis of hole transport in a polyfluorene based copolymer - evidence for the absence of correlated disorder

The presence of spatial correlation between the disordered transport site energies in semiconducting polymers used in organic electronic devices is known to affect the mobility. However, it is not established whether such a correlation is present in relevant polymers. We study hole transport in a polyfluorene-based copolymer and provide evidence for the absence of spatially correlated disorder in this material, based on an analysis of the current-voltage characteristics of sandwich-type devices. Distinguishing correlated from uncorrelated disorder, which we achieve on the basis of the hopping site density, is shown to be highly relevant for the development of quantitative device models.

4.1 Introduction

It is widely agreed that the charge carrier mobility in the disordered organic semiconductors used in organic light-emitting diodes (OLEDs) is determined by hopping between localized states. However, the development of transport models with predictive value is hampered by a lack of consensus about the type of energetic disorder: completely random or with correlation between the energies on neighbor sites. Within his pioneering Monte Carlo studies of the effects of disorder on the mobility, Bäessler¹ assumed an uncorrelated Gaussian distribution of hopping site energies. Pasveer *et al.*² showed that an extension of this model to include a carrier density (n) dependence of the mobility,^{3,4} leading to the "extended Gaussian disorder model" (EGDM), can well describe the temperature (T) dependent current-voltage characteristics $J(V,T)$ of hole transport in sandwich-type devices based on polyphenylene-vinylene (PPV) polymers. A similar conclusion was recently obtained by van Mensfoort *et al.*,⁵ who analyzed the $J(V,T)$ characteristics of hole-only polyfluorene-based copolymer devices with various layer thicknesses L . The successful use of the EGDM mobility functions,⁶ as obtained from a master-equation (ME) approach within which the nonequilibrium ("hot") carrier energy distribution is calculated assuming a *uniform* carrier density and field, indicates that for the systems studied energy relaxation after injection of carriers in actual devices with *nonuniform* densities and fields takes place on a time scale that is much shorter than the transit time. Recently, a three-dimensional ME modeling study of the $J(V)$ curves of complete devices has provided support for this point of view.⁷

The mobility (μ) in a system with spatially correlated energetic disorder was first analyzed by Gartstein and Conwell,⁸ who showed that the effect can explain why time-of-flight measurements^{9,10} often yield a Poole-Frenkel (PF) type electric field (E) dependence of the mobility, where $\ln(\mu)$ varies linearly with \sqrt{E} in a rather wide E -range. Correlation can arise as a result of randomly oriented dipoles^{11,12} a variable morphology,¹³ or (for polymers) a variable strain of the backbone.¹⁴ Dipolar disorder leads to a Gaussian density of states (DOS), with a pair correlation function of the site energies that decreases by a factor of ~ 2 within ~ 1.5 average intersite distances and which decreases at large distances (r) as $1/r$.⁸ Recently, it was found from a ME approach that the mobility is then not only field and temperature dependent,¹¹ but also carrier density dependent (as for the EGDM), leading to the so-called "extended correlated disorder model" (ECDM).¹⁵

The question now arises whether a successful analysis of the $J(V,T,L)$ characteristics of a certain material using the EGDM or the ECDM would already convincingly prove that the disorder is completely random or correlated, respectively. This question was already addressed in Ref. 15 by reanalyzing the PPV-data given in Ref. 2 for a single device. It was concluded that also the ECDM can provide a good description, provided that a much smaller intersite distance is assumed within the ECDM (~ 0.3 nm) than within the EGDM (~ 1.6 nm). Unfortunately, the relatively large conjugation length in PPV-based polymers (typically 10 monomer units) implies that the basic starting point of both models

(hopping between pointlike sites) is not well met. Therefore, it was not possible to derive from the observed intersite distances a conclusion about the presence of correlation.

4.2 Experimental results

In this chapter, we address this question by reanalyzing the $J(V,T,L)$ characteristics of the hole transport in sandwichtype polyfluorene-based copolymer devices as studied in Ref. 5, now using the ECDM. The polymer (from the LumationTM Blue Series, supplied by Sumation Co., Ltd.) consists of randomly copolymerized fluorene and triarylamine monomer units (7.5 mol %).

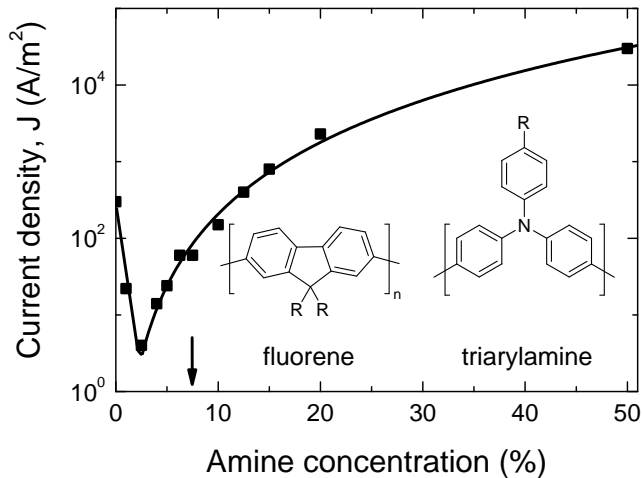


Figure 4.1: Current density at 6 V, as a function of the amine concentration (the curve is a guide to the eyes), measured (symbols) in 80 nm hole-only devices. Inset: structure of the fluorene and amine monomer units used. The arrow indicates the amine concentration on which this study focuses.

From cyclic voltammetry (CV), the amine-related highest occupied molecular orbital (HOMO) energy is found to be at ~ 5.2 eV, well displaced from the HOMO energy of the polyfluorene-derived states (~ 5.8 eV) and very close to the Fermi level energy in the hole conducting poly(3,4-ethylenedioxythiophene):poly(styrenesulfonic acid) (PEDOT:PSS) anode layer (~ 5.1 eV).⁵ These energy levels are close to those found from CV for similar materials.^{16,17} Figure 4.1 shows the current density as measured at 6 V in 80 nm hole-only devices, for a series of copolymers in which the concentration of amines is varied. The device structure is

as discussed below but with a gold cathode. Whereas the amines act as traps for small concentrations, the effective mobility increases strongly when the concentration is above the percolation threshold for guest-guest hopping. The copolymer studied in this chapter is in the second regime. Figure 4.1 thus suggests that in the copolymer studied the hole transport takes place via states localized predominantly on the amines. The rather small effective wave function decay length (well below 1 nm), as estimated in Ref. 5 within the EGDM from the temperature dependence of the mobility is consistent with this picture. From quantum-chemical calculations evidence for a fair degree of localization of the holes on the amines in similar copolymers was obtained.¹⁶ This makes these polymers more suited for our purpose than the PPV-type polymers studied in Ref. 15. We note that Khan *et al.*¹⁷ already analyzed similar systems (but with a 50 mol % amine concentration), with a single layer thickness and using the standard CDM and GDM. They also considered the site density as a possible distinguishing factor. However, no final conclusion was obtained on the presence of correlated disorder. The availability of $J(V,T)$ -characteristics for various device thicknesses and of the recently developed ECDM enable us to present a comparison with Ref. 5 employing the EGDM.

The devices studied have the structure

$$| \text{Glass} | \text{ITO} | 100 \text{ nm PEDOT:PSS} | \text{LEP} | 100 \text{ nm Pd} | , \quad (4.1)$$

with an indium tin oxide (ITO)/PEDOT:PSS anode layer, a light-emitting polymer (LEP) layer, and a palladium cathode. The PEDOT:PSS and LEP layers are deposited by spin coating; Pd is deposited by evaporation. The built-in voltage V_{bi} is approximately 2 V and the electron injection barrier at the cathode is approximately 1 eV. No evidence of electron injection or light emission was obtained. Figure 4.2 shows the measured $J(V,T)$ -characteristics for devices with LEP layer thicknesses of 67 and 122 nm for the temperature range as available from Ref. 5 (symbols).

4.3 Modeling results

Using a least-squares method, a fit to the data is made. The results are shown in Figure 4.2 (curves). The model uses functions of the form $\mu_{\text{ECDM}}(n,E,T) = \mu_{0,\text{ECDM}}(T) \times f(n,E,T)$. Here $\mu_{0,\text{ECDM}}$ is the temperature dependent mobility in the $n=0$ and $E=0$ limit and $f(n,E,T)$ is a dimensionless function which depends on the width of the Gaussian DOS σ , and on the density of hopping sites N_t in a manner described in Ref. 15. From this procedure, we find that the most likely solutions (fit error less than 3% larger than the minimum) reside in a narrow zone in $\{\sigma[\text{eV}], N_t[\text{m}^{-3}]\}$ -space, ranging from $\{0.08; 2 \times 10^{27}\}$ to $\{0.11; 2 \times 10^{28}\}$. The optimal fit to the data was obtained using the set of in total five parameters given in Table 4.1.

Table 4.1: Overview of the ECDM and EGDM model parameters that optimally describe the experimental current-voltage curves shown in Figure 4.2. In both models an experimentally determined relative permittivity of 3.2 was used (see Ref. 5).

Parameter	ECDM (this chapter)	EGDM ⁵
σ [eV]	0.085 ± 0.005	0.13 ± 0.01
N_t [10^{27} m^{-3}]	5 ± 2	0.6 ± 0.1
V_{bi} [V]	1.9 ± 0.1	1.95 ± 0.05
μ_0^* [$10^{-8} \text{ m}^2/(\text{Vs})$]	0.05 ± 0.02	14 ± 6
C	0.33 ± 0.02	0.39 ± 0.01

Figure 4.2 shows that the ECDM is able to provide a good description of the experimental data. The internal consistency of the fitting procedure follows from the observation that for the optimal $\{\sigma, N_t\}$ -set (i) V_{bi} is independent of T for every thickness, and (ii) the values of $\mu_{0,\text{ECDM}}(T)$ are essentially thickness independent and well described by an exponential $1/T^2$ dependence consistent with the ECDM, as shown in Figure 4.3. The line through the data points is described by the expression included in Figure 4.3, with a slope parameter $C = 0.33 \pm 0.02$. This value is close to the ECDM value $C = 0.29$ given in Ref. 15, calculated for a specific value of the wave function decay length. The actual value of C is expected to depend slightly on that length, as discussed in Ref. 18 for the EGDM. In order to more sensitively probe the shape of the DOS, it would be of interest to extend the temperature range to smaller values. However, we note that the numerical ECDM study in Ref. 15 yields mobility functions for cases up to $\sigma/k_B T = 5$. Accurately analyzing data well below $T = 150 \text{ K}$ [$\sigma/k_B T \sim 6.5$] would therefore require an extension of the model. We find that the smallest overall fitting errors using both models are almost equal. However, we regard the very high value of N_t ($5 \times 10^{27} \text{ m}^{-3}$) found using the ECDM as evidence that the model is not appropriate, as it is ~ 25 times larger than the amine density ($\sim 2 \times 10^{26} \text{ m}^{-3}$ for the concentration used). Much better agreement was found using the EGDM, which yields $N_t \approx 6.0 \times 10^{26} \text{ m}^{-3}$.

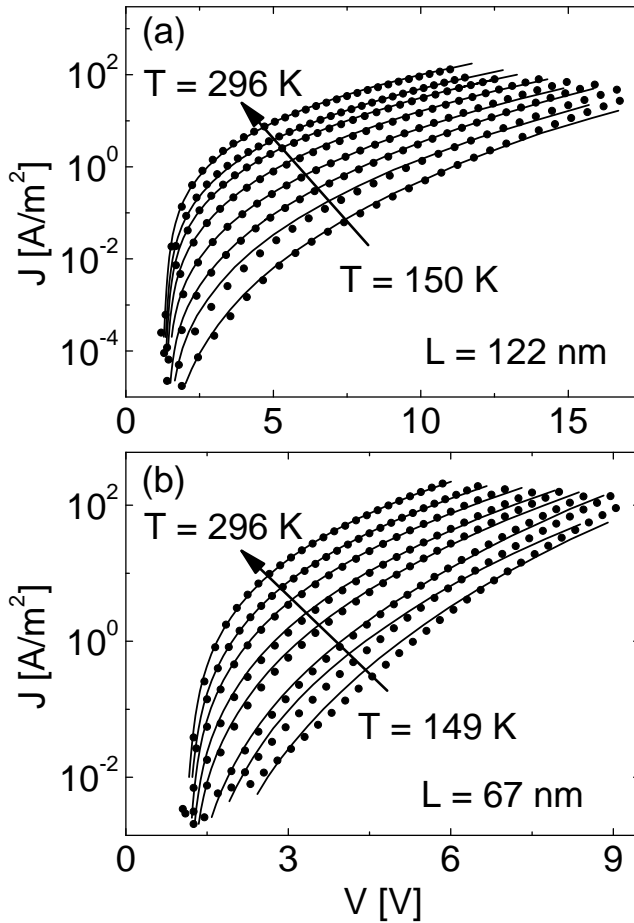


Figure 4.2: Experimental current-voltage characteristics (symbols) at various temperatures and at a layer thickness of (a) 122 nm and (b) 67 nm, and best fits using the ECDM (curves) with the parameters given in Table 4.1.

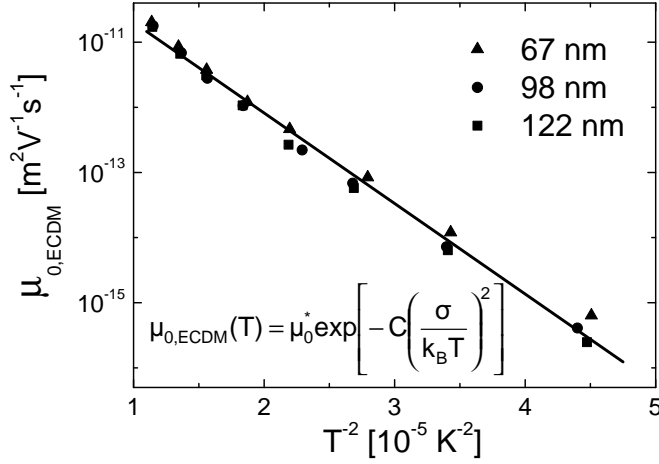


Figure 4.3: Parameter $\mu_{0,\text{ECDM}}$ as found from a fit to curves obtained at various temperatures and layer thicknesses (symbols) and a best fit using the expression shown (line).

The two sets of model parameters given in Table 4.1 lead to distinctly different predictions concerning the mobilities in devices in which much higher carrier densities occur, e.g., in OLEDs with internal interfaces at which blocking takes place and in organic field effect transistors in the accumulation regime. This may be seen in Figure 4.4, which shows that within the ECDM the n and E dependences of the mobility are significantly smaller and larger, respectively, than within the EGDM. The experiments used in the present study probe the mobility most sensitively in the density range of $10^{22} - 10^{23} \text{m}^{-3}$, found in the bulk of the LEP layer of a device such as used for calculating the density profiles given in the inset (at 2 and 8 V). The two mobility functions cross in this carrier concentration range and both models lead to a comparable fitting quality.

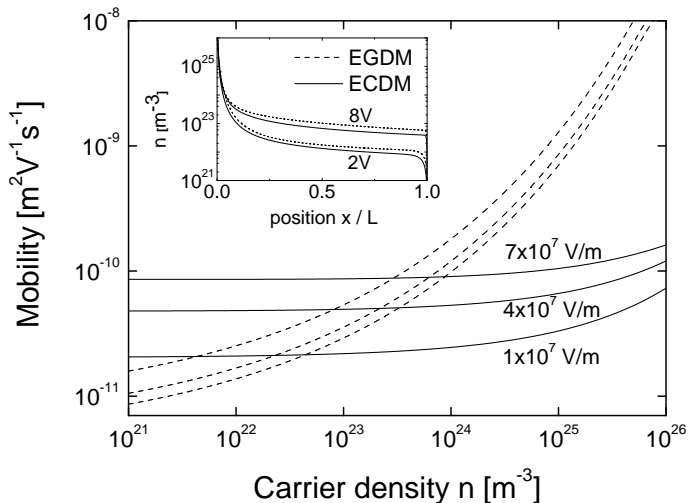


Figure 4.4: Carrier density dependence of the mobility for the ECDM (full curves) and for the EGDM (dashed curves) at 296 K and at various fields. The model parameters are given in Table 4.1. The inset shows for both models the carrier density in a 122 nm device; x is the distance to the anode.

4.4 Conclusions

In summary, for the copolymer studied, the ECDM yields over a wide temperature range and for three layer thicknesses an equally accurate description of the $J(V)$ -curves of sandwich-type devices as the EGDM. This shows that a successful analysis of the curves using either model does not yet convincingly prove that the disorder is completely random or correlated. So being able to describe $J(V)$ curves using a PF-type field-dependence of the mobility (as in the ECDM within a wide field range) does not yet prove that the site energies are correlated. In particular, for the specific material studied we argue that the site energies are uncorrelated, based on a comparison of the hopping site densities found using the two models with the amine density.

Bibliography

1. H. Bässler, *Phys. Status Solidi B* **175**, 15 (1993).
2. W. F. Pasveer, J. Cottaar, C. Tanase, R. Coehoorn, P. A. Bobbert, P. W. M. Blom, D. M. de Leeuw, and M. A. J. Michels, *Phys. Rev. Lett.* **94**, 206601 (2005).
3. C. Tanase, E. J. Meijer, P. W. M. Blom, and D. M. de Leeuw, *Phys. Rev. Lett.* **91**, 216601 (2003).
4. Y. Roichman, Y. Preezant, and N. Tessler, *Phys. Status Solidi A* **201**, 1246 (2004).
5. S. L. M. van Mensfoort, S. I. E. Vulto, R. A. J. Janssen, and R. Coehoorn, *Phys. Rev. B* **78**, 085208 (2008).
6. J. Zhou, Y. C. Zhou, J. M. Zhao, C. Q. Wu, X. M. Ding, and X. Y. Hou, *Phys. Rev. B* **75**, 153201 (2007).
7. J. J. M. van der Holst, M. A. Uijtewaal, R. Balasubramanian, R. Coehoorn, P. A. Bobbert, G. A. de Wijs, and R. A. de Groot, *Phys. Rev. B* **79**, 085203 (2009).
8. Y. N. Gartstein and E. M. Conwell, *Chem. Phys. Lett.* **245**, 351 (1995).
9. P. M. Borsenberger and D. S. Weiss, *Organic Photoreceptors for Xerography* (Dekker, New York, 1998).
10. G. Malliaras, Y. Shen, D. H. Dunlap, H. Murata, and Z. H. Kafafi, *Appl. Phys. Lett.* **79**, 2582 (2001).
11. S. V. Novikov, D. H. Dunlap, V. M. Kenkre, P. E. Parris, and A. V. Vannikov, *Phys. Rev. Lett.* **81**, 4472 (1998).
12. Y. Nagata and C. Lennartz, *J. Chem. Phys.* **129**, 034709 (2008).
13. S. V. Rakhmanova and E. M. Conwell, *Appl. Phys. Lett.* **76**, 3822 (2000).
14. Z. G. Yu, D. L. Smith, A. Saxena, R. L. Martin, and A. R. Bishop, *Phys. Rev. Lett.* **84**, 721 (2000).
15. M. Bouhassoune, S. L. M. van Mensfoort, P. A. Bobbert, and R. Coehoorn, *Org. Electron.* **10**, 437 (2009).
16. I. Grizzi, C. Foden, S. Goddard, and C. Towns, *Mater. Res. Soc. Symp. Proc.* **771**, 3 (2003).
17. R. U. A. Khan, D. Poplavskyy, T. Kreouzis, and D. D. C. Bradley, *Phys. Rev. B* **75**, 035215 (2007).
18. R. Coehoorn, W. F. Pasveer, P. A. Bobbert, and M. A. J. Michels, *Phys. Rev. B* **72**, 155206 (2005).

5

Electron transport in the small-molecule material Alq₃

In this chapter, the electrical characteristics of devices based on the well studied small-molecule material Alq₃ are analyzed using the ECDM, with the aim to obtain the mobility function of Alq₃ as well as the injection barrier in the devices employed. A good fit quality is found using a single set of materials and device parameters. From a consistency check on the zero field and electron density limit of the mobility μ_0 , strong indications for the presence of a significant injection barrier were found. Using the model with an injection barrier, a better consistency of the temperature and layer thickness dependence of μ_0 was indeed found. As viewed from a broader perspective, the performed analysis for electron transport first of all shows the necessity of using the parameter extraction method introduced in Chapter 2. The amount of parameters involved was found to require a robust extraction method. Secondly, the obtained mobility function is found to be very sensitive to the value of the injection barrier. Therefore an accurate extraction of the bulk mobility function requires detailed information about the interface properties which have to be included in a device model.

5.1 Introduction

We have studied the electron transport properties of tris(8-hydroxyquinolinato)aluminium (Alq₃), which is one of the archetypical small-molecule based OLED material. Previously, Berleb and Brütting¹⁻³ have extensively studied the electron transport characteristics of Alq₃ based devices using the empirical Poole-Frenkel mobility model. The goal of that work was to determine the charge carrier mobility in evaporation deposited layers of Alq₃, in which the molecular structure is highly disordered. For multiple reasons, this is not a straightforward task. First of all, Alq₃ typically contains electron trap states, which may be intrinsic for the material or due to impurities.⁴ Such trap states strongly influence the mobility of the electrons. Secondly, Alq₃ has a facial and a meridional isomer. Typically, the meridional isomer is the major constituent.^{5,6} The ratio of these constituents in a film is not *a priori* known and both have different transport properties. For example, Curioni *et al.*⁷ show the stronger degeneracy of the LUMO states of the meridional isomer with respect to the facial isomer. Figure 5.1 shows the chemical structure and localized LUMO of the meridional isomer of Alq₃.

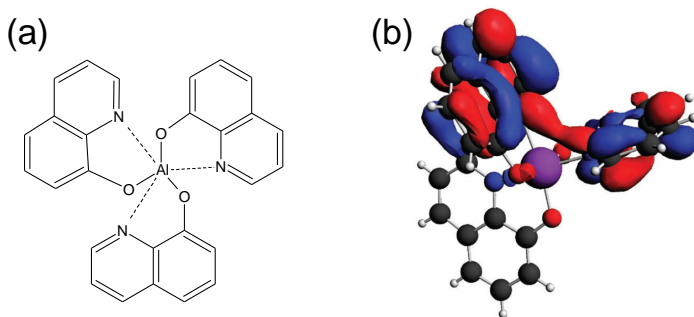


Figure 5.1: (a) Chemical structure of tris(8-hydroxyquinolinato)aluminium (Alq₃). (b) Visualization of the localized LUMO on the meridional isomer.⁶ The red and blue surfaces show the positive and negative part of the wave function.

Despite the fact that Alq₃ is not a simple material, it was found possible to measure a complete temperature and layer thickness dependent set of current-voltage characteristics and to use the empirical Poole-Frenkel mobility model to obtain a good fit to the current density versus voltage ($J(V)$) characteristics.¹⁻³ However, in Ref. 3 it was shown that a satisfying fit quality could only be obtained if for each layer thickness studied a different set of trap parameters was used. Furthermore, two simplifying assumptions were made. First, diffusion of charge carriers was neglected. Secondly, in the analysis of Berleb and Brütting,¹⁻³ no injection barrier for electrons at the electron injecting Ca-Alq₃ electrode interface occurring in the devices studied was assumed. The authors noted that various others⁸⁻¹³ had shown that the formation of a dipole layer at the interface can strongly influence charge injection at a metal-Alq₃ interface. This leads to the

question whether an interface barrier is present in these devices. Answering this question is very important because neglecting an interface barrier can strongly affect the obtained bulk mobility in any model. In the extreme case of injection limited transport, the barrier fully determines the current which can then be described as:¹

$$J = e\mu(n(F), F)\frac{V}{L}, \quad (5.1)$$

with e the elementary charge, μ the mobility, n the charge carrier density, V the applied voltage, L the Alq₃ thickness and F the electric field.

In this chapter it is investigated whether more advanced transport models such as the ECDM or the EGDM, and a device model which also includes diffusion, can lead to a similarly good or even better description of the $J(V)$ curves as the Poole-Frenkel model used in Refs. 1–3. Within an EGDM or ECDM study, a single set of physically interpretable materials and device parameters is used. Subsequently, the question whether these models can be used to detect the presence of an injection barrier, which determines the current, is addressed. Finally, based on a comparison of the parameter values as obtained using the EGDM and the ECDM, one may investigate whether or not correlations in energy between hopping sites are present. This was already theoretically studied for holes using Molecular Dynamics calculations by various authors in Refs. 14–16. Nagata *et al.*^{14,15} showed that the correlations in Alq₃ are confined to one or at most two neighbors. Experimentally, this question was also studied by Van Mensfoort *et al.*^{17–20} for various other materials. It was found that for the small-molecule materials studied, the ECDM was more applicable. In Section 5.2 an overview is given of the experimental data used, and a comparison is given with $J(V)$ curves obtained for additional devices fabricated in our own laboratory. In order to address the questions posed, Section 5.3 gives the ECDM fit results, with and without an injection barrier, to current-voltage curves experimentally obtained by Berleb and Brütting.^{1–3} In an Appendix, the EGDM results on these data without an injection barrier are presented. A summary and conclusions are presented in Section 5.4.

5.2 Experimental results

5.2.1 $J(V)$ curves of samples employed in the analysis

The $J(V)$ curves employed in the EGDM and ECDM analysis presented in this chapter were taken from the work by Berleb and Brütting,^{1–3} from the University of Bayreuth, who investigated systems with the structure:

$$| \text{Al anode (30 nm)} | \text{Alq}_3 | \text{Ca (10 nm)} | \text{Al cathode (100 nm)} |.$$

The Alq₃ used in the devices was well purified by multiple sublimation steps and was evaporation deposited on top of the Al anode. Subsequently, the Ca-Al cathode was evaporated. A plot of the measured current density versus the

average field V/L is shown in Figure 5.2. It shows that at room temperature, the measured current density at a certain field is rather independent of the Alq₃ layer thickness. This is an indication that an interface barrier plays a role. At lower temperatures the curves are more thickness dependent, which shows that the transport is not fully injection limited.

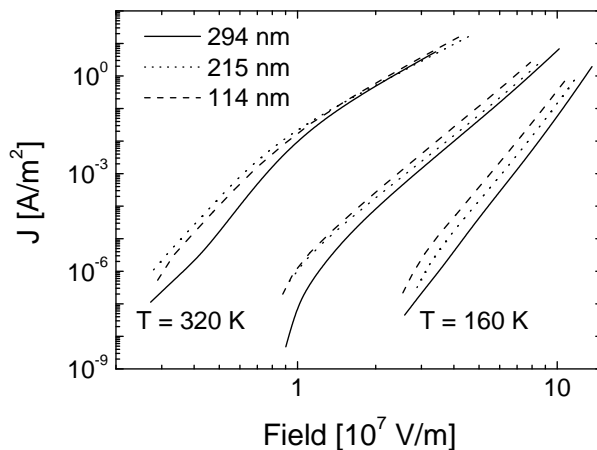


Figure 5.2: Measured current-density versus the average field for devices with an Alq₃ film thickness of 294, 215 and 114 nm at 320, 220 and 160 K. These data were measured by Berleb and Brütting.¹⁻³ The average field is defined as V/L .

5.2.2 Additional transport studies of Alq₃ devices

To further study the transport properties and the reproducibility of Alq₃ device fabrication, new samples were made at Philips Research Eindhoven. The devices have the same structure as the devices presented in Section 5.2.1. The devices were made by evaporation deposition with an evaporation rate of 1 Å/s. Figure 5.3 shows the measured room temperature current density versus average field. Clearly, the current density for the nominally 100, 200 and 300 nm thick devices is different at a given average field. This shows that these devices are not fully injection limited. The current density is smaller than as found by Berleb and Brütting (for a comparable Alq₃ thickness), and the effect of space charge on the Alq₃ thickness dependence is much more pronounced.

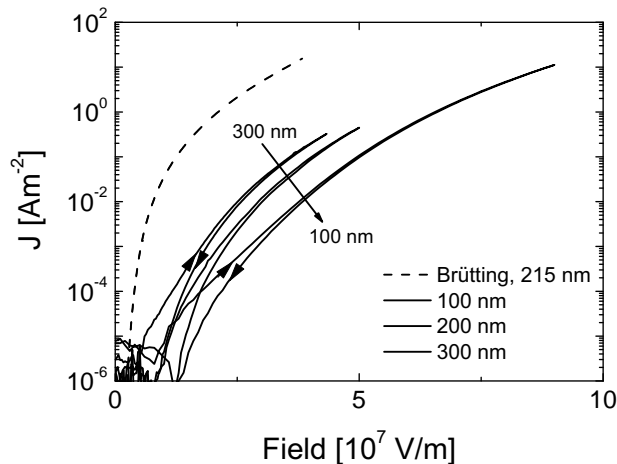


Figure 5.3: Measured current-density versus average field characteristics at room temperature (drawn curves) for AlQ_3 layer thicknesses of 100, 200 and 300 nm. Also, the room temperature curve of Berleb and Brütting¹⁻³ of a 215 nm device is shown (dashed curve).

In Figure 5.4 the results of capacitance voltage measurements are shown, measured at a frequency of 200 Hz. A voltage independent capacitance is obtained and the ratio between the values obtained closely matches the nominal inverse thickness ratio (1 : 1/2 : 1/3) of the new devices. The absence of a peak around the built-in voltage indicates that a sizeable injection barrier is likely to be present.²¹ Also Berleb and co-workers used impedance spectroscopy to study the capacitance in their devices.²² They found that the frequency dependence of the capacitance showed a clear minimum for every bias voltage studied in the range 4 – 10 V. It was concluded that this reveals the dispersive nature of the electron transport in these AlQ_3 based devices. In their work on these systems the voltage dependence of the capacitance was not studied.

5.2.3 Selection of $J(V)$ characteristics studied

The new samples were used to investigate to what extent the $J(V)$ curves of nominally identical devices, made in different laboratories are similar. Figure 5.3 shows the measured room temperature current versus average field for several layer thicknesses and a comparison with a 215 nm device as studied by Berleb and Brütting.¹⁻³ It can be seen that despite the well purified AlQ_3 used in both cases and despite the identical device design, a different $J(V)$ characteristic is obtained for the ~ 200 nm thick devices. This suggests a strong dependence on

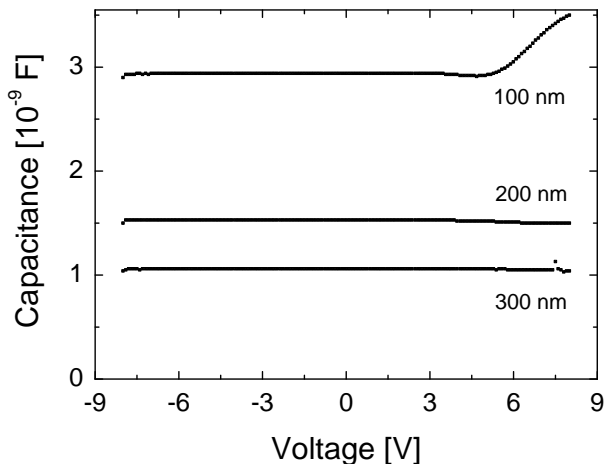


Figure 5.4: Measured capacitance-voltage curves for the devices also shown in Figure 5.3. The devices were studied at room temperature ($T = 298$ K) and at a frequency of 200 Hz. A nearly voltage independent capacitance is obtained, indicating the presence of an injection barrier at the electron injecting contact. The device area is 9 mm^2 and the measured capacitance leads to $\epsilon_r = 3.8 \pm 0.3$. This is consistent with the value of 3.5 reported in Ref. 4.

material purity and/or deposition conditions, which was also noticed in Refs. 1–3 and 23. To systematically study transport in Alq_3 , a set of devices made under identical deposition conditions and based on material from the same batch should be used. Therefore we decided to base the further modeling study on the experiments described by Berleb and Brütting^{1–3} who studied Alq_3 devices over a wide temperature range and a wide range of different layer thicknesses. Obviously, the obtained results will be specific for these devices.

We remark that the measurements shown in Figure 5.3 show a difference between the upward and the downward voltage sweep. This difference can be due to charging effects as a consequence of relatively slow charge carrier relaxation processes.²⁴ In Chapter 6 a study which aims at including time-dependent effects in a charge transport model is presented. In our experiments the characteristics were measured in voltage steps of 0.1 V at time intervals of 1 s. The time-scales in the measurements of Berleb and Brütting^{1–3} were chosen such that the difference between both sweeps is minimal. In the steady-state transport study presented in the next section, the upward $J(V)$ curves are considered (i.e. the curves shown in Figure 5.2).

5.2.4 Amorphous nature of Alq₃ films

Hopping models such as the Poole-Frenkel mobility model and also the ECDM or EGDM can describe transport in amorphous organic materials. For Alq₃ it is however argued that also small crystallites can be present in evaporated thin films.²⁵ Also Tang and VanSlyke reported on microcrystalline ordering of Alq₃ in their pioneering work on OLEDs.²⁷

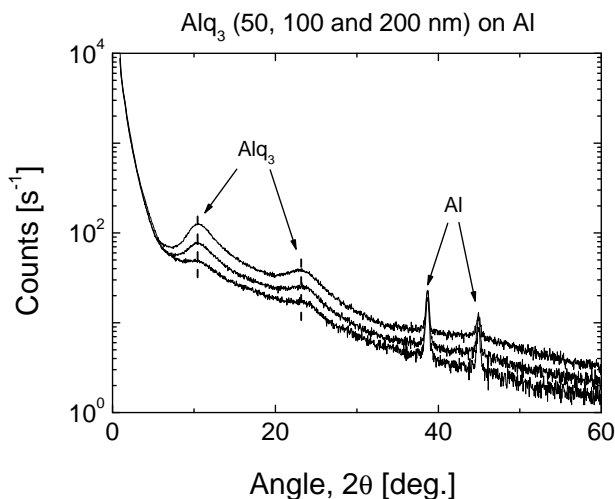


Figure 5.5: Grazing incidence X-ray diffractograms for Alq₃ films on Al, showing the scattered intensity as a function of the 2θ scatter angle. The lowest curve corresponds to a 50 nm thick film, the middle to a 100 nm thick film and the upper curve to a 200 nm film. The broad peaks around 11° and 22° are due to scattering in the Alq₃ film. The widths of these peaks indicate the amorphous or at most nanocrystalline nature of the films.

In order to investigate the possible crystalline order in thin film Alq₃, several films were deposited on a glass-Al substrate and subsequently analyzed by X-ray diffraction (XRD). The evaporation rate was $1.5 - 3 \text{ \AA/s}$ and the substrate was at room temperature during the deposition. Subsequently, the measurements were performed in air with an X'Pert MPD diffractometer, equipped with a Cu X-ray source. A grazing incidence configuration was applied to achieve a high surface sensitivity. The diffractogram in Figure 5.5 shows two broad peaks at $\sim 11^\circ$ and $\sim 22^\circ$ which originate from the Alq₃ layer. This can be concluded since the intensity of the peaks increases with increasing layer thickness. Moreover, a reference sample without an Alq₃ film shows no peaks at these angles. The two narrow peaks at about 39° and 45° originate from the Al layer. This was concluded from a comparison with data from the International Centre for Diffraction. There

is no dependence of the Alq₃-related peak width or position on the Alq₃ film thickness. The width of the peaks can be used to judge whether the material is amorphous.²⁶ An estimation of the crystallite size can be given using the Scherrer equation, which assumes grain boundaries as the only imperfections of a crystal. Using this equation, a maximum average crystallite size of 3 nm is found, which shows the material is amorphous or at most nanocrystalline.

In conclusion, no or only nano-scale crystalline order is found in the Alq₃ films on Al fabricated in our laboratory. Therefore, expectedly, the hopping transport models for amorphous organic materials such as the EGDM and the ECDM can be used to describe the charge transport in these Alq₃ based devices. We assume that this also holds for the Alq₃ based devices of Berleb and Brütting.¹⁻³

5.3 ECDM results and discussion

The $J(V)$ characteristics measured by Berleb and Brütting¹⁻³ for Alq₃ based electron-only devices have been analyzed using the ECDM. The device model is based on physically interpretable parameters and includes diffusion. Also an exponential distribution of trap states is taken into account as mentioned in Chapter 1. As a first step to investigate the question whether consistent modeling is possible using a single set of parameters, no injection barrier is assumed. A one-dimensional drift-diffusion solver is employed as described in Ref. 28. Figure 5.6 shows the good fit which was obtained using a single set of parameters to describe the shape of the density of states.

Table 5.1 (first column) shows the materials and device parameters for every device, as found using the “grid approach”. The parameters were obtained by minimizing the “fit error” which is the sum of errors of $J(V)$ curves at three thicknesses (114, 215 and 294 nm) and at three temperatures (320, 220 and 160 K). This optimization was done by a systematic variation of the density of states parameters on a grid as will be shown in Figure 5.8. The obtained best fit site density within the ECDM is $(0.5 - 2) \times 10^{27} \text{ m}^{-3}$, which is consistent with the experimental Alq₃ density of $2 \times 10^{27} \text{ m}^{-3}$. The obtained value for the width of the DOS σ is 0.11 eV which is close to the value of 0.12 eV obtained in Refs. 1–3. In the optimization the built-in voltage and the mobility μ_0 in the limit of zero electron density and field are free parameters. These parameters are used to check the consistency of the modeling. The built-in voltage is found to be temperature independent. A value of $1.2 \pm 0.1 \text{ V}$ is obtained for the 114 and 215 nm thick devices which is in line with the earlier work. For the 294 nm device the obtained built-in voltage is $1.8 \pm 0.1 \text{ V}$ which is significantly higher. This was also found in the earlier work and can be due to a device-specific interfacial dipole layer.

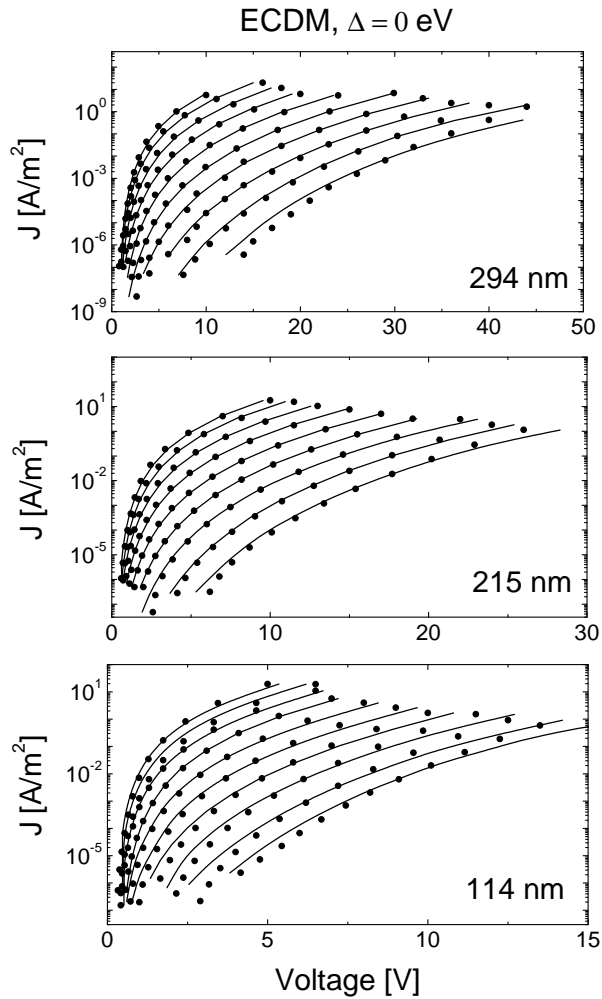


Figure 5.6: ECDM fit results (solid lines) for three devices with different organic layer thicknesses (114, 215 and 294 nm). For every device, the temperature dependence of the $J(V)$ characteristics is modeled, for temperatures in the range 140 – 320 K in steps of 20 K. For the 215 nm device the lowest temperature is 160 K.

Figure 5.7 shows the obtained values of the mobility μ_0 in the limit of zero field and charge carrier density for every temperature and layer thickness investigated. A slope parameter C as defined in Eq. 1.7 equal to 0.39 is obtained and a best fit is shown in Figure 5.7. The expected value for the C -parameter within the ECDM assuming Miller Abrahams hopping is 0.29; therefore the obtained value is unexpectedly high. It should be noted however that recent work of Cottaar *et al.*²⁹ shows that also higher values of C are possible if Marcus-theory is assumed. Another remarkable result from the modeling is that at every temperature, an increasing mobility μ_0 is obtained with increasing thickness. This effect can also be seen in detail in the inset of Figure 5.7, for 9 devices at room temperature. This shows that the model is not internally consistent. A consistent model describing the bulk Alq₃ mobility would yield thickness independent μ_0 values.

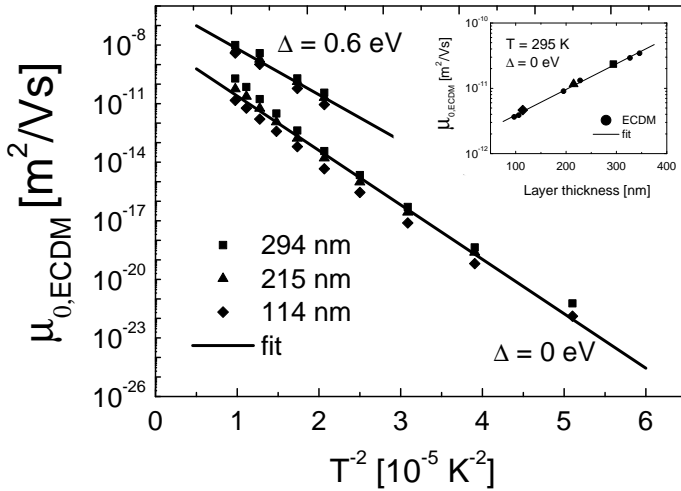


Figure 5.7: Obtained values for the mobility μ_0 for every temperature and layer thickness shown in Figure 5.6. Also a best fit to the data is given. The inset shows the obtained thickness dependent mobility μ_0 for 9 devices at room temperature. If an injection barrier of 0.6 eV is taken into account, a significantly higher μ_0 value is obtained, and the layer thickness dependence becomes smaller.

A systematic variation of the density of states parameters was performed, varying pairwise σ and N_t or $N_{t,\text{trap}}$ and T_0 , while keeping the other parameters fixed, as can be seen in Figure 5.8(a) and (b), respectively.

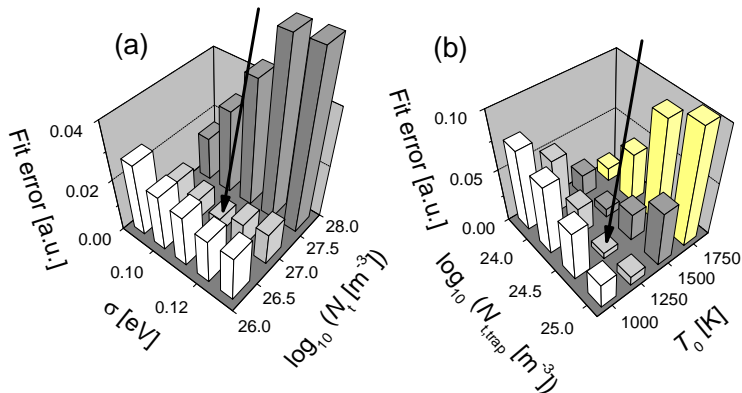


Figure 5.8: Fit error for various different parameter value combinations. A clear minimum is found and is indicated with an arrow. In (a), σ and N_t are varied at the best fit values of T_0 and $N_{t,\text{trap}}$ as shown in (b). In (b), a similar variation is performed for the trapping parameters at the best fit σ and N_t value.

The arrows point at the best fit parameter combination given in Table 5.1. From this “grid approach” it can not yet be excluded that a similar fit quality as obtained for the optimum indicated can be obtained at a different parameter combination. Using this approach any further would lead to a very time consuming parameter extraction, since one would have to calculate 9 $J(V)$ curves for every possible parameter combination chosen on the grid. In order to study the correlated uncertainties in the parameter values obtained in more detail, the parameter extraction method developed in Chapter 2 can be used. However, we limit the discussion in this chapter to an analysis of the parameter values found as a function of L and T .

The thickness dependence of the mobility in the zero density and field limit, $\mu_0(T)$, shown in Figure 5.7, can be seen as an indication that there is an electron injection barrier. This can be understood by reasoning as follows. If there were an injection barrier it would mostly affect the current in the thinnest device. In a model without a barrier, this leads to a too low bulk mobility. This effect is less strong in a thicker device. The obtained thickness dependent mobility μ_0 points at the presence of an interface barrier which influences the current. An injection barrier can be taken into account in the model. Figure 5.9 shows the modeling results using the ECDM with an 0.6 eV injection barrier. This value was suggested by Campbell *et al.*¹³ based on internal photoemission experiments. In our modeling no image charge correction to the barrier, as for instance in Ref. 20, is taken into account. Furthermore a fixed realistic site density ($1 \times 10^{27} \text{ m}^{-3}$) and width of the density of states ($\sigma = 0.11 \text{ eV}$) as obtained in the former analysis were used. Subsequently, the parameter extraction method presented in Chapter 2 was employed to obtain the best fit trap parameters, built-in voltages and values for

Table 5.1: Best fit ECDM and EGDM materials and device parameters. The parameters were either set or, for the cases without an injection barrier, obtained using the “grid approach”. For the built-in voltages a margin is indicated since the obtained values lie in that region. Also the best fit slope parameter C of the temperature dependence of the mobility (μ_0) and the zero temperature limit μ_0^* of that mobility are given. Values with an asterisk were kept fixed.

Parameter	ECDM	ECDM	EGDM
Δ [eV]	0*	0.6*	0*
N_t [10^{26} m^{-3}]	10	10*	2
σ [eV]	0.11	0.11*	0.09
$N_{t,\text{trap}}$ [10^{24} m^{-3}]	5	10	5
T_0 [K]	1250	1381	1250
V_{bi} 294 nm [V]	1.8 ± 0.1	1.1 ± 0.1	1.8 ± 0.1
V_{bi} 215 nm [V]	1.2 ± 0.1	0.8 ± 0.1	1.2 ± 0.1
V_{bi} 114 nm [V]	1.2 ± 0.1	0.8 ± 0.1	1.2 ± 0.1
C	0.39	0.33	0.43
μ_0^* [$\text{m}^2\text{V}^{-1}\text{s}^{-1}$]	$(0.3 - 3) \times 10^{-8}$	$(1 - 2) \times 10^{-6}$	$(0.3 - 6) \times 10^{-7}$

$\mu_0(T)$. An overview of the parameters which were fixed and obtained are shown in Table 5.1 (second column). The extraction was based on the $J(V)$ characteristics of the 114 and 215 nm thick devices using the 320 and 220 K curves. Subsequently, the $J(V, T)$ curves for intermediate temperatures and of the 294 nm thick device were fitted using the obtained parameters. Figure 5.9 shows the ECDM fit results. It can be seen that the overall fit quality is somewhat lower as compared to the case without an injection barrier. This can be due to the choice to fix the site density, and the width of the density of states. Therefore the obtained fit quality cannot be used to make a distinction between the different approaches. However, when using a 0.6 eV injection barrier, the mobility $\mu_0(T)$ depends much less on layer thickness as can be seen in Figure 5.7. Moreover the slope parameter C now equals 0.33, which is closer to the expected value of 0.29 for the ECDM. In Ref. 2 it was already argued that the thickness dependence of the $J(V, T)$ characteristics provides crucial information on the transport mechanism. This point is confirmed by this analysis, which shows that an interface barrier is present.

In Appendix 5.5 an EGDM analysis without an injection barrier of the $J(V)$ characteristics is presented. Also in this case, a good fit quality is found. However, the thickness dependence of the mobility μ_0 is even stronger than for the ECDM without an injection barrier. This shows that also the EGDM does not give a consistent description without an injection barrier. Furthermore, the optimal site density is found to be equal to $2 \times 10^{26} \text{ m}^{-3}$, which is a factor 10 smaller than the experimental value. This finding provides an indication that positional correlation should be included when modelling electron transport in Alq₃.

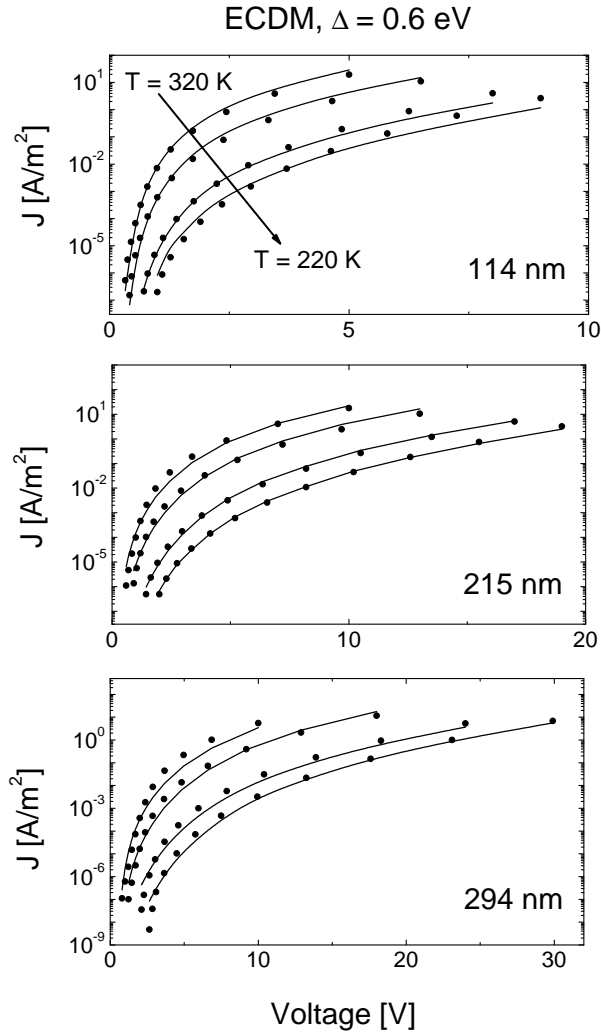


Figure 5.9: Best fit results using the ECDM with a 0.6 eV injection barrier. Parameter extraction is used for the 114 and 215 nm thick devices to obtain the best fit trap parameters, built-in voltages and μ_0 values. Subsequently, the intermediate temperatures and 294 nm device $J(V,T)$ characteristics were fitted using these parameters.

5.4 Summary and conclusions

In this chapter, we have investigated to what extent the electron transport in Alq₃ based devices can be consistently described within the EGDM and the ECDM. As a first step, evaporation deposited Alq₃ films and Alq₃ based devices were made. The films were made in order to study the molecular structure using X-ray diffraction. The diffractograms confirmed the absence of crystalline order in the evaporated Alq₃ films. Therefore, hopping transport models for amorphous organic materials, such as the EGDM and the ECDM, are expected to be applicable to describe the charge transport in the Alq₃ based devices made.

The newly made electron-only devices were found to give significantly different $J(V)$ curves (see Figure 5.3) as compared to those obtained for nominally identical devices studied in earlier work Refs. 1–3. The difference can be due to the level of purity of the material or differences in the evaporation conditions. In this case, the devices studied were made on different machines which inevitably leads to at least slightly different evaporation conditions under nominally identical conditions. This can have a significant effect on the transport characteristics. We have therefore concluded that a modeling study on the transport properties can only be performed on devices based on the same batch of Alq₃ which are made under the same deposition conditions and in the same machine. This implies that the results of such a study are specific for these devices. The value of such a modeling study is however also to develop a strategy to consistently determine the bulk mobility (function). We have chosen to use the extended set of $J(V)$ characteristics published in Refs. 1–3 for this purpose. The electron-only current-voltage characteristics of these Alq₃ based single-layer devices were modeled using the ECDM and the EGDM.

If no injection barrier is assumed, a good fit to the temperature and layer thickness dependent data is obtained using the ECDM and using a single set of materials parameters which describe the density of states. A site density of $1 \times 10^{27} \text{ m}^{-3}$ is obtained, which is a realistic value since an Alq₃ density of $2 \times 10^{27} \text{ m}^{-3}$ was measured.^{1–3} Furthermore, a value for the width of the density of states of $\sigma = 0.11 \text{ eV}$ was obtained. This value is close to the 0.12 eV obtained in Refs. 1–3. The obtained value is also close to the 0.13 eV obtained by Lee *et al.*³⁰ based on time of flight measurements. It is however found that the model is not fully internally consistent, as a layer thickness dependent value of the mobility in the zero electron density and field limit, $\mu_0(T)$, is obtained. At room temperature, $\mu_0(T)$ varies over more than an order of magnitude with the device thickness, as shown in Figure 5.7. This suggests that an electron injection barrier plays an important role. This can be understood as follows. If there is an injection barrier, it would most strongly affect the current in the thinnest device. In a model without an injection barrier, this leads to a too low bulk mobility. This effect is less strong in a thicker device. Therefore the obtained thickness dependence of $\mu_0(T)$ points at the presence of an interface barrier which influences the current. A similar conclusion was obtained by reanalyzing the $J(V)$ curves using the EGDM, again neglecting an electron injection barrier.

By including an injection barrier ($\Delta = 0.6 \text{ eV}$) in the model, the thickness

dependence of μ_0 decreases significantly, as shown in Figure 5.7. It can be seen that, for instance at room temperature, the obtained bulk mobility increases by ~ 2 orders of magnitude (see also $\mu_{0,\text{ECDM}}^*$ in Table 5.1). This clearly shows that an interface barrier has to be included to come to a consistent model. A correct extraction of the bulk mobility requires thus a consistent model which properly includes the metal-organic interface.

The presence of an interface barrier can strongly determine the shape of the $J(V)$ characteristics. The density of states parameters obtained from a model. Depend strongly on this shape. This makes a correct inclusion of the interface barrier crucial for a consistent description. The EGDM analysis, carried out for $\Delta = 0$ eV, was found to provide indications that positionally correlated disorder should be included, as in the ECDM. However, in order to provide stronger evidence, an important next step would be to reanalyze the $J(V)$ characteristics using the EGDM with an injection barrier. This would make it possible to directly compare with the ECDM results and to draw a more firmly founded conclusion about the possible presence of correlated disorder based on a comparison of the obtained site densities.

5.5 Appendix: EGDM results and discussion

Figure 7.3 shows the obtained best fit using the EGDM without an injection barrier. The best fit parameters, obtained by the same method as described in Section 5.3, are shown in Table 5.1 (second column). In the present approach, the built-in voltages and μ_0 values were left free for every $J(V)$ curve studied. A comparable or, at low temperatures, even higher fit quality as obtained using the ECDM (see Figure 5.6) was found. In the lower voltage range where diffusion plays an important role, a better fit is obtained than found by Berleb and Brütting.^{1–3} Figure 5.11 shows the fit error versus the width of the density of states (σ) and hopping distance ($N_t^{-\frac{1}{3}}$), taking all other parameters fixed at the values given in Table 5.1. In Figure 5.11(a) it can be seen that at the indicated experimental Alq₃ distance (corresponding site density $N_t = 2 \times 10^{27} \text{ m}^{-3}$) the fit error is significantly higher than at the best fit average hopping distance ($\sim 2 \text{ nm}$). The minimum corresponds to a site density of about $2 \times 10^{26} \text{ m}^{-3}$. This value is clearly significantly lower than the experimental Alq₃ density. A similar extraction was performed for the trapping parameters which led to the values given in Table 5.1. More thorough parameter extraction can be done using the method presented in Chapter 2. Figure 5.11(b) includes the results obtained if the 160 K data are included. The figure shows the trend of increasing fit error with increasing σ . If the 160 K data are included, a clear best fit σ value of about 0.09 eV is observed.

The built-in voltages, see Table 5.1, come out very similar as for the ECDM extraction. The obtained value of μ_0 is found to be strongly thickness dependent, see Figure 5.12. At room temperature, μ_0 is for the thickest device about 2 orders of magnitude higher than for the thinnest device. The effect is even stronger than for the ECDM (see Figure 5.7) and points at the presence of an injection barrier at the electrode interface. For every thickness studied, the best fit temperature dependence according to Eq. 1.7 is shown. The average slope parameter C for these fits is 0.43, which is within the range of 0.4–0.5 expected from the underlying theory.³¹ If an injection barrier would be taken into account this value will most likely decrease as shown for the ECDM in Section 5.3.

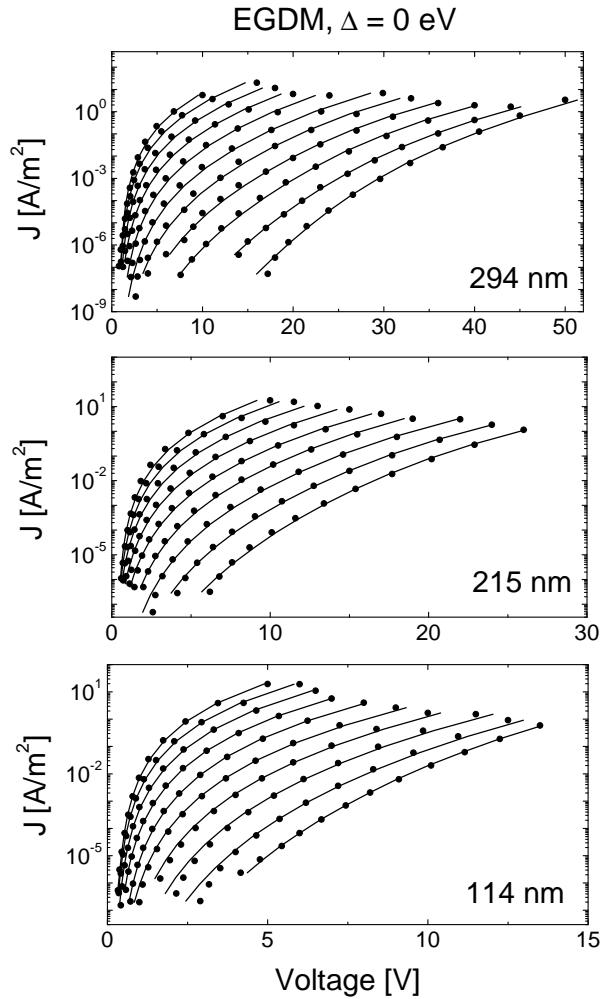


Figure 5.10: Best fit results using the EGDM without an injection barrier. $J(V)$ characteristics were fitted in a temperature range between 140 and 320 K in steps of 20 K. For the 215 nm thick device, the lowest temperature is 160 K.

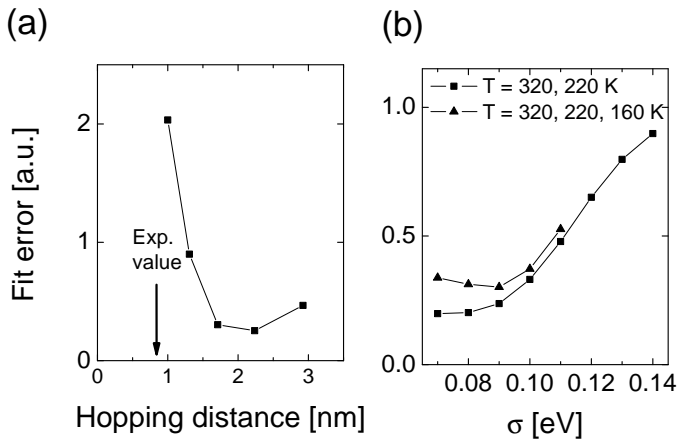


Figure 5.11: Obtained fit error as a function (a) of the average hopping site distance and (b) the width of the density of states. In (a), the arrow indicates the experimentally determined average intermolecular Alq₃ distance.

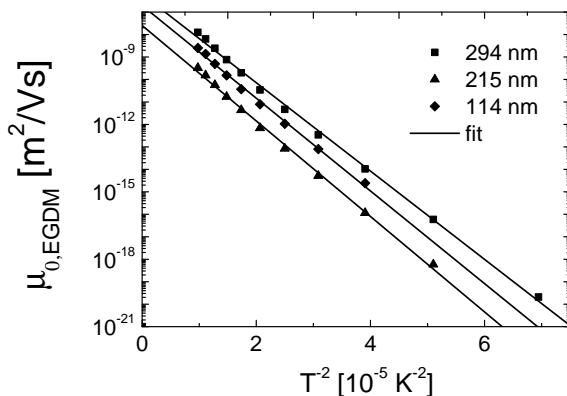


Figure 5.12: Temperature dependence of the mobility μ_0 as obtained using the EGDM. For every thickness, the best fit temperature dependence is shown. An average slope parameter C equal to 0.43 is obtained and a strong thickness dependence can be observed.

Bibliography

1. W. Brütting, S. Berleb, and A. G. Mückl, *Org. Electron.* **2**, 1 (2001).
2. W. Brütting, S. Berleb, and A. G. Mückl, *Synth. Met.* **122**, 99 (2001).
3. *Raumladungsbegrenzte Ströme und Hoppingtransport in organischen Leuchtdioden aus Tris-(8-hydroxyquinolin)-Aluminium (Alq₃)*, S. Berleb, PhD thesis University of Bayreuth (2001).
4. G. G. Malliaras, Y. Shen, D. H. Dunlap, and Z. H. Kafafi, *Appl. Phys. Lett.* **79**, 2582 (2001).
5. R. L. Martin, J. D. Kress, I. H. Campbell, and D. L. Smith, *Phys. Rev. B* **61**, 15804 (2000).
6. J. J. Kwiatkowski, J. Nelson, and W. Wenzel, *Phys. Chem. Chem. Phys.* **10**, 1852 (2008).
7. A. Curioni, M. Boero, and W. Andreoni, *Chem. Phys. Lett.* **294**, 263 (1998).
8. R. Steyrleuthner, M. Schubert, F. Jaiser, J. C. Blakesley, Z. Chen, A. Facchetti, and D. Neher, *Adv. Mater.* **22**, 2799 (2010).
9. S. K. M. Jönsson, W. R. Salaneck, M. Fahlman, *J. Appl. Phys.* **98**, 014901 (2005).
10. A. Uddin, C. B. Lee, X. Hu, and T. K. S. Wong, *Appl. Phys. A* **78**, 401 (2004).
11. M. A. Baldo and S. R. Forrest, *Phys. Rev. B* **64**, 085201 (2001).
12. E. Tutiš, M. N. Bussac, and L. Zuppiroli, *Appl. Phys. Lett.* **75**, 24 (1999).
13. I. H. Campbell and D. L. Smith, *Appl. Phys. Lett.* **75**, 4 (1999).
14. Y. Nagata and C. Lennartz, *J. Chem. Phys.* **129**, 034709 (2008).
15. Y. Nagata, *Chem. Phys. Chem.* **11**, 474 (2010).
16. A. Lukyanov and D. Andrienko, *Phys. Rev. B* **82**, 193202 (2010).
17. S. L. M. van Mensfoort, S. I. E. Vulto, R. A. J. Janssen and R. Coehoorn, *Phys. Rev. B* **78**, 085208 (2008).
18. R. J. de Vries, S. L. M. van Mensfoort, V. Shabro, S. I. E. Vulto, R. A. J. Janssen, and R. Coehoorn, *Appl. Phys. Lett.* **94**, 163307 (2009).
19. S. L. M. van Mensfoort, V. Shabro, R. J. de Vries, R. A. J. Janssen and R. Coehoorn *Phys. Rev. B* **80**, 033202 (2009).
20. S. L. M. van Mensfoort, R. J. de Vries, V. Shabro, C. van der Marel, H. P. Loebel, R. A. J. Janssen and R. Coehoorn, *Org. Electron.* **11**, 1408 (2010).

21. S. L. M. van Mensfoort and R. Coehoorn *Phys. Rev. Lett* **100**, 086802 (2008).
22. S. Berleb and W. Brütting, *Phys. Rev. Lett.* **89**, 286601 (2002).
23. C. B. Lee, A. Uddin, X. Hua, and T. G. Andersson, *Materials Science & Engineering B* **112**, 14 (2004).
24. W. Chr. Germs, J. J. M. van der Holst, S. L. M. van Mensfoort, P. A. Bobbert, and R. Coehoorn, *Phys. Rev. B* **84**, 165210 (2011).
25. M. Rajeswaran, T. N. Blanton, C. W. Tang, W. C. Lenhart, S. C. Switalski, D. J. Giesen, B. J. Antalek, T. D. Pawlik, D. Y. Kondakov, N. Zumbulyadis, and R. H. Young, *Polyhedron* **28**, 835 (2009).
26. *X-ray diffraction procedures for polycrystalline and amorphous materials*, H. P. Klug and L. E. Alexander, Wiley (1954).
27. C. W. Tang and S. A. VanSlyke, *Appl. Phys. Lett.* **51**, 913 (1987).
28. S. L. M. van Mensfoort and R. Coehoorn, *Phys. Rev. B* **78**, 085207 (2008).
29. J. Cottaar, R. Coehoorn, and P. A. Bobbert, unpublished.
30. C. B. Lee, A. Uddin, and T. G. Andersson, *Solid State Commun.* **142**, 206 (2007).
31. R. Coehoorn, W. F. Pasveer, P. A. Bobbert, and M. A. J. Michels, *Phys. Rev. B* **72** 155206 (2005).

6

Experimental and modeling study of dark injection transients

A challenge which is often encountered in studying electron transport in materials such as Alq₃ or NET-5, see Chapter 5 and 7, respectively, is how to treat hysteresis effects which lead to a significant experimental uncertainty in measured $J(V)$ characteristics. Ideally, a transport model would be available that includes such time and device history dependent effects. In this chapter the EGDM is used to describe the time-dependence of the measured current-density as obtained by so-called dark injection measurements on PF-TAA based hole-only devices, which provide an effective charge carrier transit time. A systematic study on several device layer thicknesses and at various voltages was performed and a critical comparison with the prediction as obtained from the EGDM model was made. Excellent agreement concerning the voltage and layer thickness dependence of the effective transit time is found, albeit that the observed transit time is systematically smaller than as predicted and the steady-state current density is approached more slowly than as predicted. It is argued that the inclusion of charge carrier relaxation effects, which lead to a time dependence of the mobility, can improve the description.

6.1 Introduction

In Chapter 4 a device model was used to derive the mobility function from a study of the $J(V)$ characteristics of sandwich-type organic semiconductor devices. There are various other experimental techniques that provide information about the mobility. Examples are Time-of-Flight (TOF)^{1,2} and Dark Injection (DI) measurements³⁻⁵. In a DI experiment a voltage pulse is applied to for example an OLED and the current response is measured. In a typical experiment, the transient current density shows a distinct peak, before decreasing gradually to the steady-state current density. The peak occurs when the front of carriers that have been injected at $t = 0$ and that have subsequently filled the device, arrive at the other electrode. Therefore, the peak time, τ_p , may be viewed as an effective transit time. The peak time is often used as a measure for the mobility. In a simple theory,³ assuming a constant mobility and neglecting charge carrier diffusion and possible injection barriers at the interfaces, the mobility μ follows from:

$$\mu = 0.787 \frac{L^2}{\tau_p V}, \quad (6.1)$$

where L is the device thickness and V the applied voltage. The voltage at $t < 0$ is assumed to be zero. Poplavskyy *et al.*⁴ have studied DI transients for hole-only sandwich type devices based on a green-emitting polyfluorene based copolymer. Using Eq. 6.1, they found a Poole-Frenkel (PF) electric field dependence of the mobility (see Eq. 2.8 in Chapter 2). It is often found that the mobility as obtained using TOF and DI experiments is very different for the same system. A better understanding of this discrepancy would require a device model that can be used to describe the experiment. Such a step would be very interesting, because a better understanding of the time-dependent response would also give insight into the frequently encountered hysteresis or charge carrier relaxation processes in organic materials. These processes often make studying electron transport properties a challenging task. This difficulty has been encountered in several electron transport studies and is described in Chapter 7. Recently, Knapp *et al.*⁶ have used the EGDM⁷ to calculate the time-dependent response of the current-density using a one-dimensional drift-diffusion model. The availability of such simulations makes it now possible to describe the time-dependent DI experiments, including the effects of disorder on the mobility. In the past, the EGDM was used to predict the current-voltage characteristics⁸ of the polyfluorene-based hole transport devices introduced in Section 1.1.1. EGDM-based device models were also used to successfully describe electro-absorption⁹ and capacitance-voltage¹⁰ measurements, carried out for the same devices. Now the question arises whether it is also possible to describe measured DI transients in these devices using the EGDM, which includes the effects of energetic disorder, without introducing new fit parameters or changing the materials and device parameters determined from the steady-state $J(V)$ curves. In order to investigate this, a critical comparison between measured and modelled DI transients is made for these polyfluorene based devices.

6.2 Experimental

The systems studied were polyfluorene based sandwich-type OLED devices introduced in Chapter 1. The material consists of randomly copolymerized fluorene with triarylamine monomer units (PF-TAA). The DI transients were measured in the setup depicted in Figure 6.1(a). The time-dependent current is obtained by measuring the voltage (V_{probe}) over a series resistor (R). The measured response is the result of a voltage pulse train ($V(t)$) as depicted in Figure 6.1(b). The voltage is stepwise varied between V_0 and V_1 with a duty cycle defined as $t_{\text{pulse}}/t_{\text{tot}} \cdot 100\%$.

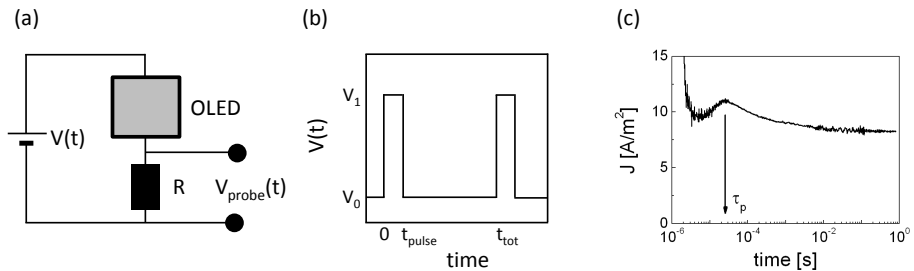


Figure 6.1: Experimental setup (a) for measuring dark injection transients. The $3 \times 3 \text{ mm}^2$ OLED is placed in series with a resistor R over which a voltage response V_{probe} is measured. This response is the result of an applied voltage pulse train $V(t)$ shown in (b). During a time t_{pulse} a high voltage V_1 is applied, subsequently a lower voltage V_0 is applied until time t_{tot} , after which the sequence is repeated. (c) A typical result measured for the 122 nm device with $V_0 = 0 \text{ V}$ and $V_1 = 5 \text{ V}$. The arrow indicates the peak time τ_p .

Large signal ($V_1 \gg V_0$) DI transients were measured for a broad range of final voltages (V_1 values in the range 2 to 12 V were used) for three available layer thicknesses. These layer thicknesses were: 67, 98, and 122 nm. A typical result, measured for the 122 nm thick device with $V_0 = 1.5 \text{ V}$ and $V_2 = 5 \text{ V}$, is shown in Figure 6.1(c). In order to investigate the precision of the experimental results, various consistency checks were performed. The value of the resistor was varied between 5 and 270 Ω . For the measurements shown, 100 Ω was chosen because in this case the interesting features such as the peak height and position are not affected whereas at the same time a sufficiently high signal-to-noise level was obtained. Furthermore it was found that the use of a low starting voltage, well below the approximately 1 - 1.5 V current onset voltage, gives rise to a varying peak position in time with varying t_{tot} . This is possibly caused by the time it takes for the charge carriers in the device to reach equilibrium. Especially if V_0 approaches 0, the capture and release of carriers to states that are low in energy is important. Carriers in such “deep trap states” take long to leave the material. If then the measured transient is obtained at comparable time-scales, the measurement can be influenced by the choice of t_{tot} . We found that with

$V_0 = 1.5$ V the transients show a good reproducibility. Therefore this value was set in the further experiments. It was also found that a reproducible and t_{tot} independent measurement could be done if $t_{\text{tot}} = 1$ s with a duty cycle of 1% was chosen. Therefore also these values were used in the further experiments. In order to further investigate the precision, the measured DI current densities (after about 1 s) were compared with independently measured steady-state current densities. In Figure 6.2 the consistency between both experiments is shown.

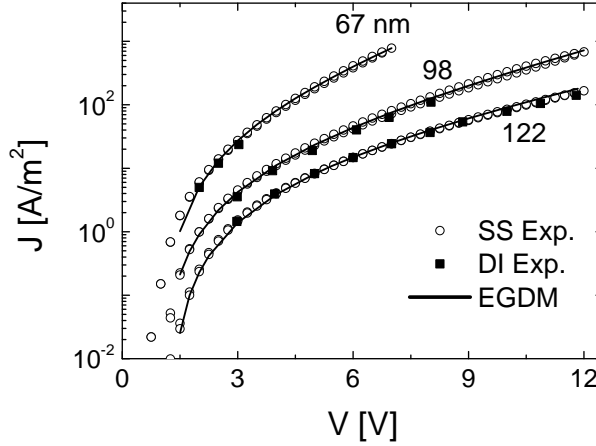


Figure 6.2: Experimental room-temperature steady-state current densities as a function of voltage obtained from the DI setup (filled squares) and a DC measurement (open circles). Data for the three different layer thicknesses studied (67, 98, and 122 nm) are shown. Also the best fit as obtained using parameter extraction (see Chapter 2) and the EGDM is shown (drawn curve).

The EGDM provides a good description to the measured characteristics as can be seen in Figure 6.2. The obtained materials and device parameters are very similar to the parameters obtained earlier in Ref. 8. In particular, a width of the DOS of 0.12 eV is obtained and a hopping site density of $4 \times 10^{26} \text{ m}^{-3}$ was found. The built-in voltages that optimally describe the characteristics were slightly different for each device and about 0.1 eV lower than in Ref. 8. This may be caused by a change of the metal-organic interface due to ageing. The obtained values of V_{bi} are 1.57, 1.54 and 1.80 V for the 67, 98, and 122 nm device, respectively. The optimized mobility μ_0 , which gives the zero field and carrier density limit of the EGDM mobility function, that describes the room temperature $J(V)$ characteristics shown in Figure 6.2, is equal to $(5 \pm 1) \cdot 10^{-12} \text{ m}^2/\text{Vs}$. The dielectric constant of the material was taken equal to 3.2, as in Ref. 8.

6.3 Modeling

A first simulation of the time-dependence of the current-density in organic semiconductors using the EGDM, which includes the effects of disorder, was given by Knapp *et al.*⁶ In their analysis also diffusion is taken into account. The time-dependent one-dimensional drift-diffusion equation is solved using a Scharfetter-Gummel discretization. However, no comparison with an experiment was made. In this work that step is made. We make use of an extension of a one-dimensional model based on the Master Equation (ME) for hopping transport, developed by Coehoorn and van Mensfoort *et al.*¹¹ Using the ME model, the time dependence of the current-density is calculated using the rate equations described in Ref. 11 and a sufficiently fine discretization of the time. To make the model applicable to the experiment, also the load resistance is included in a numerically exact way in the model. Figure 6.3 compares the modeled and experimental $J(t)$ curve measured in a device with a thickness of 122 nm.

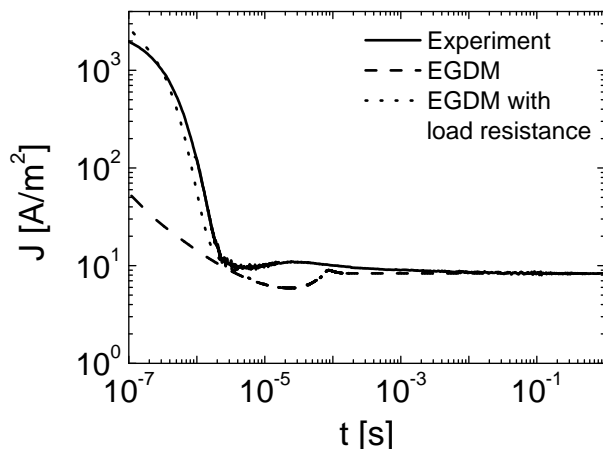


Figure 6.3: Measured (solid curve) and modeled (dashed curve) DI transients for the 122 nm thick device obtained using $V_0 = 1.5$ V, $V_1 = 5$ V and $R = 100$ Ω , at room temperature. The influence of including the load resistance in the model is shown by the dotted line which coincides with the dashed line after 10^{-5} s.

The solid curve shows the measured transient and the dotted and dashed curves give the modeled results with and without including the load resistance, respectively. A significantly improved description of the capacitive charging effect at the lower part of the time-scale can be seen if the load resistance is included in the model, viz. by calculating for each time-step the voltage drop across the load resistance and the diode under the constraint of an equal current density in each

of the two elements. The load resistance R was chosen at 100Ω such that it does not influence important features such as the peak position. This can be seen in Figure 6.3. As an alternative, Scott *et al.*¹² used a different setup in which the capacitive charging effect is suppressed, using a capacitance bridge. It is however not clear whether this method also affects the exact peak position and shape of the measured transient. Therefore it was chosen not to use this approach but to include the load resistance in the model.

6.4 Results and discussion

Figure 6.4 compares the experiments with the dark injection transients as predicted by the 1D-ME model. The modeled and measured transients go to the same steady state current-density at long time-scales (e.g. at 1 s). The DI peak time, which is due to the wavefront of carriers that have traveled through the device, moves to a lower value with increasing applied voltage. This is a direct result of the higher average velocity of the carriers at a higher voltage, due to the higher average field and the higher average mobility. The measured and modeled peak positions change similarly with increasing voltage. In Figure 6.5 this is visualized for the three different device thicknesses studied. Despite the good correspondence in the trend of the peak positions, there is a significant, quite systematic, difference in the values of the peak position. The experimental peak occurs about a factor of 3 earlier in time than the modelled peak. This indicates that something is missing in the description. Another difference between the measured and modeled transients is the time it takes after the peak has been obtained to reach the steady-state current-density. In the experiment this time is much longer, up to 0.1 - 1 s. Furthermore, the observed peak is in all cases broader than the predicted peak. This discrepancy between the experimental and the modeling result, which concerns also the peak width and peak tail length, is considered to be a consequence of a neglect of charge carrier relaxation in the modeling. Recently, Germs *et al.*¹³ have used a time-dependent mobility to take such relaxation effects into account in the low-frequency differential capacitance. A significantly higher mobility at the short time-scales after injection is found due to charge carrier relaxation processes. Such an increased mobility after injection was also reported by Devizis *et al.*¹⁴ The principle of charge carrier relaxation is shown in Figure 6.6. Carriers are injected at $t = 0$ s at the transport level, indicated by the bar, after which they relax to lower-energy states in the Gaussian DOS. The mobility of the carriers is initially high as compared to the equilibrium mobility, since the injected “hot” carriers are high in energy. Many other neighboring hopping sites are then energetically favorable to hop to. Hence a higher effective mobility is found just after injection. So far these effects have not yet been included in the model.

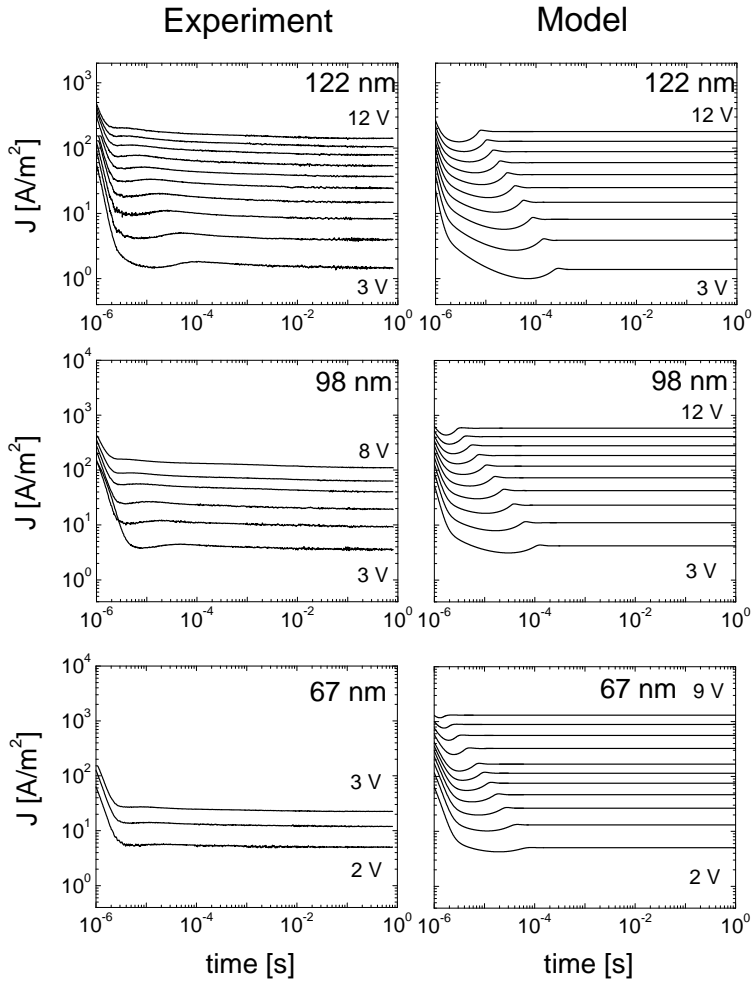


Figure 6.4: Measured and modeled DI transients at room temperature for the three PF-TAA based devices studied. A similar trend in the DI peak position can be observed; with increasing voltage, the peak occurs earlier in time due to the larger average field in the device.

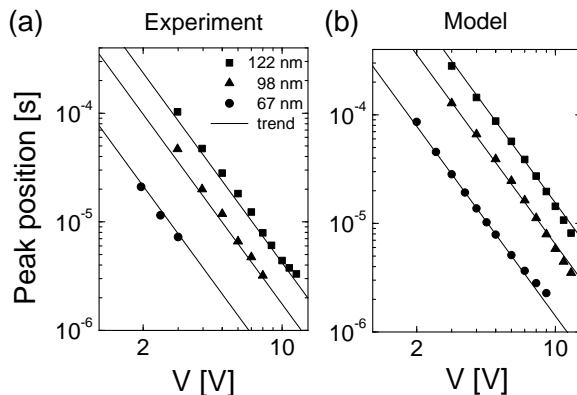


Figure 6.5: Experimental (a) and modeled (b) voltage dependence of the peak positions. For every thickness, a similar trend is observed. It can be seen however that the experimental peak position occurs about a factor of three earlier in time.

The inclusion of such effects could help to understand the difference in the observed peak-positions and peak shapes. Also, it may explain the longer times needed to reach steady-state observed in the experiment as compared to the model (see Figure 6.4). For PF-TAA, the time-dependent mobility, which results from charge carrier relaxation effects, is calculated using Monte Carlo simulations at various carrier concentrations c for a $\sigma/k_B T$ value of 5.1.¹³ A typical carrier concentration in the middle of the devices studied is 10^{-4} - 10^{-5} at 5 V. For these concentrations a strong time dependence of the mobility can be seen from Figure 6.7. This time-dependence of the carrier mobility due to relaxation will influence the measurement result and should be taken into account in the model to improve the description. Because the charge carrier relaxation process is sensitive to temperature, it is also valuable to study the temperature dependence of DI transients. So far, “large signal” DI transients have been studied. It would be valuable to study “small signal” DI transients. In such measurements $V_1 = V_0 + \Delta V$, with $\Delta V/V_0 \ll 1$, such that the experiment is much closer to the measurements of the steady-state $J(V, L, T)$ characteristics.

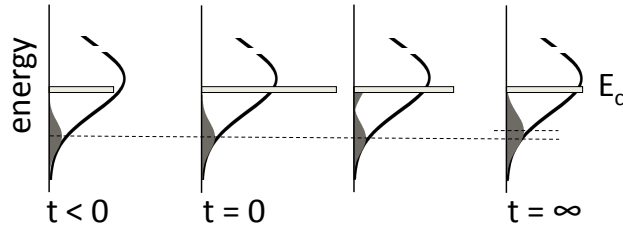


Figure 6.6: Visualization of the charge carrier relaxation process. At $t = 0$, charges are injected at the transport level, which is just below the top of the Gaussian DOS (bar). After this, the injected “hot” carriers relax to a lower equilibrium energy level (see figure at $t = \infty$).

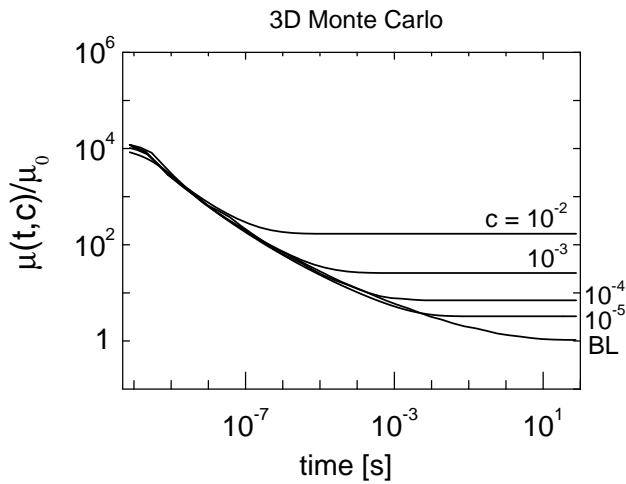


Figure 6.7: Normalized charge carrier mobility calculated using three-dimensional Monte Carlo simulations as a function of time. Various different values of the charge carrier concentration (c) in between the Boltzmann limit (BL) and $c = 10^{-2}$ are shown. A typical carrier concentration in the middle of the 122 nm thick OLED, studied at 5 V, is in the range 10^{-4} to 10^{-5} .¹⁵ The calculations are done at a $\sigma/k_B T$ value of 5.1, which is a realistic value for PF-TAA at room temperature.⁸

6.5 Conclusions and outlook

DI transients of PF based hole-only devices have been measured for three organic layer thicknesses. The accuracy of the measured transients was investigated by comparing the obtained values of the current-densities at 1 s with the independently measured steady state $J(V)$ characteristics. A good agreement was found. The materials and device parameters, which form the input for the EGDM, were determined from room temperature $J(V)$ curves and were consistent with the earlier work in Ref. 8. A simple analysis of the 122 nm transient measured at 5 V using Eq. 6.1 would give $\mu_{\text{DI}} = 7 \times 10^{-11} \text{ m}^2/\text{Vs}$. In contrast, an EGDM analysis of the same device yields $\mu_0 = 5 \times 10^{-12} \text{ m}^2/\text{Vs}$, and the actual mobility is a strong function of the carrier density and field. This explains why DI mobilities can be very different and clearly shows that DI transients cannot be used directly to measure the mobility function μ . The transients have been modeled using a 1D ME approach and the EGDM, which include the effects of energetic disorder and diffusion. The load resistance, which is a part of the experimental set-up, was included in the model. The trend in the measured voltage dependence of the “transit time” peak position is essentially the same as that obtained from the model. However, although diffusion and energetic disorder are now included, the experimental results show a broader peak and a longer time is required to reach steady state. Furthermore, experimentally the peak is observed about a factor of three earlier in time. These differences may be due to charge carrier relaxation effects. This process leads to a higher effective mobility of carriers just after injection. It would be valuable to include these effects in an improved model. The effect of relaxation is already of importance for hole-only devices, as studied in this chapter. However, it is expected to be even more important for electron-only devices, in which the presence of an additional trap density of states is expected to make relaxation effects even more important. A clear indication is the frequently observed occurrence of history-dependent hysteresis effects in the $J(V)$ curves of electron-only devices.

Bibliography

1. P. M. Borsenberger, R. Richert, and H. Bässler, *Phys. Rev. B* **47**, 4289 (1993).
2. P. M. Borsenberger, L. T. Pautmeier, and H. Bässler, *Phys. Rev. B* **48**, 3066 (1993).
3. A. Many and G. Rakavy, *Phys. Rev.* **126**, 1980 (1962).
4. D. Poplavskyy, W. Su, F. Pschenitzka, and F. So, *Proc. SPIE* **5519**, 110 (2004).
5. D. Poplavskyy, W. Su, and F. So, *J. Appl. Phys.* **98**, 014501 (2005).
6. E. Knapp and B. Ruhstaller *10th Conference on Numerical Simulation of Optoelectronic Devices (NUSOD)* **126**, 35-6 (2010).
7. W. F. Pasveer, J. Cottaar, C. Tanase, R. Coehoorn, P. A. Bobbert, P. W. M. Blom, and D. M. de Leeuw *Phys. Rev. Lett.* **94**, 206601 (2005).
8. S. L. M. van Mensfoort, S. I. E. Vulto, R. A. J. Janssen, and R. Coehoorn, *Phys. Rev. B* **78**, 085208 (2008).
9. R. J. de Vries, S. L. M. van Mensfoort, R. A. J. Janssen, and R. Coehoorn, *Phys. Rev. B* **81**, 125203 (2010).
10. S. L. M. van Mensfoort and R. Coehoorn, *Phys. Rev Lett.* **100**, 086802 (2008).
11. R. Coehoorn and S. L. M. van Mensfoort, *Phys. Rev. B* **80**, 085302 (2009).
12. J. C. Scott, S. Ramos, and G. G. Malliaras, *J. Imaging Sci. Tech.* **43**, 233 (1999).
13. W. Chr. Germs, J. J. M. van der Holst, S. L. M. van Mensfoort, P. A. Bobbert, and R. Coehoorn, *Phys. Rev. B* **84**, 165210 (2011).
14. A. Devizis, K. Meerholz, D. Hertel, and V. Gulbinas, *Phys. Rev. B* **82**, 155204 (2010).
15. R. J. de Vries, S. L. M. van Mensfoort, V. Shabro, S. I. E. Vulto, R. A. J. Janssen, and R. Coehoorn, *Appl. Phys. Lett.* **94**, 163307 (2009).

A device model for multilayer white OLEDs

The overall goal of the research presented in this thesis has been to develop methods that contribute to making it feasible to rationally design OLEDs on the basis of device modeling. Since the first device models introduced in the 1990s,¹⁻⁴ considerable progress has been made.⁵⁻⁷ For example, van Mensfoort et al.⁸ have shown how the disordered nature of the organic semiconductors can be included, so that predictive device modeling is possible for single layer OLEDs. In this Chapter, further steps towards realizing predictive device modeling for a realistic white multilayer OLED are presented. The system studied is a hybrid OLED, containing fluorescent blue and phosphorescent green and red layers, investigated within the European project AEVIOM. It is first shown how the method on parameter extraction from Chapter 2 is used to determine the electron mobility in the small-molecule material NET-5 which forms the electron transport layer. Also modeling results on the blue-emitting Spiro-DPVBi layer are described. In the AEVIOM project this knowledge has formed the input for a three-dimensional Monte Carlo simulation of the full multilayer hybrid white OLED. The model is based on physically interpretable parameters related to the molecular structure of the materials used. We present a first comparison between the measured and modeled current-density versus voltage characteristics. This shows that it is now possible to make such a comparison based on experimental knowledge on the mobility in the layers used. As a next step it is worth investigating which device parameters most strongly influence the current-density and the device efficiency. Is this for example a specific interface barrier or the electron or hole mobility in a certain layer? A device model can be used to find the critical parameters which may subsequently be used for a rational stack design for improving the efficiency.

7.1 Introduction

Multilayer white OLEDs are interesting candidates for lighting applications.^{9–11} The rational design of such an OLED is hampered by the lack of a device model which consistently includes the effects of the disordered nature of the organic semiconducting layers and takes the interfaces into account. In this Chapter, contributions to the development of such a multilayer model for the white OLED depicted in Figure 7.1 are described. The functioning of the stack and the materials used are described in Chapter 1. Figure 7.1(b) shows the energy levels of the highest occupied molecular orbital (HOMO) and lowest unoccupied molecular orbital (LUMO) of the materials used in the stack.¹²

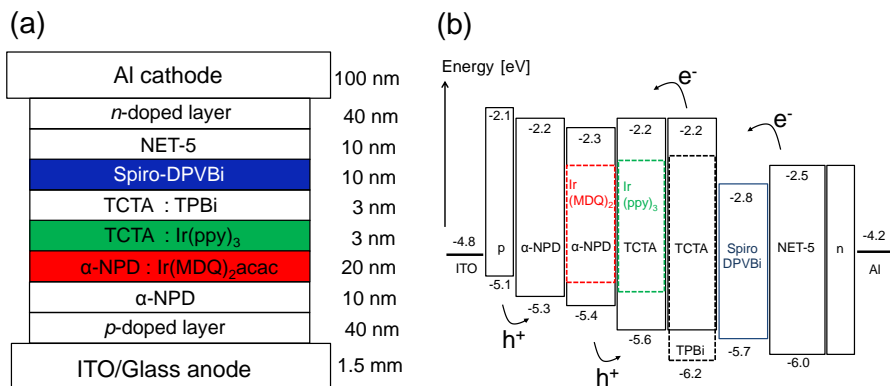


Figure 7.1: Layer structure (a) and energy level diagram (b) of the multilayer white OLED studied in this chapter. The stack consists of various evaporation deposited small-molecule based organic layers in between a transparent ITO anode and an Al cathode, as earlier introduced in Chapter 1.

Now the question arises whether it is possible to efficiently and accurately determine the mobility function in each layer. For holes this was found to be possible in α -NPD by using the ECDM.¹³ The determination of the mobility function is potentially harder for the case of electrons, as shown in Chapter 2 and 5. We use symmetric devices with doped injection layers as an effective electrode material to reduce the amount of parameters in the determination of the mobility by modeling.¹⁴ Section 7.2 of this chapter gives a modeling study on the electron transport of a Novaled Electron Transport (NET-5) layer in between n -doped NET-5 layers.¹⁵ In Section 7.3, electron transport in the blue-emitting small-molecule material Spiro-DPVBi is experimentally studied. Subsequently, in Section 7.4 the results of a calculation of the current-density using a three-dimensional Monte Carlo model is shown, carried out in the group Theory of Polymers and Soft Matter at the Eindhoven University of Technology.¹⁶ This

simulation is based on the mobility obtained from studies of the hole and electron transport in the layers used, including the study of the electron transport current-density versus voltage ($J(V)$) characteristics of NET-5 and Spiro-DPVBi discussed in this chapter. We show that it is now possible to develop an OLED device model based on experimental data, opening the prospect that it will be possible to develop a simulation tool which supports the rational design of white OLED multilayer stacks.

7.2 Electron transport in NET-5

Electron transport in rather simple electrically symmetric devices based on the small-molecule material NET-5 in between approximately 50 nm thick n -doped NET-5 layers was studied. The goal of this new approach was to determine the electron mobility function as input for a multilayer device simulation. Also the question whether the transport in this material is described best using either the EGDM or the ECDM, which is based on correlations between the hopping sites due to dipolar disorder, is addressed. The complete device structure is:

$$| \text{ITO} | n\text{-doped NET-5} | \text{NET-5} (L) | n\text{-doped NET-5} | \text{Al} |.$$

The measured $J(V)$ curves are shown in Figure 7.2. As expected from the symmetric device structure, symmetric $J(V)$ characteristics are measured for all three NET-5 layer thicknesses (L). The DC measurements (solid lines) in the figure are measured in voltage steps of 0.1 V at time intervals of 1 s. Carrying out DC measurements at currents above ~ 100 A/m² led to heating of the sample. Therefore, pulsed measurements (dashed lines) were carried out at 1 Hz with a duty cycle of 1%. These pulsed measurement settings were found to lead to a curve which is well connected to the measured DC curve. The doped injection layers¹⁷ used have a high conductivity, so that there is expectedly no or only a small voltage drop across these layers. This makes it possible to study the mobility in the bulk of NET-5 by analyzing the $J(V, L, T)$ characteristics using the device models introduced in Chapter 1.

The nominal layer thicknesses of the NET-5 layer were 100, 150 and 200 nm. Often, the actual thickness is somewhat different, due to a change over time of the deposition rate resulting from a given setting of the deposition conditions. The real thicknesses of the NET-5 layers were determined using two techniques. Transmission Electron Microscopy (TEM) images of the cross section of the devices were made to obtain the thickness of the organic part of the devices. No distinction could be made between the n -doped NET-5 and the pure NET-5 layer based on the TEM images. Therefore additional X-ray Photoelectron Spectroscopy (XPS) experiments were done with which a concentration profile was made of the elements present in the layers. The measurements were carried out in a Quantera SXM from Ulvac-PHI. The depth profiles were measured by alternating XPS measurements and sputtering with Ar⁺-ions. Since the sputtering rate in the organic layers is not known, the total thickness obtained using TEM was used to calibrate the XPS profile.

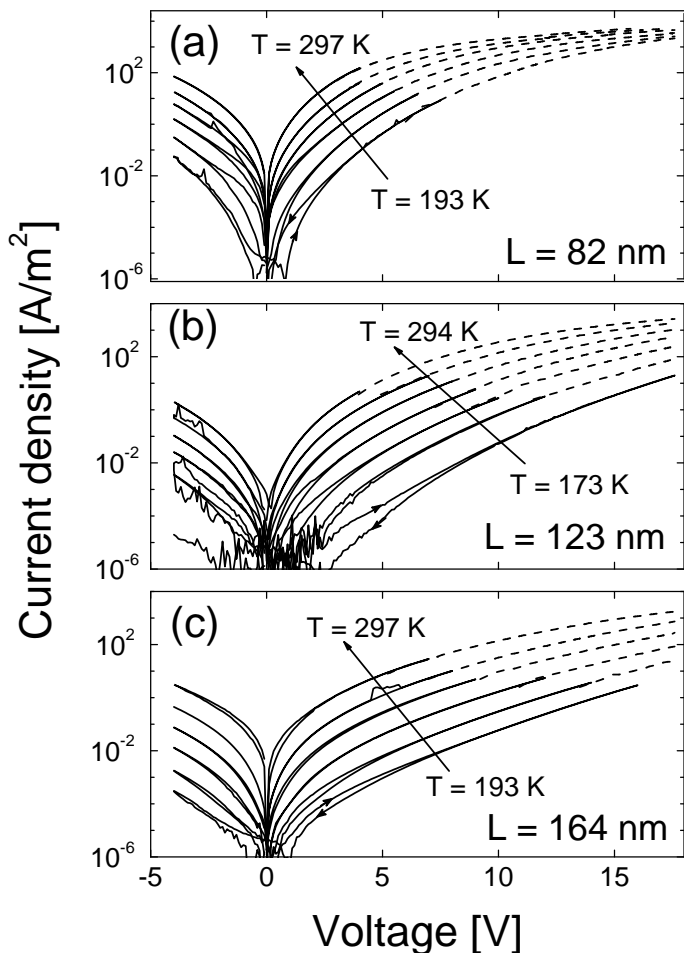


Figure 7.2: Measured $J(V)$ characteristics of devices based on NET-5, for three layer thicknesses. The solid lines give the DC measurement results and the dashed lines show the results of pulsed measurements. More specifically for the 82 nm device curves were measured at 193, 213, 233, 253, 272, and 297 K. For the 123 nm device at 193, 213, 233, 253, 273, and 294 K, and for the 164 nm device at 193, 213, 233, 253, 273, and 297 K. The arrows indicate the curves resulting from an upward and downward voltage sweep. Some hysteresis is observed at small voltages.

From this data, the n -doped layer could be distinguished from the pure NET-5 layer. As an example, the total thickness of the organic part of a NET-5 based device turned out to be 195 nm using TEM. Subsequently, the XPS measurements showed that the n -doped layers in this material had a thickness of 36 nm. This gives a total NET-5 thickness of 123 nm ($195-2\times 36$). The obtained NET-5 thicknesses of the other two devices studied were found to be 82 and 164 nm, respectively.

7.2.1 EGDM results

It was first investigated to what extent the EGDM can be used to describe the measured $J(V)$ characteristics. Within the analysis a single set of fit parameters was used, and the fitting was carried out using the “grid approach”, as also used in Chapter 5. The n -doped layers were treated as metallic contacts, with a Fermi level coinciding with the LUMO of the NET-5 (no injection barrier). Figure 7.3 shows the modeling results and reveals that a rather good fit was obtained.

Table 7.1 (first column) shows the obtained best fit parameters using the EGDM.

Table 7.1: Best fit EGDM and ECDM materials and device parameters obtained using, for the EGDM, a “grid approach” and for the ECDM the parameter extraction procedure presented in Chapter 2. The asterisk indicates that for the ECDM the value of N_t was kept fixed.

Parameter	EGDM	ECDM
N_t [10^{27} m^{-3}]	0.2	1*
σ [eV]	0.11	0.12
$N_{t,\text{trap}}$ [10^{24} m^{-3}]	5	1.8
T_0 [K]	1400	1670
C	0.47 ± 0.02	0.44 ± 0.03
μ_0^* [$10^{-7} \text{ m}^2\text{V}^{-1}\text{s}^{-1}$]	$10^{0.5\pm 0.5}$	$10^{-0.2\pm 0.5}$

The best fit hopping site density from the modeling is about a factor of five lower than the expected molecular NET-5 density. This indicates that the modeling is not fully consistent. The other parameters obtained using the EGDM are in the expected range. For instance the C -parameter is found to be equal to 0.47 ± 0.02 which is within the range 0.4–0.5 expected for the EGDM. Furthermore, the width of the density of states has a value which is typical for organic materials. However, similar to the work on Alq_3 presented in Chapter 5, a thickness dependence of the mobility in the limit of zero field and electron density, $\mu_0(T)$, was found. This result is shown in Figure 7.4 and indicates that the modeling is not fully consistent.

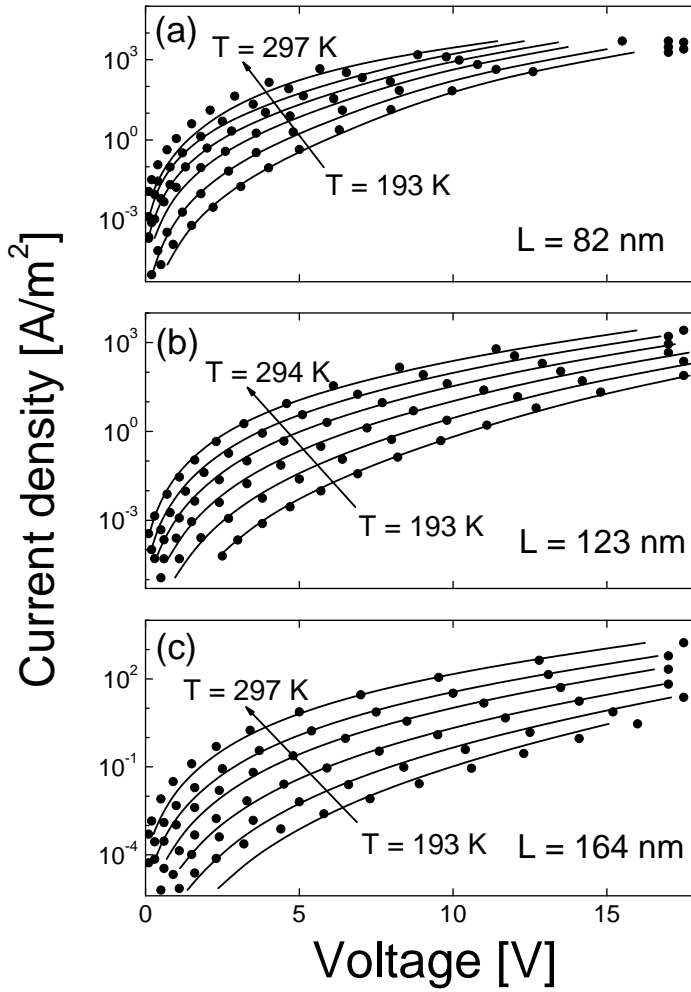


Figure 7.3: EGDM fit (drawn curves) to the measured (\bullet) $J(V)$ characteristics using a single set of materials and device parameters.

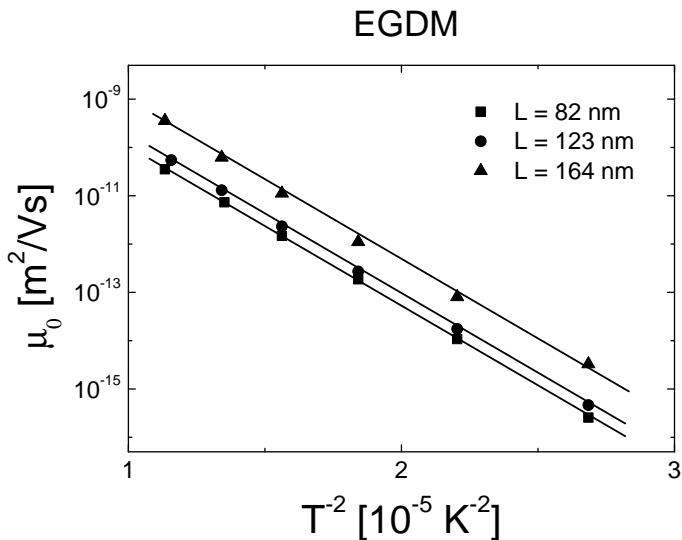


Figure 7.4: Temperature dependence of μ_0 obtained using the EGDM for the different NET-5 layer thicknesses studied.

In Chapter 2 it was shown that typically the ECDM yields a higher hopping site density than the EGDM.^{13,18–20} This leads to the question whether the ECDM can give an equally good or even better description to the NET-5 characteristics, with a more realistic site density.

7.2.2 ECDM results

Using a fixed realistic site density N_t of $1 \times 10^{27} \text{ m}^{-3}$, the ECDM was used to obtain the other fit parameters to the experimental data. The resulting $J(V)$ curves are shown in Figure 7.5, and the fit parameters are shown in Table 7.1. They were determined using the extraction method described in Chapter 2.

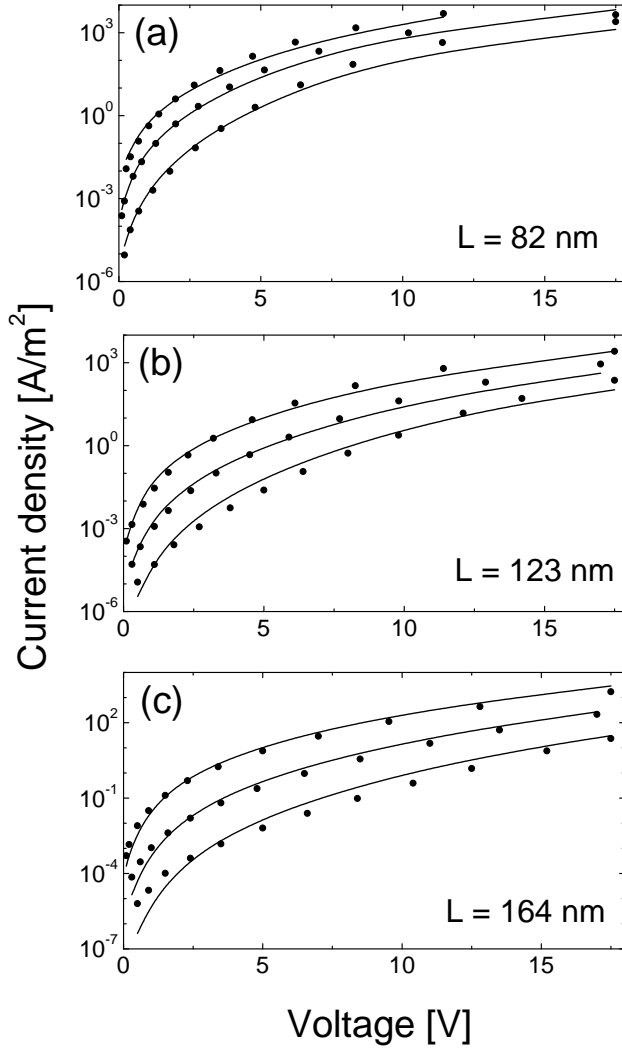


Figure 7.5: ECDM fit (solid lines) to the measured (\bullet) characteristics using a realistic site density.

For the extraction, curves measured at 294, 253 and 213 K were used as obtained from devices with a thickness of 82 and 123 nm. Subsequently, the obtained parameters were used to fit the data measured at the same temperatures for the device with a thickness of 164 nm. In this fit, the mobility μ_0 was left free for every curve studied. The fit results are rather good, as can be seen in Figure 7.5.

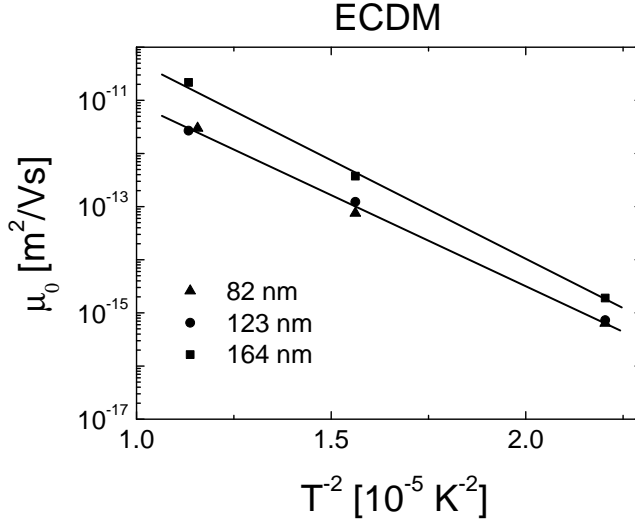


Figure 7.6: Temperature dependence of μ_0 obtained using the ECDM and using the parameter extraction method described in Chapter 2. The upper line shows a guide-to-the-eye to the data obtained for the 164 nm thick device. The lower line is related to the two thinner devices.

Figure 7.6 shows the obtained temperature dependence of μ_0 . A slope parameter C equal to 0.44 ± 0.03 is obtained, which is relatively high for the ECDM, when Miller Abrahams hopping is assumed. However, recent work of Cottaar *et al.*²¹ shows that within Marcus-theory the C -parameter a value of 0.44 can be realistic for the case of correlated disorder. Furthermore a spread of about one order of magnitude at room temperature in the obtained μ_0 value is found. This shows the modeling is, again, not fully consistent. As described in Chapter 5 such an unexpected thickness dependence of μ_0 can be caused by an interface effect. Alternatively, the n -doped injection layers may lead to a series resistance which influences the analysis. To investigate this, the $J(V)$ characteristics of a 100 nm thick n -doped layer in between ITO and Al were studied. At room temperature, a symmetric linear (Ohmic) $J(V)$ curve was measured with a high conductivity. Already at 2 V a current-density of 1500 A/m² was measured. In the 100 nm thick NET-5 based device studied in this section this current-density is reached at

about 9 V. With decreasing temperature, the conductivity of the n -doped layer is found to decrease much less quickly than the conductivity of the NET-5 based devices. Therefore the voltage drop over the n -doped layer is largest at room temperature. A more complete model should include the transport through and the injection from these layers. Such a model should also take the molecular level structure of the host guest materials in the n -doped layer, and the effect on the injection, into account (see Figure 7.7).

In summary, we find that good fits to the experimental data can be obtained using the ECDM and the EGDM. However, the temperature dependence of the mobility μ_0 leads for both models to an inconsistent result. At every temperature a thickness dependent μ_0 value is obtained. Therefore we consider it at this stage not possible to conclude on the question whether the ECDM or the EGDM is more applicable to describe the measured NET-5 characteristics.

7.3 Electron transport in Spiro-DPVBi

In a similar device architecture, the small-molecule material Spiro-DPVBi was studied. In Chapter 1 the molecular structure of Spiro-DPVBi was shown. Devices with the structure:

$$| \text{ITO} | n\text{-doped NET-5} | \text{Spiro-DPVBi} (L) | n\text{-doped NET-5} | \text{Al} |,$$

were made with nominal thicknesses of $L = 100, 150,$ and 200 nm. A possible deviation of the actual thickness of the layers was not investigated. A schematic energy level diagram is shown in Figure 7.7, in which the dashed lines show the HOMO and LUMO level of the dopants used in the n -doped layer. The measured current-density versus voltage characteristics are shown in Figure 7.8. Similar to the case of NET-5, symmetric curves were obtained as expected.

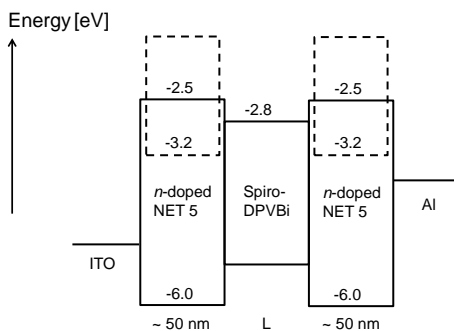


Figure 7.7: Schematic energy level diagram of the studied Spiro-DPVBi based devices. The LUMO level of Spiro-DPVBi is at -2.8 eV. The HOMO level of the dopant (dashed) and the LUMO level of the NET-5 are at -3.2 and -2.5 eV, respectively.¹²

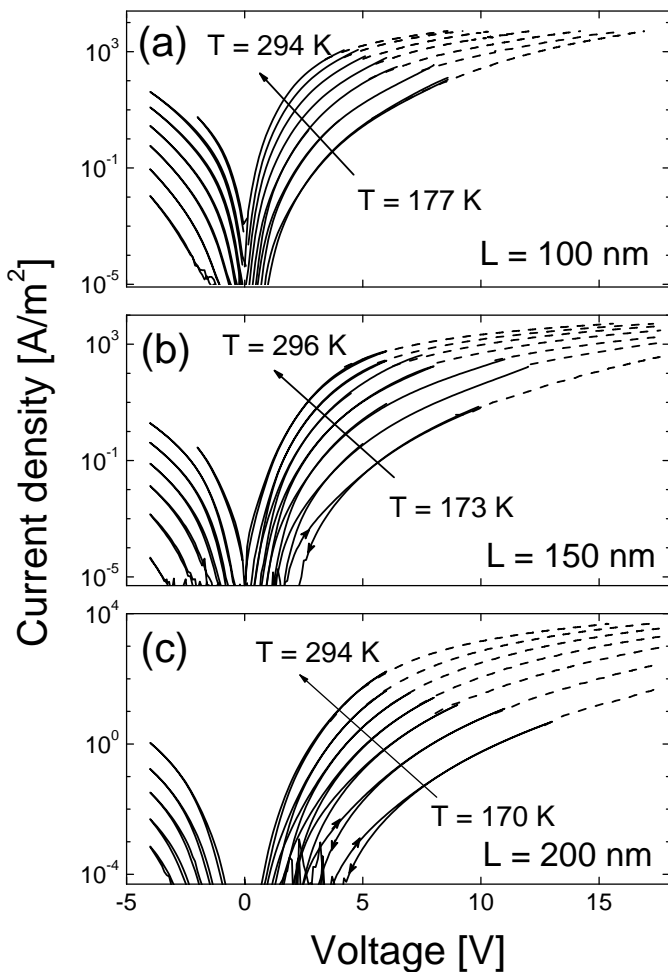


Figure 7.8: Measured current-density versus voltage characteristics of Spiro-DPVBi based devices with a nominal layer thickness of 100, 150 and 200 nm. The solid lines show the results of the DC measurements and the dashed lines show the pulsed measurement results. For the 100 nm thick device the curves were measured at 294, 273, 253, 233, 213, 193, and 177 K, for the 150 nm device at 296, 273, 253, 233, 213, 193, and 174 K, and for the 200 nm thick device at 294, 273, 253, 233, 213, 193, and 170 K.

From the energy levels an injection barrier is expected at the interface with the n -doped layer. From a modeling study using the EGDM without an interface barrier, no consistent description of the characteristics could be obtained. In particular, from a fit to the curves obtained for $V > 0$ V a built-in voltage of about 2 V was obtained for the 200 nm device. This is unexpected for these symmetric devices. It should be noted that since Spiro-DPVBi is found to be a better conductor than NET-5, an even higher voltage drop over the n -doped NET-5 based injection layer is expected. To be more specific, in the Spiro-DPVBi based device of 100 nm, a current-density of 1500 A/m^2 is found at 4.3 V. For that current-density a voltage drop of about 2 V over the n -doped layers is expected based on the measurements on the n -doped layer in between ITO and Al. A complete model thus requires the inclusion of the injection layers. Moreover a thickness dependent mobility μ_0 is obtained, which points at an inconsistency in the model. In Chapter 5 it was concluded that such a thickness dependence can point at the presence of an injection barrier at the interface of, in this case, Spiro-DPVBi and the n -doped NET-5 layer. From the experimentally determined LUMO levels of Spiro-DPVBi and the n -doped NET-5 layer an injection barrier is expected. The exact size of this barrier is hard to deduce from these numbers due to the rather large experimental uncertainty in the value of the energy levels, and due to the fact that the n -doped layer consists of two materials, as shown in Figure 7.7, which expectedly both contribute to the injection into the Spiro-DPVBi layer. The series resistance across the n -doped layers can also contribute to an apparent layer thickness dependence of μ_0 , if this effect is neglected in the analysis.

Instead of carrying out such a refined analysis, which we regard as a future project, we used the experimental data to obtain a description of the mobility function with an accuracy that is expected to be sufficiently fair as an input for the Monte Carlo calculation presented in Section 7.4. For that purpose, the ECDM is used with a $\Delta = 0.5$ eV injection barrier, together with the parameter extraction method developed in Chapter 2. This value of the injection barrier was chosen on the basis of the following considerations. In equilibrium the Fermi energy in the doped NET-5 layer is expected to be more close to the HOMO energy of the dopant than to the LUMO energy of the host. Its detailed position depends on the shapes of both densities of states, and on the dopant concentration. From Figure 7.7 an injection barrier $\Delta = 0.4$ eV or slightly smaller would be expected. However, it is quite likely that under realistic bias conditions the n -doped layer does not act as an ideal metal and the electron density at the interface would be even smaller than as expected for such a barrier. Therefore a slightly higher value of $\Delta = 0.5$ eV was chosen. The extraction is based on the room temperature $J(V)$ characteristics of the 100 and 200 nm devices. The extraction assumes a realistic site density $N_t = 1 \times 10^{27} \text{ m}^{-3}$ and width of the density of states $\sigma = 0.1$ eV, as these parameters were taken to be fixed (for all layers) in the Monte Carlo study. Furthermore, a fixed trap density $N_{t,\text{trap}} = 1 \times 10^{24} \text{ m}^{-3}$ was used. The fit yielded a trap temperature T_0 equal to 2350 K and a mobility μ_0 equal to $1 \times 10^{-10} \text{ m}^2 \text{V}^{-1} \text{s}^{-1}$. These results were used as input for the multilayer MC simulation presented in Section 7.4.

7.4 Monte Carlo simulation of a multilayer stack

The increased calculation speed of modern computer systems makes it now possible to perform three-dimensional Monte Carlo (MC) simulations of the multilayer OLED presented in Figure 7.1. In such a simulation, physical parameters related to the molecular structure such as the width of the density of states and the site density are used. In the case of electron transport also the traps can be taken into account. Within the AEVIOM project the group Theory of Polymers and Soft Matter at the Eindhoven University of Technology performed such a multilayer device simulation based on a fixed realistic intersite distance of 1 nm and a width of the density of states σ of 0.1 eV for every layer in the stack.¹⁶ From previous work, it follows that small-molecule based materials are typically described best using the ECDM.^{13,20} For that reason the MC simulation was carried out assuming correlated disorder. The energy levels shown in Figure 7.1 were assumed. It should be noted that a rather large relative uncertainty of about 0.2 eV (or in some cases even more), is present in these numbers. Furthermore, for all layers which contain α -NPD a hole mobility μ_0 equal to $6 \times 10^{-9} \text{ m}^2\text{V}^{-1}\text{s}^{-1}$ was chosen.¹³ The electron mobility, which is not critical in these hole transport layers, is taken a factor of 10 lower. The layers which contain TCTA were given a hole mobility μ_0 value of $2 \times 10^{-8} \text{ m}^2\text{V}^{-1}\text{s}^{-1}$, which follows from Ref. 23. Again the electron mobility is expectedly not critical and is chosen a factor of 10 lower. The description of the electron transport in Spiro-DPVBi and NET-5, used in the MC calculation was derived from our experimental studies. For the case of Spiro-DPVBi, the MC calculations were performed using $\mu_0 = 8 \times 10^{-9} \text{ m}^2\text{V}^{-1}\text{s}^{-1}$, $T_0 = 2350 \text{ K}$ and $N_{\text{t,trap}} = 1 \times 10^{23} \text{ m}^{-3}$, as explained in Section 7.3. A similar ECDM analysis led for NET-5 to $\mu_0 = 1 \times 10^{-10} \text{ m}^2\text{V}^{-1}\text{s}^{-1}$, $T_0 = 1400 \text{ K}$ and $N_{\text{t,trap}} = 5 \times 10^{24} \text{ m}^{-3}$. For the hole mobility in Spiro-DPVBi and NET-5, which are both non-critical, a value equal to that in α -NPD $6 \times 10^{-9} \text{ m}^2\text{V}^{-1}\text{s}^{-1}$ and $1 \times 10^{-11} \text{ m}^2\text{V}^{-1}\text{s}^{-1}$ were chosen, respectively. It should be noted that, for the case of electron transport, a precise determination of the density of states parameters and mobility μ_0 is not easy, as discussed in Chapter 2. This causes a relatively large uncertainty in the parameters obtained. An additional potential inaccuracy is obtained by fixing the values of σ and N_{t} , instead of leaving them as a layer-specific free parameter. This was done for technical reasons related to the MC simulation code. Nevertheless, we expect that the approximate approach used leads to a useful first view on the functioning of the hybrid white AEVIOM stack.

Figure 7.9 shows the result of a stack simulation using the mentioned experimental input on the description of the DOS and of μ_0 in each layer.²⁴ The stack is modeled using a cubic lattice of $56 \times 50 \times 50$ sites with periodic boundary conditions in the y - and z -direction (56 is the total number of organic layers in the x -direction). The time-averaged occurrence of recombination events at 7 V is indicated in Figure 7.9(a) by the red, green and blue spheres, whereas the purple and yellow spheres represent the electrons and holes, respectively. The radius of the red, green and blue spheres are a measure for the number of recombination events. Figure 7.9(b) shows the calculated $J(V)$ characteristic (drawn curve). For comparison, also the measured (open symbols) $J(V)$ characteristic is given. It can be seen that the measured and modeled $J(V)$ curve are quite similar.

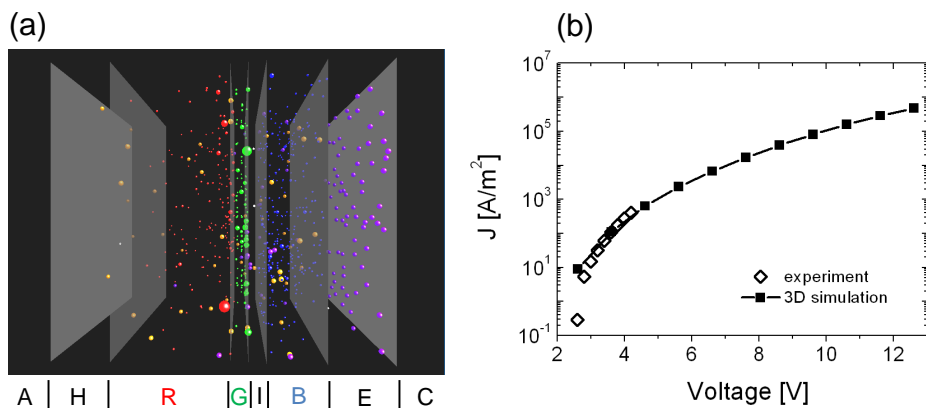


Figure 7.9: Three-dimensional Monte Carlo simulation of the multilayer white OLED shown in Figure 7.1. (a) Visualization of the recombination of electrons and holes (purple and yellow spheres, respectively) to red, green and blue photons (time-averaged probability of recombination events). The letters A, H, R, G, I, B, E, and C indicate the anode, hole transport layer, red-emitting layer, green-emitting layer, interlayer, blue-emitting layer, electron transport layers and the cathode, respectively. (b) Measured (open symbols) and modeled (drawn curve) $J(V)$ characteristic.

In conclusion, these results show that it is now technically possible to do such a simulation and to compare with a measured result, which makes experimental validation possible. Therefore the rational design of OLEDs which may be realized based on a device model with a predictive value is one step closer. It is now for instance possible to investigate which mobility, layer thickness or interface barrier is most critical for the eventual device efficiency. Despite the fact that the multilayer model presented contains many numbers with large uncertainties such as on the mobilities, energy barriers and layer thicknesses which may be improved by more in-depth studies, the model makes it now for the first time possible to perform scenario studies which contribute to rational stack design.

Bibliography

1. J. Staudigel, M. Stossel, F. Steuber, J. Simmerer, *J. Appl. Phys.* **86**, 3895 (1999).
2. P. W. M. Blom, M. J. M. de Jong, and S. Breedijk, *Appl. Phys. Lett.* **71**, 930 (1997); P. W. M. Blom and M. C. J. M. Vissenberg, *Mat. Sci. Eng.* **27**, 53 (2000).
3. G. G. Malliaras and J. C. Scott, *J. Appl. Phys.* **83**, 5399 (1998); G. G. Malliaras and J. C. Scott, *J. Appl. Phys.* **85**, 7426 (1999)
4. B. K. Crone, P. S. Davids, I. H. Campbell, and D. K. Smith, *J. Appl. Phys.* **84** 833 (1998); P. S. Davids, I. H. Campbell, and D. L. Smith, *J. Appl. Phys.* **82**, 6319 (1997); S. J. Konezny, D. L. Smith, M. E. Galvin, and L. J. Rothberg, *J. Appl. Phys.* **99**, 064509 (2006).
5. B. Ruhstaller, S. A. Carter, S. Barth, H. Riel, W. Riess, J. C. Scott, *J. Appl. Phys.* **89**, 4575 (2001).
6. W. F. Pasveer, J. Cottaar, C. Tanase, R. Coehoorn, P. A. Bobbert, P. W. M. Blom, and D. M. de Leeuw *Phys. Rev. Lett.* **94**, 206601 (2005).
7. M. Bouhassoune, S. L. M. van Mensfoort, P. A. Bobbert, and R. Coehoorn *Org. Electron.* **10**, 437 (2009).
8. S. L. M. van Mensfoort, J. Billen, M. Carvelli, S. I. E. Vulto, R. A. J. Janssen and R. Coehoorn, *J. Appl. Phys.* **109**, 064502 (2011).
9. B. W. D'Andrade and S. R. Forrest, *Adv. Mat.* **16** 1585 (2004).
10. G. Schwartz, K. Fehse, M. Pfeiffer, K. Walzer and K. Leo, *Appl. Phys. Lett.* **89**, 083509 (2006).
11. S. Reineke, F. Lindler, G. Schwartz, N. Seidler, K. Walzer, B. Lussem and K. Leo, *Nature* **459**, 234 (2009).
12. Within the AEVIOM project the LUMO levels were obtained using ultra violet photoelectron spectroscopy (UPS) and cyclic voltammetry. More specifically, UPS is used to determine the HOMO level and by adding an optical gap the LUMO level is obtained. One may argue that also an exciton binding energy should be added but this was not done.
13. S. L. M. van Mensfoort, V. Shabro, R. J. de Vries, R. A. J. Janssen and R. Coehoorn *J. Appl. Phys.* **107**, 113710 (2010).
14. M. Schober, S. Olthof, M. Furno, B. Lüssem, and K. Leo, *Appl. Phys. Lett.* **97**, 013303 (2010).
15. Novaled AG is a well-known supplier of organic materials for OLED applications (<http://www.novaled.com/>).

16. The Monte Carlo simulations were done by Jeroen Cottaar, Murat Mesta, Jeroen van de Holst, Frank van Oost en dr. Peter Bobbert at the Eindhoven University of Technology.
17. K. Walzer, B. Meannig, M. Pfeiffer and K. Leo, *Chem. Rev.* **107**, 1233 (2007).
18. S. L. M. van Mensfoort, S. I. E. Vulto, R. A. J. Janssen and R. Coehoorn, *Phys. Rev. B* **78**, 085208 (2008)
19. R. J. de Vries, S. L. M. van Mensfoort, V. Shabro, S. I. E. Vulto, R. A. J. Janssen, and R. Coehoorn, *Appl. Phys. Lett.* **94**, 163307 (2009).
20. S. L. M. van Mensfoort, R. J. de Vries, V. Shabro, C. van der Marel, H. P. Loebel, R. A. J. Janssen, and R. Coehoorn, *Org. Electron.* **11**, 1408 (2010).
21. J. Cottaar, R. Coehoorn, and P. A. Bobbert, unpublished.
22. O. Li, C. H. Kim, Z. Zhou, J. Shinar, and K. Okumoto, *Appl. Phys. Lett.* **88**, 253505 (2006).
23. S. Noh, C. K. Suman, Y. Hong, and C. Lee, *J. Appl. Phys.* **105**, 033709 (2009).
24. F. W. A. van Oost and P. A. Bobbert, “Visualisation of a 3D Monte Carlo simulation in a 3 layer OLED”, <http://www.youtube.com/watch?v=HVMQtyT0jWQ>

Summary

Development of a charge transport model for white organic light-emitting diodes (OLEDs)

Organic light-emitting diodes (OLEDs) are promising candidates for future **lighting applications** since they can be made ultra-thin, color-tunable and flexible. Improving their efficiency is an important challenge in the field of organic electronics. The availability of a device model can make the **rational design** of more efficient devices possible. State-of-the-art models give insights on processes at the molecular scale, for instance by yielding physically interpretable parameters. This brings the molecular-scale design of more suitable materials one step closer. In this thesis, crucial elements towards the development of a **multilayer white OLED model** are presented.

The white OLEDs on which this study finally focusses are introduced in Chapter 1. They contain evaporation deposited electron and hole transport layers but also a blue-emitting fluorescent layer and red- and green-emitting phosphorescent layers. An overview is given of how one can analyze current-density (J) versus voltage (V) characteristics of single layer devices. Also the recently developed “**extended Gaussian disorder model**” (EGDM) and the “**extended correlated disorder model**” (ECDM) are introduced. In this thesis, these models are used to analyze the measured electrical characteristics of various small-molecule based single-layer devices. This was done to explore the necessary steps towards multilayer device modeling, and to obtain the charge carrier mobility in the layers. In addition, single layer polymer devices are investigated in order to develop and validate additional methods for studying the charge transport in disordered organic semiconductors. The interpretation of the characteristics is found to require detailed knowledge of the materials and the interfaces. Several parameters must be determined to achieve an accurate description.

Firstly, this led to the question how accurately materials parameters which determine the **mobility** can be determined based on $J(V)$ characteristics of single layer devices. In Chapter 2, an extraction method based on a Gauss-Newton algorithm is developed and thoroughly tested on both hole-only and electron-only characteristics to investigate the **accuracy** but also the **limitations** of parameter extraction. It is concluded that for hole transport the extraction is straightforward, in contrast to the case of electron transport where the extraction often requires additional knowledge about the system.

Obviously, if one could use an **independent experimental technique** to determine one of the parameters involved this would improve the accuracy of

electrical characterization. One of the important parameters in single layer devices is the **built-in voltage**. To give insight into this parameter, an electroabsorption setup was built with which polyfluorene based co-polymer hole-only devices were studied. These devices were already found to be well described using the EGDM, which makes it possible to interpret the voltage at which the electroabsorption signal goes to zero in relation to the built-in voltage. A significant difference between both voltages was found. This is explained by charge carrier diffusion in the co-polymer layer. This work is described in Chapter 3.

As mentioned, the polyfluorene-based co-polymer devices were found to be well described using the EGDM. Now the question arises how well the ECDM can describe the transport in these devices. This was investigated in Chapter 4, using the extraction method introduced in Chapter 2. It was found that a similarly good fit to the data could be obtained but with an unrealistically high hopping site density. We view the unrealistically high site density as evidence for the absence of correlated disorder in this material. Hence, **one may discriminate between both models by making a comparison with the experimental site density**.

Analyzing electron transport is often more difficult due to an increased experimental uncertainty (possibly caused by charge carrier relaxation effects) and due to the presence of additional parameters describing a density of trap states in such materials. In Chapter 5, we re-analyzed published electrical characteristics of electron-only devices based on the well-studied small-molecule material Alq₃ using the EGDM and the ECDM. A consistent set of parameters was used for all devices studied. In contrast to the earlier analysis of these characteristics using a conventional model, a strong indication for the presence of a **significant injection barrier** was found. A **good fit quality** was found using a **realistic site density** with the **ECDM**.

In studying charge transport, it has often been noticed that charging effects can significantly affect the measurement results, in particular for electron transport. For this reason, an extension of the model in which also time-dependent **relaxation effects** are described, is valuable. Chapter 6 describes to what extent the EGDM can explain measured dark injection (DI) transients. For the polymer based hole-only devices studied already in Chapter 3 and 4, a strong indication for the presence of the (time-dependent) relaxation effect was found from a thorough comparison between the experimental DI peak position with modeling results.

In Chapter 7 **parameter extraction is applied** to measured characteristics of two small-molecule based materials (Spiro-DPVBi and NET-5) which are employed in the white multilayer stack mentioned. Subsequently, these experimental results on the mobility have been employed in a **charge transport model based on 3D Monte Carlo simulations**, developed by the Eindhoven University of Technology. A **comparison between the predicted and the experimental** current-density versus voltage curve is presented. This shows that it is now possible to make a multilayer OLED model based on physically interpretable parameters and experimentally determined mobilities. With this model, further experimental validation is possible and scenario studies can be done that can bring the rational design of more efficient OLEDs one step closer.

Samenvatting

De ontwikkeling van een model voor ladingstransport in organische licht-emitterende diodes (OLEDs)

Organische licht-emitterende diodes (OLEDs) zijn **veelbelovende lichtbronnen** voor de toekomst aangezien ze dun, flexibel en in allerlei kleuren gemaakt kunnen worden. Het verbeteren van de efficiëntie is een belangrijke uitdaging. De beschikbaarheid van een model dat de transportfysica van deze organische diodes beschrijft, kan het mogelijk maken OLEDs op een systematische manier te ontwerpen zodat de efficiëntie kan worden verbeterd. De meest recente transport modellen geven inzicht in processen op de moleculaire schaal, omdat zij het ladingstransport beschrijven in termen van fysisch interpreteerbare parameters. Dit inzicht maakt het ontwikkelen van bruikbare materialen beter mogelijk. In dit proefschrift worden cruciale elementen op weg naar het ontwikkelen van een model voor **multilaags witte OLEDs** gepresenteerd.

De witte OLEDs waarop dit proefschrift zich uiteindelijk richt worden geïntroduceerd in Hoofdstuk 1. Ze bevatten opgedampte electron- en gatentransportlagen, en ook een blauw emitterende fluorescente laag en rood en groen lichtgevende fosforescente lagen. Allereerst wordt een overzicht gegeven van hoe men stroomdichtheid (J) tegen spanningen (V) karakteristieken van enkellaags OLEDs kan analyseren. Het onlangs ontwikkelde “**extended Gaussian disorder model**” (EGDM, “uitgebreide Gaussische wanorde model”) en het “**extended correlated disorder model**” (ECDM, “uitgebreide gecorreleerde wanorde model”) worden geïntroduceerd. In dit proefschrift worden deze modellen gebruikt om de elektrische karakteristieken van verscheidene enkellaags OLEDs op basis van kleine-molecuul materialen te bestuderen. Dit is gedaan om de noodzakelijke stappen naar multilaags modellering te onderzoeken en om de mobiliteit van de ladingsdragers in deze materialen te verkrijgen. Ook zijn enkellaags polymere OLEDs bestudeerd om aanvullende methodes te ontwikkelen voor het bestuderen van transport in deze organische materialen. De interpretatie van de elektrische karakteristieken blijkt gedetailleerde kennis van de materialen maar ook van de interfaces te vragen. Hierbij zijn verscheidene parameters betrokken die bepaald moeten worden voor een nauwkeurige beschrijving.

Ten eerste leidt dit tot de vraag hoe nauwkeurig de materiaalparameters die de **mobiliteit** in enkellaags devices bepalen, verkregen kunnen worden op basis van $J(V)$ karakteristieken. In Hoofdstuk 2 wordt een extractiemethode gebaseerd op het Gauss-Newton algoritme gepresenteerd. De methode is uitvoerig getest op zo-

wel gaten als elektronentransport karakteristieken om de **nauwkeurigheid** en de **bepalingen** van het extractiealgoritme te onderzoeken. We hebben geconstateerd dat voor gatentransport de extractie relatief eenvoudig is, in tegenstelling tot de situatie bij elektronen waar het gebruik van aanvullende gedetailleerde kennis van de bestudeerde systemen cruciaal blijkt.

Het ontwikkelen van **onafhankelijke experimentele technieken** die de mobiliteitsbepalende parameters vastleggen verhoogt de nauwkeurigheid van de mobiliteitsbepaling. Een belangrijke parameter in enkellaags systemen is de **inbouwspanning**. Om inzicht te krijgen in deze parameter is een electroabsorptie opstelling gebouwd waarmee gatentransport systemen zijn bestudeerd. Dit wordt beschreven in Hoofdstuk 3. De OLEDs zijn gemaakt van een copolymeer op basis van polyfluoreen. Uit eerdere studies, en uit onderzoek beschreven in Hoofdstuk 4, is gebleken dat het EGDM deze OLEDs goed kan beschrijven. Dit maakt het nu mogelijk de spanning waarbij het electroabsorptiesignaal door nul gaat te interpreteren in relatie tot de inbouwspanning. Er wordt een significant verschil gevonden tussen beide spanningen. Dit verschil kan worden verklaard door de diffusie van ladingstraggers in de organische laag.

Zoals genoemd kunnen de $J(V)$ karakteristieken van de bestudeerde blauwe OLEDs goed beschreven worden middels het EGDM. Nu komt de vraag naar voren of ook het ECDM deze karakteristieken kan beschrijven. Dit is bestudeerd in Hoofdstuk 4 gebruikmakend van de extractiemethode uit Hoofdstuk 2. We hebben gevonden dat een vergelijkbaar goede fit aan de data gemaakt kan worden met het ECDM, maar alleen met een onrealistisch hoge moleculaire dichtheid. Dit zien we als een bewijs voor het afwezig zijn van gecorreleerde wanorde. **Hiermee is het mogelijk een onderscheid tussen beide modellen te maken op basis van een vergelijking met de experimentele moleculaire dichtheid.**

Het analyseren van elektronentransport is vaak lastiger dan het analyseren van gatentransport door een verhoogde experimentele onzekerheid (mogelijk veroorzaakt door relaxatie-effecten van de ladingstraggers) en door de aanwezigheid van extra parameters die de dichtheid van “trap” toestanden in organische materialen beschrijven. In Hoofdstuk 5 worden gepubliceerde elektrische karakteristieken van het uitvoerig bestudeerde OLED materiaal Alq₃ geanalyseerd middels het EGDM en het ECDM. Een enkele set van parameters is gebruikt voor alle bestudeerde OLEDs. In tegenstelling tot de eerdere studie met een conventioneel transport model wordt een sterke indicatie voor een **significante injectiebarrière** gevonden. Het **ECDM** geeft de **beste fit** bij een **realistische moleculaire dichtheid**.

Bij het bestuderen van ladingstransport wordt met name bij elektronentransport vaak gevonden dat oplaadefecten het meetresultaat significant kunnen beïnvloeden. Daarom is een uitbreiding van het model, dat ook de tijdsafhankelijke processen kan beschrijven, waardevol. In Hoofdstuk 6 wordt onderzoek gepresenteerd naar de vraag in hoeverre het EGDM de gemeten tijdsafhankelijke reactie op een elektrische spanningsstap ook wel “dark injectie” (DI) genoemd, kan beschrijven. Voor de polymere OLEDs die ook in Hoofdstuk 3 en 4 zijn bestudeerd is een sterke indicatie voor de aanwezigheid van het tijdsafhankelijke **relaxatie-effect** gevonden. Dit blijkt uit een grondige vergelijking tussen de experimenteel verkregen DI piek positie met het modelresultaat.

In Hoofdstuk 7 is **parameterextractie toegepast** op gemeten $J(V)$ karakteristieken van twee kleine-molecuul materialen (Spiro-DPVBi en NET-5) die in de witte multilaag OLED worden gebruikt. Vervolgens zijn de experimenteel verkregen mobiliteiten gebruikt in een **ladingstransportmodel** dat is gebaseerd op **drie-dimensionale Monte Carlo simulaties**, ontwikkeld bij de Technische Universiteit Eindhoven. Middels dit model is een **vergelijking tussen een voorspelling en de gemeten $J(V)$ karakteristiek** mogelijk. Dit laat ook zien dat het nu mogelijk is om een multilaags OLED-model op basis van fysisch interpreteerbare parameters en experimenteel bepaalde mobiliteiten te maken. Met dit model is een verdere experimentele validatie mogelijk en kunnen scenariostudies worden uitgevoerd die het systematisch ontwerpen van efficiëntere OLEDs versnellen.

List of publications

Published and submitted papers

1. *Free energies of steps on (111) fcc surfaces*,
P. R. Kole, R. J. de Vries, B. Poelsema, and H. J. W. Zandvliet, *Solid State Communications* **136** (6), 356-359 (2005).
2. *Methodology for performing RF reliability experiments on a generic test structure*,
G. T. Sasse, R. J. de Vries, and J. Schmitz, *IEEE ICMTS*, 177 (2007).
3. *Spatial mapping of the inverse decay length using scanning tunnelling microscopy*,
R. J. de Vries, A. Saedi, D. Kockmann, A. van Houselt, B. Poelsema, and H. J. W. Zandvliet, *Applied Physics Letters* **92**, 174101 (2008).
4. *Analysis of hole transport in a polyfluorene based copolymer - evidence for the absence of correlated disorder*,
R. J. de Vries, S. L. M. van Mensfoort, V. Shabro, S. I. E. Vulto, R. A. J. Janssen, and R. Coehoorn, *Applied Physics Letters* **94**, 163307 (2009).
5. *Relation between the built-in voltage in organic light-emitting diodes and the zero-field voltage as measured by electroabsorption*,
R. J. de Vries, S. L. M. van Mensfoort, R. A. J. Janssen, and R. Coehoorn, *Physical Review B* **81**, 125203 (2010).
6. *Electron transport in the organic small molecule material BA1q - the role of correlated disorder and traps*,
S. L. M. van Mensfoort, R. J. de Vries, V. Shabro, R. A. J. Janssen, and R. Coehoorn, *Organic Electronics* **11**, 1408 (2010).

7. *Hole transport in the small molecule material α -NPD: evidence for the presence of correlated disorder*,
S. L. M. van Mensfoort, V. Shabro, R. J. de Vries, R. A. J. Janssen, and R. Coehoorn, *Journal of Applied Physics* **11**, 113710 (2010).
8. *Guest-concentration dependence of the mobility in a fluorene-arylamine host-guest system in the guest-to-guest regime*,
H. T. Nicolai, A. J. Hof, M. Lu, R. J. de Vries, P. W. M. Blom, and R. Coehoorn, *Applied Physics Letters* **99**, 203303 (2011).
9. *Effects of energetic disorder on the low-frequency differential capacitance of organic light emitting diodes*,
W. Chr. Germs, S. L. M. van Mensfoort, R. J. de Vries, and R. Coehoorn, *Journal of Applied Physics*, accepted.

Manuscript in preparation

1. *Extraction of the materials parameters that determine the mobility in disordered organic semiconductors from the current-voltage characteristics: accuracy and limitations*,
R. J. de Vries, A. Badinski, R. A. J. Janssen, and R. Coehoorn.

Curriculum vitae



Rein de Vries werd geboren op 30 januari 1984 in Hengelo in Overijssel. Hij groeide er op en in 2002 rondde hij zijn VWO opleiding af aan de Scholengemeenschap de Grundel. Vervolgens studeerde hij Technische Natuurkunde aan de Universiteit van Twente waar hij zijn Bachelor diploma cum laude behaalde. Rein combineerde zijn studie met een sportief leven en volgde een minor sportfysica. Tijdens de Master fase van zijn studie, eveneens aan de Universiteit van Twente, liep Rein stage bij Philips Research in Eindhoven in de groep Fotonische Materialen en Devices (FMD) onder begeleiding van prof. dr. Reinder Coehoorn en dr. Siebe van Mensfoort. Hier deed hij onderzoek naar de elektrische geleiding van organische lichtgevende diodes (OLEDs). Tijdens zijn afstudeeronderzoek in Twente in de groep van prof. dr. Bene Poelsema richtte Rein zich onder begeleiding van prof. dr. Harold Zandvliet op het meten van de elektronische structuur van moleculen op oppervlakken met behulp van “Scanning Tunneling Microscopy” (STM). De resultaten van dit onderzoek zijn gepubliceerd, en Rein ontving in 2008 zijn Master diploma cum laude. Na een leerzame ervaring als stagair bij Philips Research, begon Rein ook weer in de groep FMD aan een uitdagend promotieonderzoek naar ladingstransport in witte OLEDs. Hierbij was hij ook verbonden aan de groep Moleculaire Materialen en Nanosystemen van de Technische Universiteit in Eindhoven (TU/e), geleid door prof. dr. ir. René Janssen. De belangrijkste resultaten van dit onderzoek zijn beschreven in dit proefschrift. Rein heeft zijn werk kunnen presenteren op diverse nationale en internationale symposia en conferenties, onder meer in Detroit, Barcelona, Brussel, Kopenhagen, Ede en Veldhoven. Tijdens zijn promotieonderzoek heeft Rein drie studenten begeleid tijdens hun externe stage en afstudeeronderzoek.

Rein de Vries was born on the 30th of January 1984 in Hengelo in Overijssel. In 2002, he finished his high school at the “Scholengemeenschap de Grundel”. Subsequently, he studied Applied Physics at the University of Twente where he obtained his Bachelor degree cum laude. Rein combined his studies with a sportive life and followed the minor “sport physics”. During the Master phase of his studies, also at the University of Twente, Rein did an internship in the Photonic Materials and Devices (PMD) group at Philips Research Laboratories in Eindhoven under the daily supervision of prof. dr. Reinder Coehoorn and dr. Siebe van Mensfoort. He investigated the electrical transport in organic light-emitting diodes (OLEDs). During his graduation project in Twente in the group of prof. dr. Bene Poelsema and prof. dr. Harold Zandvliet, Rein focussed on the measurement of the electronic structure of molecules on surfaces using “Scanning Tunneling Microscopy” (STM). The results were published, and in 2008 Rein obtained his Masters degree cum laude. After a good experience as an intern at Philips Research, Rein started in the PMD group on a challenging PhD project on the charge transport in white OLEDs. He was also connected to the Molecular Materials and Nanosystems group at the Eindhoven University of Technology (TU/e), headed by prof. dr. ir. René Janssen. The most important results of this investigation are described in this thesis. Rein presented his work at national and international symposia and conferences, for example in Detroit, Barcelona, Brussel, Kopenhagen, Ede and Veldhoven. During his PhD study, Rein has guided three students during their external internship and graduation project.

Dankwoord

Dit proefschrift is het resultaat van vier jaar onderzoek in een divers samenwerkingsverband met vele collega's. Mijn promotietraject bij Philips Research was een bijzondere, leerzame en vormende ervaring waarvoor ik iedereen die er op welke manier dan ook aan heeft bijgedragen enorm wil bedanken.

Allereerst wil ik mijn promotor prof. Reinder Coehoorn bedanken voor zijn dagelijkse begeleiding bij Philips Research. Reinder, ik heb in allerlei opzichten veel van je geleerd. Ik bewonder je kennis, enorme drive voor wetenschap en in het bijzonder je inzet om je promovendi op allerlei vlakken naar een hoger niveau te brengen. Hier heb ik de vruchten van mogen plukken. Reinder, bedankt! Naast de begeleiding van Reinder was ook prof. René Janssen altijd betrokken bij het project. Als groepsleider van de vakgroep Moleculaire Materialen en Nanosystemen (M2N) nam ook jij de tijd om bijna iedere twee weken inhoudelijk te praten over mijn werk. Je wist knelpunten zo te benoemen dat ik er weer mee verder kon, dit heeft me vaak geholpen. Reinder en René, bedankt voor deze kans en voor alles wat jullie voor me hebben gedaan.

Graag wil ik het *Dutch Polymer Institute* (DPI) bedanken voor de financiering van het project. In het bijzonder wil ik John van Haare en prof. Frans de Schrijver bedanken voor het zorgvuldig volgen van het project en de waardevolle inbreng.

I also want to thank prof. Wolfgang Brütting and prof. Beat Ruhstaller for their willingness to be a part of my thesis defense committee and judging my thesis for scientific value. Moreover I want to thank you, together with prof. Paul Blom, prof. Neil Greenham, Robert Nitsche, Evelyne Huber, Matthias Schober, and Herman Nicolai for your cooperation within the European Project AEVIOM. Ook dr. Peter Bobbert en dr. Martijn Kemerink wil ik bedanken voor de bereidheid deel uit te maken van mijn commissie. Peter, de afgelopen jaren hebben we regelmatig samen gereisd en gewerkt binnen allerlei projecten. Samen met de promovendi; Jeroen Cottaar, Frank, Jeroen van der Holst, Murat en Jeroen de Groot leg je het theoretisch fundament voor het experimenteel bestuderen van transport processen in organische materialen. Zonder jullie was het werk dat ik heb mogen doen niet mogelijk geweest, bedankt voor alle bijdragen. Martijn, als lid van de groep van René ken je dit werk goed en gezien je expertise op het gebied van transport in organische materialen ben ik blij dat je deel uitmaakt van de commissie.

Binnen onze groep heb ik de afgelopen jaren samengewerkt met vele andere studenten. Maarten, Charley, Hanno, Wijnand, Vahid, Rossella en Alexander, bedankt voor jullie gezelschap en de waardevolle bijdragen. Vervolgens wil ik mijn kamergenoten; Ties, Mark-Jan, Harm, Silke en Paul bedanken voor jullie plezierige gezelschap. Jullie wisten me waar nodig altijd even af te leiden met de nodige humor.

Graag wil ik de collega's bij M2N bedanken voor de suggesties tijdens meetings van de groep en de prettige sfeer. Erwin, Kevin, Wijnand Dijkstra, Wijnand Germs, Sandra, Veronique, Dominique, Erik, Ron, Simon, Kees, Martijn, Nick, Jiri, Stephan, Dimitri, Klara, Christian, Augusta, Zuhail en Willem, bedankt! Ook wil ik de collega promovendi bij Philips Research, Edsger, Fatemeh, Simon, Mark-Jan en Anne-Marije bedanken voor het plezierige gezelschap. Dan zijn er vele collega's bij Philips Research waaronder, Hans, Herbert, Leendert, Piet, Pauline, Mark, Peter, Jan, Margreet, Dirk, Gert, Frans en prof. Dago de Leeuw bedankt voor jullie veelzijdige inbreng. *I would like to thank the colleagues from Philips Research Aachen for sample fabrication which was crucial for the project. Peter Loebel, Volker and Stefan thank you for the pleasant collaboration.* Ton van den Biggelaar wil ik bedanken voor het zorgvuldig vervaardigen van de samples in Eindhoven. Voor het design van de cover van dit proefschrift wil ik Bertina Senders hartelijk danken.

Harm, het is aan jou om een deel van mijn werkzaamheden over te nemen. Ik vind het dan ook gepast dat je paranimf bent bij de verdediging en blijf graag met je samenwerken om een vloeiende overgang mogelijk te maken. Bedankt voor je inbreng en de samenwerking. *Marco, we have been in the same environment for almost four years. Thank you for your support and the collaboration, we have seen and learned a lot.* Siebe, ook jou wil ik bedanken. Je niveau, positieve instelling en sociale persoonlijkheid hebben er sterk aan bijgedragen dat ik allereerst met plezier een stage heb gelopen bij Philips Research en er vervolgens ook een promotie die voortging op je werk heb gedaan. De afgelopen jaren ben je altijd betrokken gebleven bij mij en onze groep. Bedankt voor je inbreng en voor je bereidheid paranimf te zijn.

Voor de nodige ontspanning ben ik dank verschuldigd aan vele vrienden, familieleden en kennissen. Het voert te ver hier iedereen bij naam te noemen. Jeroen, Priscilla, Flip, Joost, Nard, Floor, Sibrecht, Bram, Rico, Eva, Jelle, Paul, Chris, Ton, Herjan, Theo, Smeets, Lisa, Kristel, Erwin, Michiel, Rianne, Anna-Catharina, Matthijs, Hetty, Peter, Andre, Marloes, Joep, Ron, Marjolein, Rik, Eva, Sandra, Bob, Jos en Olga bedankt voor de vele mooie momenten. Papa, mama, Gemma, Eelke en Marly, zonder jullie betrokkenheid en support was dit me niet gelukt. Bedankt dat jullie er altijd voor me zijn.

Rein